

Characterization and quality assurance of silicon micro-strip sensors using pulsed infrared laser for the CBM Experiment

Dissertation
zur Erlangung des Doktorgrades
der Naturwissenschaften

beim Fachbereich Physik
der Goethe-Universität
in Frankfurt am Main

Pradeep Ghosh
aus Bilaspur, Indien

Frankfurt am Main 2015
(D 30)

vom Fachbereich 13 der

Johann Wolfgang Goethe - Universität als Dissertation angenommen.

Dekan: Prof. Dr. Rene Reifarth

Gutachter : Prof. Dr. Peter Senger

Prof. Dr. Joachim Stroth

Datum der Disputation : 07. April. 2016

I would like to dedicate this thesis to my dear parents and loving
wife ...

Acknowledgements

Carrying out of this Ph.D. work would not be possible without the encouragement and support of my supervisor, Peter Senger. I would also like to thank Jürgen Eschke, Johann Heuser for many insightful discussions and their continuous support, Haik Simon for regular feedback as an external supervisor and the Helmholtz Graduate School for Heavy Ion Research (HGS-HIRe) for fruitful lectures and soft-skill courses. To all of them I express my deep gratitude for this excellent opportunity.

Working on a Ph.D. has been an exciting and unforgettable experience. This is owing to the friendliness and openness of the whole CBM team, which I appreciate sincerely. I would also be grateful to the help and efforts in the Ph.D. work by Wolfgang Niebur and Peter Zumbruch without whom the progress was not possible.

I also want to thank to the Helmholtz Research School for Quark Matter Studies (H-QM) for the numerous lecture weeks and other educational events they organized. I am deeply indebted to my friends, Piotr Szwangruber and Ioannis Bouras, whose company was so important for me at tough times, and with whom I spend the best and unforgettable moments of these three years.

Here I want to recollect my school teacher of physics S.K. Singh, University professors Rudra Pratap Malik (BHU), Raghuvir Pratap Singh (DU), Eric Royer (CEA-Saclay) and Walter Ambrosini (Uni. de Pisa) for making physics interesting for me and making sure to have a strong foundation for my career as physicist.

Finally, I want to thank to my wife, Yashika and my parents for their love and support.

Abstract

The Compressed Baryonic Matter (CBM) experiment will explore the phase diagram of strongly interacting matter in the region of high net baryonic densities. The matter at these extreme conditions will be produced and studied in heavy-ion collisions with a fixed target set-up.

The present work is dedicated to the main component of the CBM experiment - the Silicon Tracking System (STS). The STS comprises of 8 tracking stations with 1292 double sided silicon micro-strip sensors. The STS has to enable the reconstruction of up to 1000 charged particle tracks per nucleus-nucleus interaction at a rate of up to 10 MHz, provide a momentum resolution of $\Delta p/p = 1\%$, and withstand the radiation load of up to $10^{14} n_{eq}/cm^2$ (n_{eq} radiation dose of 1 MeV neutron equivalent). Self triggering read-out electronics will be located on the periphery of the detecting planes, and connected to the sensors with low mass micro-cables.

During the R&D phase, as well as in the pre-series and series production phase, the characterization of the sensors, of the front-end electronics and of the complete detector modules has to be performed. It is evident that characterization of more than 1000 silicon micro-strip sensors and later of complete detector modules is very time consuming, and may even damage the objects if not performed with great care. One of the goals of this work was to develop a systematic procedure for the quality assurance for the double-sided silicon micro-strip sensors. This includes static optical inspection and visual tests, passive electrical test (such as leakage current, bulk capacitance, inter-strip capacitance & resistances, bias resistance, and coupling capacitance), radiation hardness and long-term stability. A strategy for

the quality assurance of these sensors is presented, defining the various tests to be performed and the documentation of the results. The techniques and quality assurance criteria will be applied for the pre-series and series production.

With decreasing feature size and increase in functionality and structures, the classical mechanical probe approach for internal fault detection and functional testing faces increasing challenges. In the field of silicon based chips and sensors there is rarely any analysis on the topic of non-invasive or contact-less probing and characterization, despite the fact that the contact-less probing is becoming more and more important as the fabrication technologies become smaller and more susceptible to the parasitic impact of mechanical probes. The silicon micro-strip double sided sensors used in STS have a complex structure, such as 1024 metal electrodes, 2048 bias resistors, 2048 DC pads and 4098 AC pads for probing, several guard rings in the prototype sensor. Photo-intrusive technique is one of the best solution for the characterization and investigation of crucial parameters related to the detector operation and its functionality. A photo-intrusive probing is a method in which a non-invasive pulsed laser of desired wavelength is used to inject the photon into the bulk and resulting in electron-hole pairs (e-h). In a completely depleted silicon sensor the charge injected (or generated) by the pulsed laser beam could be detected as current and shall be used for characterization.

A non-invasive contact-less Laser Test System (LTS) was developed based on a pulsed laser to investigate properties of the silicon sensors. The set-up is able to inject charge locally and scan sensors(or detector modules) with a pulsed infra-red laser driven by a step motor. The LTS is designed to measure sensor response in an automatized procedure at several thousand positions across the sensor with focused infra-red laser light (spot size $\approx 12 \mu\text{m}$, wavelength = 1060 nm). The duration ($\approx 10 \text{ ns}$) and power ($\approx 5 \text{ mW}$) of the laser pulses are selected such that the absorption of the laser light in the $300 \mu\text{m}$ thick

silicon sensors produces a number of about 24000 electrons, which is similar to the charge created by minimum ionizing particles (MIP) in these sensors. The set-up was used to developed characterization procedures to determine the charge sharing between strips, and to measure qualitative uniformity of the sensor response over the whole active area. The prototype sensors which are tested with the set-up are small prototype sensors (256 strips, orthogonal strips, pitch = 50 μm on each side) and full size detector modules (1024 strips/side, stereo angle on p-side of 7.5 $^\circ$ and pitch = 58 μm). They are read-out using a self-triggering prototype read-out electronic ASIC called n-XYTER. Laser scans for amplitude response, charge sharing in the inter-strip region, and spot-size determination technique are reported. For the verification of the some design parameters, unique methods of determining coupling capacitance, and inter-strip capacitance have been developed. The modules were also tested with proton beams, and the charge sharing in the inter-strip region has been compared to the laser test results.

Kurzfassung

Die Experimente am Compressed Baryonic Matter (CBM) Detektorsystem der Facility for Antiproton and Ion Research (FAIR) haben zum Ziel, das Phasendiagramm der starken Wechselwirkung im Bereich hoher Netto-Baryondichte zu erforschen. Ideale Voraussetzungen für diese Experimente bieten Schwerionenkollisionen im FAIR-Energiebereich, da sie die Möglichkeit bieten, hochkomprimierte Kernmaterie im Labor herzustellen und zu untersuchen.

Die vorliegende Arbeit befasst sich mit dem zentralen Detektor des CBM-Experiments, das Silicon Tracking System (STS). Das STS befindet sich im Feldvolumen (ca. 1 m^3) eines Dipolmagneten und besteht aus acht Ebenen mit insgesamt 1292 doppelseitigen Silizium-Mikrostreifen-Sensoren. Mithilfe des STS können bis zu 1000 geladene Teilchenspuren pro Kern-Kern Wechselwirkung gemessen und rekonstruiert werden, mit einer Reaktionsrate von bis zu 10 MHz, einer Impulsauflösung von $\Delta p/p = 1\%$, und einer Rekonstruktionseffizienz von über 95%. Der STS ist für eine Strahlungs dosis von bis zu $1 \times 10^{14} \text{ n}_{\text{eq}}/\text{cm}^2$ ausgelegt ($\text{n}_{\text{eq}} = 1 \text{ MeV}$ Neutronen äquivalente Strahlendosis). Die Detektorsignale werden über Mikrokabel mit extrem geringer Massebelegung von der freilaufenden Front-End-Elektronik ausgelesen, die sich an der Peripherie der Detektorebenen außerhalb der aktiven Fläche befindet.

Die Charakterisierung der Sensoren, der Front-End-Elektronik und der kompletten Detektormodule ist ein wesentlicher Bestandteil der Entwicklungsphase und der Vorserien- und Serienproduktion. Aufgrund der großen Stückzahlen ist diese Aufgabe besonders aufwendig in der Vorserien- und Serienproduktion. Die Charakterisierung der mehr als 1000 Silizium-Mikrostreifen-Sensoren und anschließend der kompletten Detektormodule ist sehr zeitaufwendig und muss mit großer Sorgfalt durchgeführt werden, um die Objekte nicht zu beschädigen. Eines der Ziele dieser Arbeit war es, ein systematisches Verfahren für die Qualitätssicherung der doppelseitigen Silizium-Mikrostreifen-Sensoren zu entwickeln. Dazu gehören optische Inspektion und visuelle Tests, passive elektrische Tests (wie Leckstrom, Volumenkapazität, Zwischenstreifen-Kapazität und -Widerstand, Vorspannungswiderstand und Kopplungskapazität), Strahlungsbeständigkeit und Langzeitstabilität. Eine Strategie zur Qualitätssicherung der Sensoren sowie die Definition der verschiedenen Tests und die Dokumentation der Ergebnisse werden vorgestellt.

Abnehmende Strukturgröße und zunehmende Funktionalität der Sensoren stellen klassische mechanische Prüfverfahren zur Fehlererkennung und Funktionsprüfung vor wachsende Herausforderungen. Auf dem Gebiet der Silizium-basierten Chips und Sensoren gibt es wenige Analysen zum Thema nicht-invasive oder berührungslose Untersuchungen und Charakterisierung, obwohl die kontaktlose Untersuchung mehr und mehr an Bedeutung gewinnt, da die Herstellungstechnologien kleiner und anfälliger für die parasitäre Auswirkungen mechanischer Sonden werden. Die doppelseitigen Silizium-Mikro-Streifen Sensoren des STS besitzen eine komplexe Struktur, wie zum Beispiel 1024 Metallelektroden, 2048 Vorspannungswiderstände, 2048 DC-Pads und 4098 AC-Pads für die Sondierung, und mehrere Schutzringe. Die foto-intrusive Technik ist die geeignetste Methode zur Charakterisierung und

Untersuchung der für Betrieb und Funktion wichtigen Detektorparameter. Eine foto-intrusive Untersuchung ist ein Verfahren, bei dem mit einem nicht-invasiven gepulsten Laser einer bestimmten Wellenlänge ein Photon in das Detektorvolumen injiziert wird um Elektronen-Loch-Paare (eh) zu erzeugen, die dann als Strom gemessen und zur Charakterisierung verwendet werden können.

Im Rahmen dieser Arbeit wurde ein nicht-invasives berührungsloses Laser-Testsystem (LTS) auf der Basis eines gepulsten Lasers entwickelt, um eine größere Anzahl von Silizium Sensoren effizient untersuchen zu können. Die Messapparatur ist in der Lage, die Ladung zu lokal zu injizieren, und die Sensoren (oder Detektormodule) mit einem gepulsten Infrarotlaser, der durch einen Schrittmotor verfahren wird, abzutasten. Das Testsystem ist dafür ausgelegt, das durch fokussiertes Infrarot-Laserlicht (Strahlfokussdurchmesser = 12 μm , Wellenlänge = 1060 nm) generierte Sensorsignal in einem automatisierten Verfahren an mehreren tausend Positionen auf der Sensoroberfläche zu messen. Die Dauer (10 ns) und Leistung (5 mW) der Laserimpulse sind so gewählt, daß durch die Absorption des Laserlichts in den 300 μm dicken Silizium-Sensoren etwa 24000 Elektronen erzeugt werden. Diese Anzahl entspricht der Ladungsmenge, die durch minimal-ionisierende Teilchen (MIP) in diesen Sensoren generiert wird. Mithilfe des Testsystems wurden Charakterisierungsverfahren entwickelt, um die Ladungsteilung zwischen den Streifen zu bestimmen und die Uniformität der Sensorsignale über die gesamte aktive Detektorfläche zu messen. Untersucht wurden kleine doppelseitige Prototyp-Sensoren (256 Streifen pro Seite, Stereowinkel 90°, Streifenabstand 50 μm) und große doppelseitige Sensoren, wie sie später im Experiment verwendet werden (1024 Streifen pro Seite, Stereowinkel 7.5°, Streifenabstand 58 μm). Die Sensorsignale wurden mithilfe eines selbstgetriggerten Prototyp-ASIC ausgelesen („n-XYTER“. Zur Verifizierung der Design-Parameter der Sensoren wurden neuartige Methoden zur Bestimmung des Verhältnisses von Kopplungskapazität zur Kapazität zwischen den Streifen entwickelt. Die Messergebnisse bezüglich Signalamplituden und Ladungsteilung zwischen den Streifen werden in der vorliegenden Arbeit vorgestellt und diskutiert. Die Ergebnisse der Lasertests zur Ladungsteilung im Bereich zwischen den Sensorstreifen wurden durch Messungen mit Protonenstrahlen an COSY/FZ Jülich überprüft.

Contents

Contents	vi
List of Figures	viii
List of Tables	xv
1 Introduction	1
2 The CBM experiment at FAIR	7
2.1 Facility for Anti-proton and Ion Research	7
2.2 CBM Physics	9
2.3 Physics case and observables	11
2.4 CBM detectors	13
3 Silicon Tracking System	22
3.1 Technical challenges for STS	25
3.2 Hit reconstruction in STS	26
3.3 Track reconstruction	27
3.4 Particle identification	28
3.5 Prototype sensors	31
4 Characterization & QA of silicon sensors	37
4.1 Visual inspection	39
4.2 Leakage current	39
4.3 Depletion voltage	40
4.4 Pinhole tests	41

4.5	Coupling capacitance	42
4.6	Inter-strip resistance	44
4.7	Inter-strip capacitance	45
4.8	Strip current	46
4.9	Long term stability	46
4.10	Radiation tolerance	47
4.11	Summary of electrical characterization and QA	49
5	Detector Characterization & QA using infra-red laser	51
5.1	Different methods of characterization	51
5.2	Interaction of light with silicon	56
5.3	Laser-induced charge generation	61
5.4	Choice of wavelength for characterization	64
5.5	Laser Test System of the STS	66
5.5.1	Infra-red laser	67
5.5.2	Detector modules	69
5.5.3	Front-end electronics and power supplies	71
5.5.4	Step motor and EPICS control	75
5.5.5	Data acquisition and analysis	76
5.6	Calibration of laser test stand	76
5.7	Characterization results	78
5.7.1	Sensor integrity and response	79
5.7.2	Charge sharing and η function	80
5.7.3	Spot-size measurement	82
5.8	Summary of Characterization and QA with LTS	86
6	In-beam measurements with protons	88
6.1	Experimental set-up	89
6.2	Analysis of the beam-data	90
7	Conclusions and outlook	100
	References	102

List of Figures

1.1	QCD Phase diagram with freeze-out points from a statistical analysis of experimental data, from [1], Plot from Ref. [2].	2
1.2	Freeze-out curve from a statistical model analysis in the temperature versus net-baryon density plane. Red and blue points show the region available by experiments at RHIC and FAIR, respectively, depending on the collision energy.	3
1.3	A schematic phase diagram of strongly interacting matter in temperature and net-baryon density plane	5
2.1	Schematic representation of proposed experimental facilities including SIS-100/300 at Facility for Anti-proton and Ion Research (right) along with present GSI experimental facility utilizing SIS-18 (left).	8
2.2	Baryon density as a function of elapsed time for the central Au+Au collisions at different energies as calculated using covariant hadronic transport approach HSD	9
2.3	Particle multiplicities times branching ratio for central Au+Au collisions at 25 AGeV as calculated with the HSD code calculated with the HSD transport code and the statistical model. For the vector mesons (ρ , ω , ϕ , J/ψ , ψ') the decay into lepton pairs was assumed, for D mesons the hadronic decay into kaons and pions.	10
2.4	Schematic representation of the HADES detector and the CBM experimental set-up along with its components.	14

LIST OF FIGURES

2.5	A schematic engineering view of the CBM magnet. The magnet is designed to hold the 3 layers of MVD and the 8 STS detector stations.	16
2.6	A prototype Micro-Vertex Detector boarded on a printed circuit board for test.	17
2.7	A photograph of prototype Micro-Vertex Detectors under test in the laboratory.	17
2.8	Engineering view of a cross section view of STS detector stations lined up for the CBM experiment. The STS is enclosed inside a magnet.	18
2.9	Engineering view of one of the stations composed of ladders piled up with silicon sensors (centre) and cooling plates (blue).	18
2.10	Engineering view of the RICH Detector (blue) with supported structures (grey) for the CBM experiment	18
2.11	Photograph of constructed 3 layers of RICH Detector walls under test during CERN beam-time	18
2.12	Engineering view of the Muon Chamber Detector Sector for SIS-100	19
2.13	Photograph of constructed MUCH prototype module under test in VECC Kolkata	19
2.14	Engineering view of the Transition Radiation Detector (TRD) for SIS-100	20
2.15	Photograph of constructed TRD prototype module under test in CERN	20
2.16	Engineering view of the Time-of-Flight (TOF) detector	21
2.17	Photograph of constructed TOF wall under test	21
2.18	Engineering view of the ECAL detector	21
2.19	Photograph of construction of super module of PSD for the beam best at CERN	21
3.1	Conceptual design of the tracking station with building blocks such as ladder structure and modules.	23
3.2	CAD design of the Silicon Tracking System with building blocks such as ladder structure and modules.	24

LIST OF FIGURES

3.3 (a) An Engineering model of STS (Green), MVD (Orange) and the H-Shaped superconducting magnet section (Brown) and (b) Tracks from a central 25 AGeV Au+Au collision overlaid with the GEANT simulation of the STS tracking stations.	25
3.4 Cluster size distribution in the micro-strip sensors of STS station 4 for a threshold of 4000 electrons applied in the read-out electronics.	26
3.5 Distribution of cluster sizes for the entire STS.	27
3.6 Display of reconstructed tracks from a central Au+Au collision at 25 AGeV projectile energy, shown in three different projections. . .	28
3.7 Track reconstruction efficiency in the STS as a function of the momentum for all tracks in central Au+Au at 25 AGeV projectile energy.	29
3.8 Momentum resolution in the STS as a function of the momentum for all tracks in central Au+Au at 25 AGeV projectile energy. . .	29
3.9 Invariant mass spectra for the hyperon decays: $\Lambda \rightarrow p\pi^-$ (left) $\bar{\Lambda} \rightarrow \bar{p}\pi^+$, $\Xi^- \rightarrow \Lambda\pi^-$ and $\Omega^- \rightarrow \Lambda K^-$ (right) central Au+Au collisions at 25 AGeV. p, π^-, K^- were identified by the TOF detector at $z = 10$ m with a time resolution of 80 ps. The simulated statistics results to 1×10^6 events at 25 AGeV.	30
3.10 Invariant-mass spectra for the decays $D^0 \rightarrow K^-\pi^+$, $D^+ \rightarrow K^-\pi^+\pi^+$ and their charge conjugates for 10^{10} and 10^9 central Au+Au collisions at 25 AGeV.	31
3.11 Schematic drawing of the 7.5 degree orientation of strips in prototype sensor	32
3.12 Photograph of a CBM05 prototype double sided silicon micro-strip sensor	32
3.13 A prototype sensor tab-bonded to the read-out cable boarded on a printed circuit board.	33
3.14 Schematic design of the prototype low-mass ultra thin read-out cables along with its parameters.	33
3.15 A photograph depicting the tab-bonded read-out cables on the sensors strips.	34

LIST OF FIGURES

3.16	A photograph showing a test STS-XYTER prototype front-end electronics chip attached to 4 read-out cables.	35
4.1	Steps in Quality Assurance tests for silicon micro-strip sensors. . .	38
4.2	Broken strips or non-uniformity	39
4.3	Scratch on sensor surface	39
4.4	Shorts on the strips	39
4.5	Leakage current measurement for CBM05 prototype sensor	40
4.6	Depletion voltage measurement for CBM05 prototype sensor . . .	41
4.7	Schematic representation of pinhole in the implant	42
4.8	Circuit diagram for the pinhole test	42
4.9	Coupling capacitance measurement: positioning of needles in the set-up	43
4.10	Coupling capacitance measurement at different strips for CBM02 prototype sensor	43
4.11	Inter-strip resistance measurement	44
4.12	Inter-strip capacitance measurement	45
4.13	Average strip current on CBM-STs sensor prototypes of different families	46
4.14	Long term stability measurement for sensors	47
4.15	Leakage current measurement for radiation hardness	48
4.16	Effect of irradiation on leakage and strip current	48
4.17	Effect of irradiation on operating voltage	48
5.1	A schematic representation of three characterization methods adopted to investigate operational parameters for the silicon sensor, namely: (a) Particle beam (proton, electron, X-rays etc.), (b) Radioactive source (α or β) and (c) Laser (red or infra-red).	52
5.2	The spectrum of electromagnetic radiation, including wavelength ranges for the various colors in the visible spectrum	57
5.3	Various process during interaction of light (photons) with semiconductor materials	57

LIST OF FIGURES

5.4	Schematic representation of the photon interaction with the semiconductor material based on the energy of the photon. The three situation are: (a) $E_{ph} < E_{gap}$, (b) $E_{ph} = E_{gap}$ and (c) $E_{ph} > E_{gap}$.	58
5.5	A schematic diagram representing a basic micro-strip silicon sensor structure. The sensor is of p-on-n type.	62
5.6	The absorption coefficient, in a variety of semiconductor materials at 300 K as a function of the vacuum wavelength of light. Silicon shown in red.	65
5.7	Schematics representation of the laser induced charge injection in the silicon micro-strip sensor.	68
5.8	A schematic view to the connection of various components in the laser test set-up. It comprises of 5 block (a) Control, (b) Laser, (c) Detector module (sensor, cable and front-end electronics), (d) EPICS control sequencer and communicating all control devices (e) DAQ - Data Acquisition from read-out-control.	68
5.9	Schematic of the detector module and latest prototype placed adjacent	72
5.10	Prototype detector modules prepared with different length of ultra-thin low mass read-out cables. All detector modules are equipped with CBM05 prototype sensors which is double sided sensor of size 6.2 cm \times 6.2 cm. (a) Detector module (M4) with 2 daisy-chained sensors read-out with 30 cm cable on the long strips (centre) (b) Detector module (M3) with 2 daisy-chained sensors read-out with 30 cm cable on the short strips (corner) (c) Detector module (M1) with 1 sensor read-out with 20 cm cable on long strips (centre).	72
5.11	A closer look to the detector module. (a) (on the left): sensor surface - edges, strips connected to aluminium traces on read-out cables via tab-bonding and (b) (on the right): the connection to FEE board via the ERNI connectors.	73

LIST OF FIGURES

5.12	Illustration of the read-out area and the channel numbers for the connection to the read-out cable for the three prototype modules 2013. The sensor areas with two-coordinate readout that can be explored in test experiments are indicated in yellow colour. (a) Module - M1 (b) Module - M2 (c) Module - M4 (Module - M3 is not shown in the schematic.)	73
5.13	A snapshot of the operator interface (OPI) based on Control System Studio tools for the EPICS sequencer in the laser test set-up.	75
5.14	Calibration: Optimum distance for focuser and optimum laser current	77
5.15	3D lego plot showing the hit counts on focused position after calibration	77
5.16	Photograph of the laser test set-up inside the enclosed light-tight box.	79
5.17	Fractional amplitude of charge amplitude collected at p-side . . .	80
5.18	Fractional amplitude of charge amplitude collected at n-side . . .	81
5.19	η function for p-side strips of CBM05 prototype sensor	81
5.20	η function for n-side strips of CBM05 prototype sensor	82
5.21	Analytical method to determine the spot-size of the laser using width of local minima	85
5.22	Total charge amplitude collected by all strip as function of laser position	85
5.23	Schematic representation of the quality assurance and characterization possible with the Laser Test System at the STS.	86
6.1	Schematic of the Beam time set-up at COSY-Jülich Research Centre	89
6.2	Snapshot of the Beam time set up with STS station with reference sensors and modules under test	90
6.3	Non-Irradiated sensor: Total cluster amplitude spectra from the P-side of station STS 03.	91
6.4	Non-Irradiated sensor: Total cluster amplitude spectra from the N-side of station STS 03.	91
6.5	Irradiated Cluster Charge Pside	92

LIST OF FIGURES

6.6	Irradiated Cluster Charge Nside	92
6.7	Correlation of the total cluster amplitude on the p- and n-sides in stations STS 00).	93
6.8	Correlation of the total cluster amplitude on the p- and n-sides in stations STS 01	93
6.9	Radiation Tolerance Pside	94
6.10	Radiation Tolerance Nside	94
6.11	<i>Left:</i> η measured for p-side of CBM05 with Gaussian fitting the peaks. <i>Right:</i> $f(\eta)$. Perpendicular tracks.	95
6.12	Cluster size distribution for slightly inclined tracks (10^0). Experimental data for n-side (the gray filled histogram), simulations with no (the solid line) and 20% (dashed) additional charge loosing. . .	96
6.13	Most probable registered charge in dependence of track angles. The points show the experimental data from beam-time 2013 (the open triangles – p-side, the filled squares – n-side, the uncertainties in the angle measurements are drawn with bars) and the modelled data are represented by the lines (the solid line – no charge losses in the sensor, the dashed – 20% losses).	97

List of Tables

1.1	Energy ranges (GeV) of operation and reaction rates of current (Hz) of current (STAR, PHENIX, NA61) and future experiments (MPD and CBM) on dense baryonic matter.	6
1.2	Observables (to be) measured in current and future experiments on dense baryonic matter.	6
5.1	A list of parameters or characteristics of the silicon sensors which is required to be investigated and their possibility with different methods available.	55
5.2	Specifications of the customised infra-red laser used in the set-up.	69
5.3	List of specifications for the beam delivery system (optical fibre) and the beam focuser (lens system) in the laser test set-up.	70
5.4	Description of the specification of the low voltage and high voltage power supply units in the laser test set-up	74
6.1	Specification for the reference detectors in the beam-time set-up i.e., Hodoscopes (1 and 2) and the silicon prototype detectors stations (0 and 1)	98
6.2	Specification for the latest prototype detectors in the beam-time set-up i.e., STS 02 and STS 03	99

Chapter 1

Introduction

The quest for understanding how the universe evolved has always fascinated researchers. Nowadays modern physics can quantitatively describe phenomena ranging from the scale of leptons and quarks (10^{-18} cm) to the scale of planetary objects (10^{28} cm) based on four fundamental forces of nature: gravity, electromagnetism, strong and weak interactions. Whereas gravity is described by Einstein's general relativity theory, the other three forces can be described to an excellent degree by the quantum field theory of quarks and leptons based on a framework consistent with the Einstein's special theory of relativity and quantum mechanics: so called standard model (SM).

The quantum chromodynamics (QCD) theory is an important part of the standard model of particle physics. It is the theory describing the interactions between quark(s) and gluon(s) which make up hadrons such as proton, neutron and pion. QCD has peculiar properties: confinement and asymptotic freedom. A promising way to study these properties is to investigate strongly interacting matter under extreme conditions where quarks are expected to be deconfined. This is one of the main motivation to study the QCD phase diagram. The experimental investigation of the QCD phase diagram with heavy ion collisions is an ongoing intense research topic at several international accelerator facilities for the past three decades.

The research on hot and dense matter started in 1980s with heavy-ion experi-

ments at Bevalac ¹ at LBL in Berkeley, then was continued at the AGS ² at BNL in Brookhaven and at the SIS18 at GSI in Darmstadt, moved to higher energies at the SPS at CERN, then to the RHIC ³ at BNL and finally to the LHC at CERN ⁴.

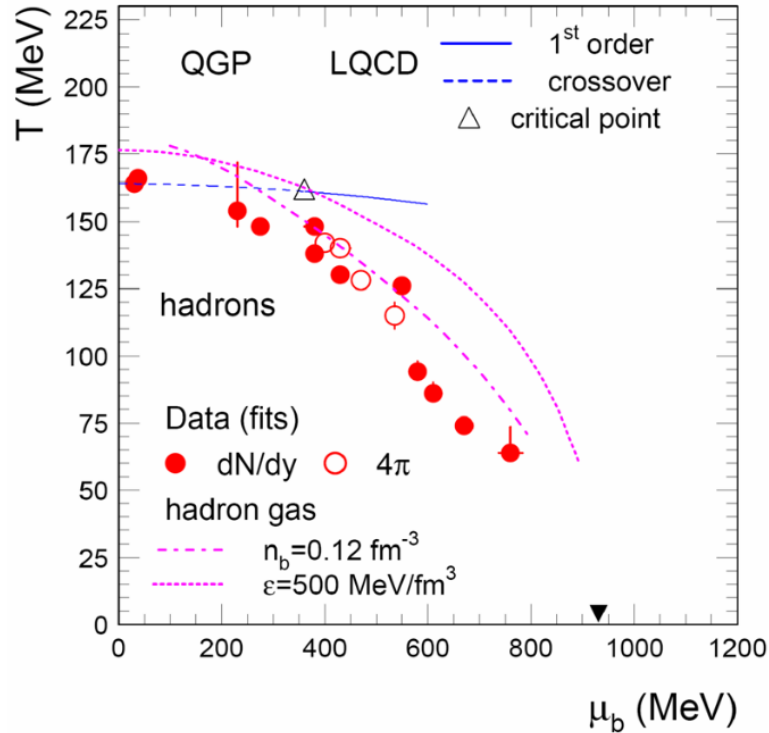


Figure 1.1: QCD Phase diagram with freeze-out points from a statistical analysis of experimental data, from [1], Plot from Ref. [2].

As a result of these experiments, the so called "chemical freeze-out curve" could be established as shown in fig. 1.1. The freeze-out point characterizes the situation where the produced particles cease to interact inelastically. At this

¹The Bevatron joined to the SuperHILAC at Lawrence Berkeley National Laboratory, U.S.A. was called Bevalac. It could accelerate a wide range of stable nuclei to relativistic energies.

²The Alternating Gradient Synchrotron (AGS) is a particle accelerator located at the Brookhaven National Laboratory in Long Island, New York, USA.

³The Relativistic Heavy Ion Collider (RHIC) is one of only two operating heavy-ion colliders, and the only spin-polarized proton collider ever built. Located at Brookhaven National Laboratory (BNL) in Upton, US

⁴The Large Hadron Collider (LHC) is the worlds largest and most powerful particle accelerator. It is the latest edition to CERN accelerator complex, Geneva Switzerland.

stage, the particle density is already lower than the saturation density. This is illustrated in fig. 1.2 which depicts the freeze-out curve as function of temperature and net-baryonic density [3]. The figure illustrates that the highest net-baryon density at freeze-out is produced at beam energies of 30 GeV, suggesting that also the highest net-baryon densities in the fireball is reached at this energy.

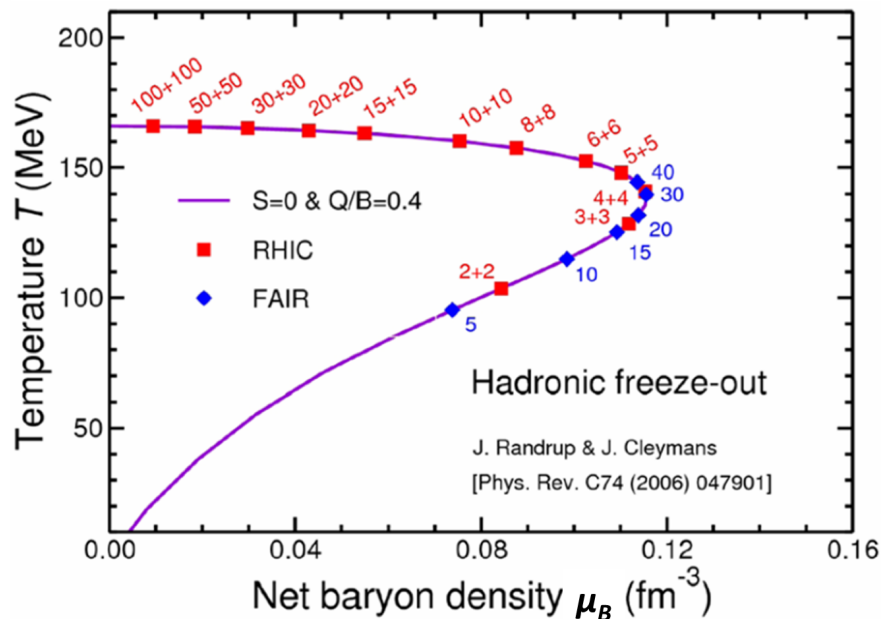


Figure 1.2: Freeze-out curve from a statistical model analysis in the temperature versus net-baryon density plane. Red and blue points show the region available by experiments at RHIC and FAIR, respectively, depending on the collision energy.

High-energy heavy-ion collisions offer the possibility to produce and investigate the highly compressed nuclear matter in the laboratory. In RHIC and LHC experiments, the measurements are focused on the study of de-confined QCD matter at very high temperatures and close to zero baryonic densities. The results from lattice QCD calculations predict that the transition from the de-confined to confined matter at almost zero baryonic densities is a smooth cross over [4], [5], [6], [7]. This is expected to change to a first-order transition at higher net-baryonic densities, i.e. when the nuclear matter is in highly compressed state. The experimental discovery of the first-order phase transition would represent a major progress in our understanding of the strongly interacting matter.

Depending on the center-of-mass energy in the collision, different values of temperatures and baryonic-chemical potentials are studied. At zero baryon-chemical potential the freeze-out temperature is found to be 155 - 165 MeV [8], which is accordance with the critical temperature (T_c) from lattice calculations, see Ref. [6], [9], [10] and [5]. The results from heavy-ion collisions at RHIC suggest the formation of a de-confined system of quarks and gluons [11] and [12]. Early lattice QCD calculations [13] suggested the existence of a crossover between partonic and hadronic matter at low baryon-chemical potential and a critical endpoint from which on the phase transition would be of the first order¹. The existence and value of the critical point (T_c) is largely debated in the Hadron physics community due to the fact that the lattice QCD calculations have a large systematic uncertainties at finite baryon-chemical potential ($\mu_B > 0$) [13] and [14].

The Beam Energy Scan (BES) experiment at RHIC investigated the partonic matter in wide range of temperatures, and low net-baryon densities. A much more detailed investigation of the QCD phase diagram of nuclear matter in the region of very high baryonic densities and moderate temperatures will be performed by the CBM experiment which will study the heavy-ion collision at beam energy range 2-35 AGeV [15]. Fig. 1.3 shows the QCD phase diagram [16] with our current understanding for the strongly interacting nuclear matter from Ref. [1] in which a newly postulated phase at high baryon density is suggested to exist [17].

There is a lack of understanding about the matter created at lower collision energies, i.e., high baryonic densities. The latter region of the QCD phase diagram which is poorly known theoretically and experimentally, it is one such object of vast physics program at lower beam energies, which is being carried out SPS/CERN and by the BES at RHIC/BNL and this will be continued at CBM/FAIR. One of the conclusions from the present knowledge about the QCD phase diagram obtained from the experimental measurements could be summarized as follows: The freeze-out conditions for the produced hadrons in a nucleus-nucleus collisions agree to the freeze-out curve as shown in fig. 1.1. Also, the same data presented in different way in fig. 1.2 indicates that freeze-out densities are expected at FAIR energies.

¹The discussion about the critical endpoint is very much under debate, see e.g. Ref. [14]

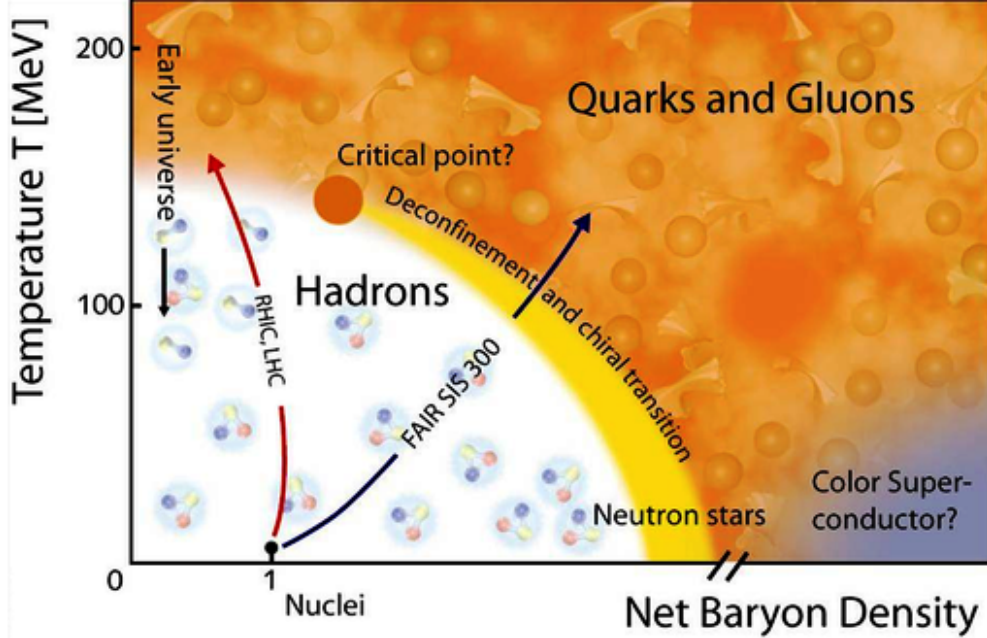


Figure 1.3: A schematic phase diagram of strongly interacting matter in temperature and net-baryon density plane

The different experiments (both present and future) dedicated to the investigation of the QCD phase diagram at high net-baryonic densities are listed in Table 1.1, together with the energy range and reaction rates. The Table 1.2 summarizes the observables for the beam energies ($\sqrt{s_{NN}} = 8 \text{ GeV}$) in the high baryon density region ¹. The CBM experiment will be the first experiment designed explicitly to have an access to these rare observables like di-leptons, multi-strange (anti-)hyperons, and D-mesons at high net baryon densities (μ_B).

The terra incognita of the QCD phase diagram motivates the experimental research program at the CBM experiment at FAIR. The CBM experiment will allow to study these topics with rare probes being sensitive to the medium, i.e. with the measurement of charm production and di-leptons. The experimental evidence of the first-order phase transition, the QCD critical point and in-medium modifications of hadron masses in dense baryonic matter would be a breakthrough for understanding the properties of the strong interaction. The potential physics

¹However, with the planned upgrade activities of accelerator for the beam energy scan at RHIC (BES II), there is certainly a possibility to have an access to the di-leptons

Table 1.1: Energy ranges (GeV) of operation and reaction rates of current (Hz) of current (STAR, PHENIX, NA61) and future experiments (MPD and CBM) on dense baryonic matter.

Experiments	Energy range (Au/Pb beams)	Reaction rates (Hz)
PHENIX & STAR @RHIC, BNL	$\sqrt{s_{NN}} = 7 - 200 \text{ GeV}$	1 – 800 (limitation by luminosity)
NA61 @SPS, CERN	$\sqrt{s_{NN}} = 6.4 - 17.4 \text{ GeV}$ $E_{kin} = 20 - 160 \text{ A GeV}$	80 (limitation by detector)
MPD @NICA, Dubna	$\sqrt{s_{NN}} = 4 - 11 \text{ GeV}$	1000 (design lumin. of $10^{27} \text{ cm}^{-2}\text{s}^{-1}$ for HI)
CBM & HADES @FAIR, Darmstadt	$\sqrt{s_{NN}} = 2.7 - 8.3 \text{ GeV}$ $E_{kin} = 2 - 35 \text{ A GeV}$	$10^5 - 10^7$ (limitation by detector)

Table 1.2: Observables (to be) measured in current and future experiments on dense baryonic matter.

Experiments	Observables for beam energies at about $\sqrt{s_{NN}} = 8 \text{ GeV}$			
	hadrons	correlation, fluctuations	di-leptons	charm
PHENIX & STAR @RHIC, BNL	yes	yes	no	no
NA61 @SPS, CERN	yes	yes	no	no
MPD @NICA, Dubna	yes	yes	no	no
CBM & HADES, FAIR, Darmstadt	yes	yes	yes	yes

observables and diagnostic probes that could be investigated and discovered in the section 2.3. An updated summary of the CBM Physics program could be found in Ref. [2] and [18]¹.

¹The current status of theoretical studies on the quantum chromodynamics (QCD) phase diagram at finite temperature and baryon chemical potential is reviewed by Kenji Fukushima and Tetsuo Hatsuda [16]

Chapter 2

The CBM experiment at FAIR

2.1 Facility for Anti-proton and Ion Research

The planned international Facility for Anti-proton and Ion Research (FAIR) in Darmstadt will provide unique research opportunities in the fields of nuclear, hadron, atomic and plasma physics [19]. The FAIR facility is a joint effort by 10¹ countries. Fig. 2.1 elaborates a schematic representation of all proposed experimental facilities including the synchrotron SIS 100/300 (two ring structure in red) and beam lines to experimental facilities (red lines). In the left part of the same graphic, the present GSI experimental facility and the SIS 18 synchrotron is shown along with UNILAC (in blue). The FAIR complex will host four scientific collaborations comprising 3000 researchers from about 53 countries. The four pillars of the scientific programs at FAIR are:

1. APPA: Atomic, Plasma Physics and Applications [20],
2. CBM: Compressed Baryonic Matter experiment [21],
3. NUSTAR: NUClear STructure, Astrophysics and Reactions [22] and
4. PANDA: anti-Proton ANnihilation at DArmstadt [23].

¹In alphabetical order: Finland, France, Germany, India, Poland, Romania, Russia, Slovenia, Sweden, and the United Kingdom. There are other countries like Austria, China, Italy, Spain and others which has not signed the convention but are collaborating with specific experiment(s) or research group(s) working for FAIR.

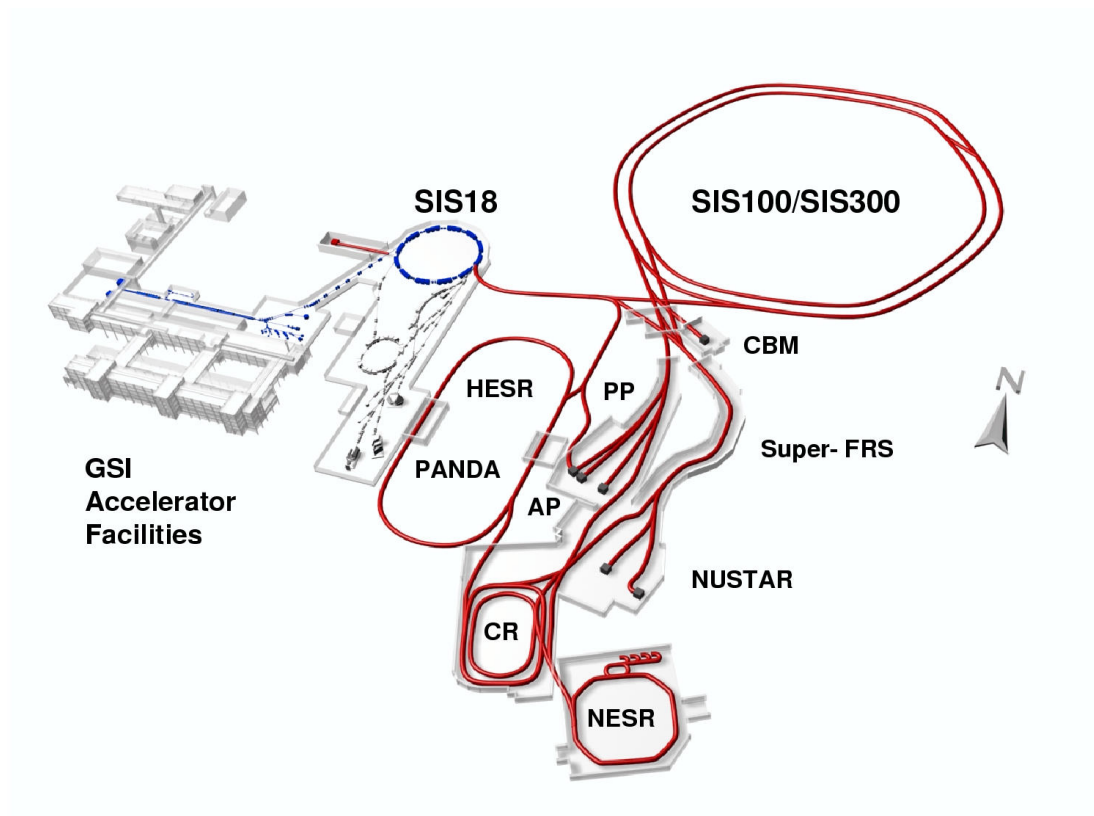


Figure 2.1: Schematic representation of proposed experimental facilities including SIS-100/300 at Facility for Anti-proton and Ion Research (right) along with present GSI experimental facility utilizing SIS-18 (left).

The SIS-100 synchrotron will deliver beams of protons up to 29 GeV, Gold (Au) up to 11 AGeV and nuclei with $Z/A = 0.5$ up to 14 AGeV. The beam intensities for CBM will be continued with beams from the SIS-300 synchrotron having protons up to 90 GeV, Au up to 35 AGeV and nuclei with $Z/A = 0.5$ up to 45 AGeV. The designed layout of the FAIR facility is shown in Fig. 2.1. A comprehensive and recent information related to the status of FAIR project could be found in Ref. [19].

2.2 CBM Physics

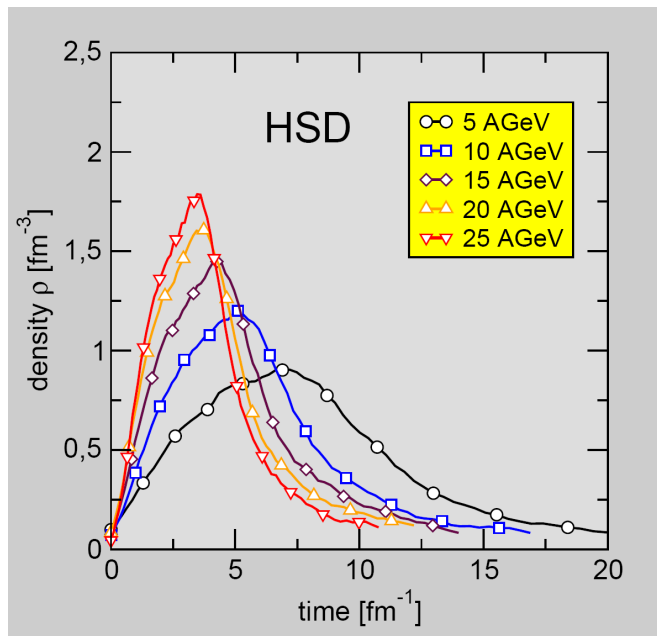


Figure 2.2: Baryon density as a function of elapsed time for the central Au+Au collisions at different energies as calculated using covariant hadronic transport approach HSD

The Compressed Baryonic Matter Experiment (CBM) [24] is one of the four major experimental pillars at FAIR. The CBM experiment is designed to perform precision measurements of hadronic, leptonic and photonic probes in order to explore the QCD phase diagram in the region of high net-baryon densities. The

SIS-100/300 beam energies are well suited to create high net-baryon densities in the heavy-ion collisions. The calculations from Ref. [25] suggest that, (e.g., see fig. 2.2) at 10 AGeV the densities up to about 7 times the saturation density could be created. At these densities the nucleons should overlap and a transition to a mixed phase of baryons and quarks could be expected.

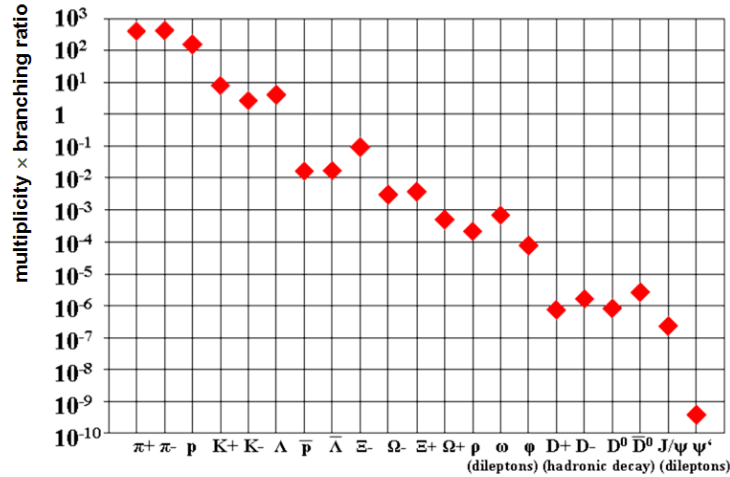


Figure 2.3: Particle multiplicities times branching ratio for central Au+Au collisions at 25 AGeV as calculated with the HSD code calculated with the HSD transport code and the statistical model. For the vector mesons (ρ , ω , ϕ , J/ψ , ψ') the decay into lepton pairs was assumed, for D mesons the hadronic decay into kaons and pions.

The experimental challenge for the CBM experiment is to measure multi-differential observables and particles with very low production cross-section and unprecedented precision. These include multi-strange (anti-) hyperons, short lived hadronic decays (particles with charm) and di-leptons. Fig. 2.3 shows the particle multiplicities times the branching ratio for the central Au+Au collisions at 25 AGeV as calculated using covariant hadronic transport approach HSD. These data points were calculated using either the transport code [26] or the thermal model based on corresponding temperature and baryon-chemical potential [27]. The calculations predict that the di-leptonic decays of low-mass vector mesons are 6 orders of magnitude less produced than pions. Mesons containing charm quark are about 9 orders of magnitude less produced than pions at 25

AGeV (Au+Au central collision). Due to the low production yield and multiplicities for the di-leptons and mesons with charm quarks, CBM is designed to run at high reaction rates of 100 kHz up to 10 MHz. At rates above 100 kHz a high level trigger has to be used in order to reduce the rate to the archiving rate. In simultaneous a suppression factor of about 500 has been achieved for the di-leptonic decay of J/ψ mesons ¹.

2.3 Physics case and observables

The envisaged list of observables and physics program of the CBM experiments could be summarised as follows:

1. The equation-of-state of baryonic matter at neutron star densities.
 - (a) Collective flow - At SIS-100 energies, the most significant observable is the collective flow of hadrons (including the strange particles) which is expected to reflect the onset of the de-confinement. It is also expected to be sensitive to the equation-of-state of nuclear matter at the early stage of the reactions.
 - (b) Multi-strange hyperons - At SIS-100 energies, excitation functions of multi-strange hyperons shall provide information about the density of the fireball.
2. In-medium properties of hadrons.
 - (a) Vector mesons - It is expected that chiral symmetry restoration will modify the in-medium properties of hadrons. This information could be extracted from the in-medium mass distribution of the vector mesons measured via their leptonic decays. ($\sqrt{s_{NN}} = 2 - 45$ AGeV range and for different collision systems)
 - (b) Charmed mesons - In medium properties of the hadrons can also be extracted from the yield and transverse mass distribution of the charmed hadrons as a function of collision energies at SIS-100 and SIS-300.

¹The plot for the multiplicities times the branching ratios for the various observables is taken from the ref. [28].

3. Phase transitions from hadronic matter to quarkyonic or partonic matter at high net-densities.

- (a) Leptons - Since leptons are penetrating probes they could carry information concerning the dense fireball at both SIS-100 and SIS-300.
- (b) Strange and charmed particles - It is anticipated that the baryonic densities at SIS-100 energies could reach up to 7 times or saturation level. Phase transition signatures could be extracted from the excitation function of yields, spectra, and collective flow of strange and charmed particles in heavy-ion collisions from 6-45 AGeV (SIS-100/SIS-300)
- (c) Lepton pairs - Phase transition from hadronic to quarkyonic or partonic matter could also be identified using the yields and spectra of the lepton pairs produced at high densities. In particular, dileptons with invariant masses between 1 and 2 GeV/ c^2 reflect the temperature of the fireball, and hence open the possibility to measure the "caloric curve" when varying the beam energy.
- (d) Fluctuations - High precision measurement of even-by-event fluctuation of the conserved quantities like baryon, strangeness, net charge etc. as a function of beam energy from 6-45 AGeV for both SIS-100 and SIS-300.

4. Hyper-nuclei, strange di-baryons and massive strange objects.

- (a) Theoretical models predict that single and double hyper nuclei, strange di-baryons and heavy multi-strange short-lived objects have maximum production yield in the SIS-100 energy range.
- (b) These forms of metastable or even stable objects with strangeness has been proposed long ago by Bodmer in 1971 [29] as collapsed states of matter either consisting of strange baryons or strange quarks. The summary of Hyper-nuclei which was already observed before can be found in the Ref. [30; 31; 32]. If these multi-strange objects decay in the form of charged hadrons, they could be easily detected via their decay products. [33]

-
5. Charm production mechanisms, charm propagation, and in-medium properties of charmed particles in (dense) nuclear matter.
- (a) Measurement of the hadronic decays of open charm in the CBM energy regime constitutes a particular challenge because of the very low multiplicity of charmed hadrons. For the study of charmonium like states, the CBM experiment will trigger on high energy lepton pairs for reaction rates up to 10 MHz.
 - (b) The CBM experiment will measure open charm in proton-nucleus collisions at FAIR energies (no data available). Moreover, CBM will also measure charmonium production in nucleus-nucleus collisions at different energies (no data below top SPS energies)

The experimental task of the CBM is to measure precisely all these observables in A+A, p+A and p+p collisions, as a function of collision energy and system size, with high precision and statistics, and to search for discontinuities in the aforementioned dependencies which would signal for example a first-order deconfinement phase transition. This vast physics program will be carried out by performing nuclear collisions at unprecedented high interaction rates.

2.4 CBM detectors

The CBM at FAIR is a fixed target heavy-ion experiment which includes a Micro Vertex Detector (MVD), a Silicon Tracking System (STS), a Ring Imaging Cherenkov Detector (RICH), a Muon Chamber System (MUCH), a Transition Radiation Detector (TRD), a Time-of-Flight detection system (TOF) using resistive plate chambers, a Shashlik type Electromagnetic Calorimeter (ECAL) and a Projectile Spectator Detector (PSD) [34]. A 3D-CAD model representing the various detector systems in the CBM experimental set up is shown in fig. 2.4. The experimental strategy is to perform systematic and multi-differential measurements of all particles produced in nuclear collisions with unprecedented precision and statistics. The CBM detector will identify hadrons and leptons in nuclear collisions with up to 1000 charged particles in CBM acceptance at collision rates

up to 10 MHz. The experiment will be optimized in particular for the detection of rare probes, like hadronic decays of D-mesons and leptonic decays of light vector mesons, that can yield information on the dense phase of the collisions. The challenge is to accomplish in this environment high-resolution charged particle tracking, momentum measurement and secondary vertex selection with a silicon tracking (STS) and vertex detection system (MVD), the central component of the CBM detector. The system requirements include a very low material budget, radiation tolerant sensors with high spatial resolution, and a fast readout to cope with free streaming data.

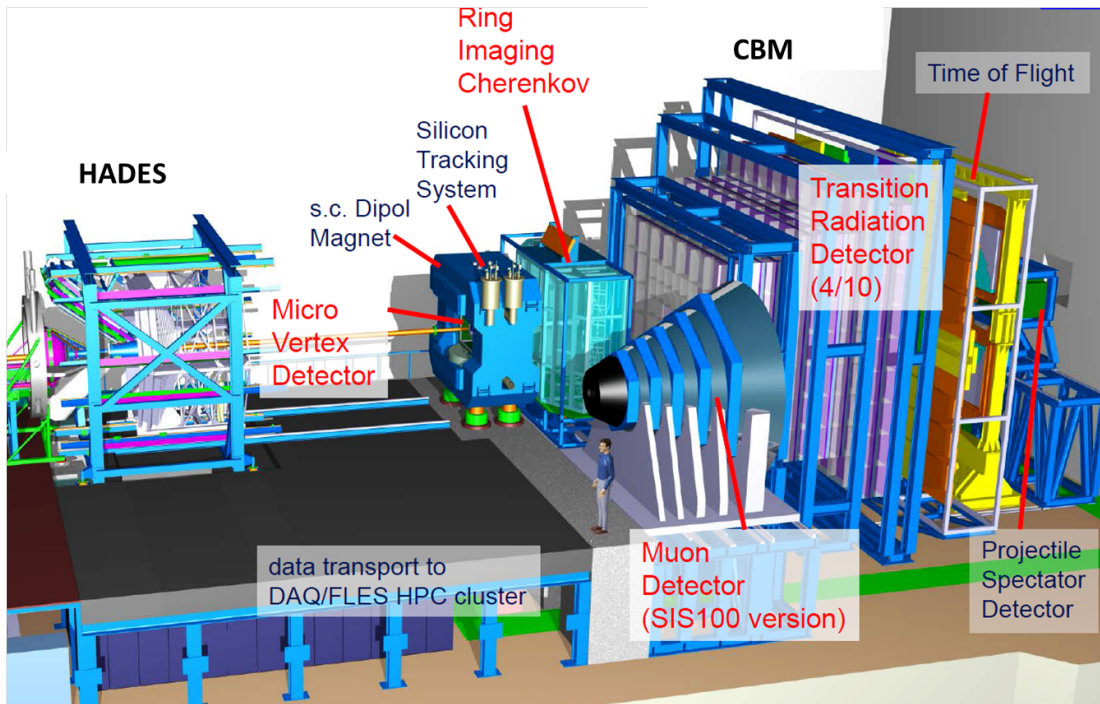


Figure 2.4: Schematic representation of the HADES detector and the CBM experimental set-up along with its components.

The technical challenge for the detector system as shown in fig. 2.4 is to identify both hadrons and leptons and to filter the rare probes. The measurements will be performed via nucleus-nucleus, proton-nucleus and proton-proton interactions at different beam energies. Proton-proton interactions are required for the baseline determination ("normal nuclear matter"). For the particle identification, especially multi-strange hyperons, hyper-nuclei, vector mesons decaying

into lepton pairs and particles with charm quarks the background suppression is an important issue [34]. As there is no simple trigger signals, a free-streaming read-out electronics has to be used. The track reconstruction of each individual particle passing through the detector system has to be made on-line and filtered with respect to the physics requirements.

In addition high speed data processing, transition and analysis using fast algorithms are prerequisites for such system. The essential factor is the data transport and computational throughput rather than the decision latency. The CBM detector system will provide both electron and muon detection systems in order to take advantage of both measurement methods. Muon and electron pairs created during particle decays will be measured during separate runs in order to control the systematic approach of the measurements. The acceptance of the detector systems as coming from the physics requirements is full 2π for φ (azimuth) and from 2.5° to 25° for Θ (polar angle). In electron configuration following detectors will be used: Micro-vertex Detector (MVD), Silicon Tracking System (STS), both placed in gap of 1 T superconducting magnet, then Ring Imaging Cherenkov Detector (RICH), Transition Radiation Detectors (TRD), Resistive Plate Chambers for time-of-flight measurements (TOF), Electromagnetic Calorimeter (ECAL) and Projectile Spectator Detector (PSD) as hadronic calorimeter. In muon configuration the RICH detector will be replaced by the Muon Detection System (MUCH) and ECAL will be removed [4].

Dipole magnet: The dipole magnet of CBM will be superconducting with a large aperture (Fig. 2.5). The coils (each with 1749 turns and cooled by liquid helium) will provide a magnetic field with total bending power 1 Tm. The total weight of the magnet will be 160 tons. The magnet is designed to hold both four layers Micro-Vertex Detectors (MVD) and eight stations of Silicon Tracking Stations (STS) for the purpose for efficient vertex identification and tracking of charged particles [34].

Micro-Vertex Detector (MVD): Micro-Vertex Detector will be built from of Monolithic Active Pixel Sensors (MAPS) with pixel sizes $18.3 \times 18.3 \mu m^2$ and $20 \times 40 \mu m^2$. Depending on the pixel size the hit position resolution varies from

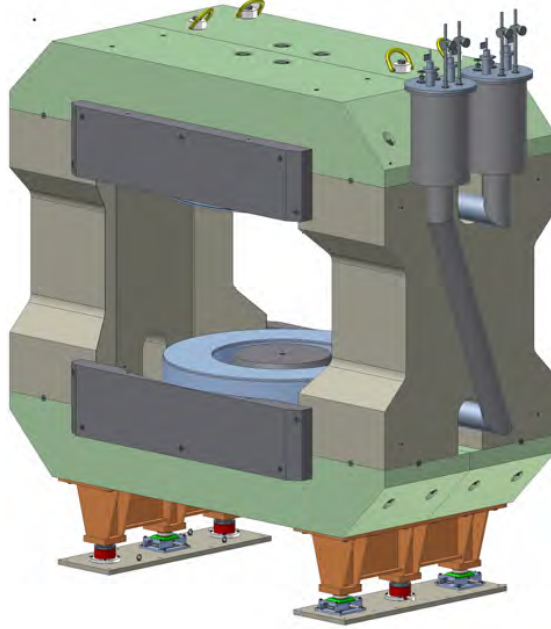


Figure 2.5: A schematic engineering view of the CBM magnet. The magnet is designed to hold the 3 layers of MVD and the 8 STS detector stations.

$3.5 \mu\text{m}$ to $6 \mu\text{m}$ resulting in secondary vertex resolution of $50 \mu\text{m}$ to $100 \mu\text{m}$ along the beam axis (Fig. 2.8 (inside orange box)). The detector will consist of four stations placed 5, 10, 15, and 20 cm downstream of the target in a vacuum box. The material budget of sensors in each of the stations together with cooling and support structures is kept between $300 \mu\text{m}$ and $500 \mu\text{m}$ of silicon equivalent [34]. The hardness against non-ionizing radiation is required to be above 10^{13} neutron equivalent per cm^2 (n_{eq}/cm^2) and for ionizing radiation to be above 3 Mrad. The read-out time of the sensors is expected to be below $30 \mu\text{s}$. The currently tested chip, called MIMOSA-26, fulfils most of the requirements giving the hit position resolution of about $4 \mu\text{m}$, and having radiation hardness for non-ionizing radiation well above $10^{13} n_{eq}/\text{cm}^2$ [34]. A prototype Micro-Vertex Detector are pictured in fig. 2.6, and the MVD detector boards under laboratory test is shown in fig. 2.7.

Silicon Tracking System (STS): Following the MVD downstream of the target is the Silicon Tracking System (STS), also placed inside the aperture of the

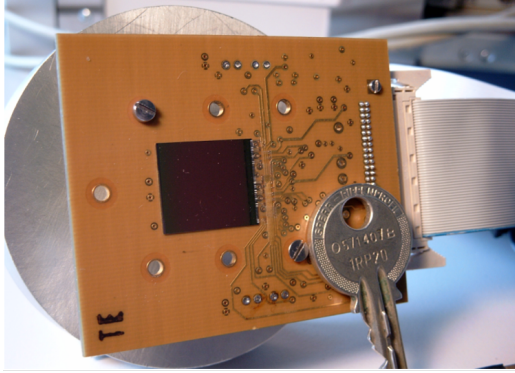


Figure 2.6: A prototype Micro-Vertex Detector boarded on a printed circuit board for test.



Figure 2.7: A photograph of prototype Micro-Vertex Detectors under test in the laboratory.

dipole magnet (Fig. 2.8). The STS has an acceptance between polar angles of 2.5° and 25° . This will provide the track reconstruction and momentum determination of the charged particles. The STS will be built out of 8 tracking layers placed from 30 to 100 cm distance from the target equipped with double-sided micro-strip silicon sensors. To obtain required momentum resolution $\Delta p/p \approx 1\%$ the stations have to have an ultra low material budget (Fig. 2.9). Thus, the front-end electronics will be placed outside the active area of the STS, and the sensors will be interconnected to the read-out chip via low-mass cables [34]. The stations are arranged in four doublets. The strips of the sensors are 2, 4, 6 cm and 12 cm when two sensors with 6 cm strip length are daisy-chained. Each of the sensors comprises 1024 channels with a strip pitch $58 \mu m$. The stereo angle is 7.5° . The thickness of the used sensors will be $300 \pm 15 \mu m$. The sensors and the electronics is CO_2 -cooled by the cooling plates around the ladders(blue) [34].

Ring Imaging Cherenkov Detector (RICH): When CBM will operate in electron configuration the Ring Imaging Cherenkov Detector is placed downstream of the STS. The RICH together with the TRD, is used for the identification of electrons and the suppression of pions in the momentum range up to 10 GeV/c [4]. The RICH gas radiator (length 1.7 m) consists of CO_2 where the pion threshold for Cherenkov is 4.65 GeV/c. The Cherenkov radiation will be reflected by mirrors built from 72 mirror tiles with a curvature of 3 m radius

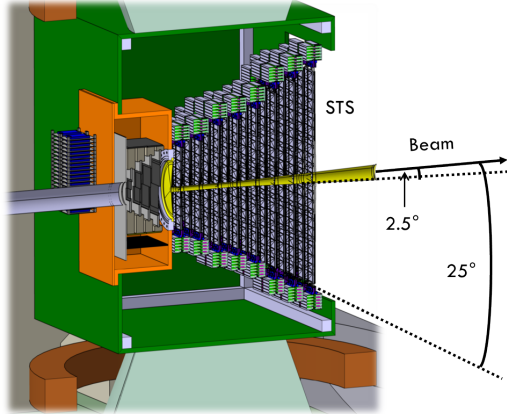


Figure 2.8: Engineering view of a cross section view of STS detector stations lined up for the CBM experiment. The STS is enclosed inside a magnet.

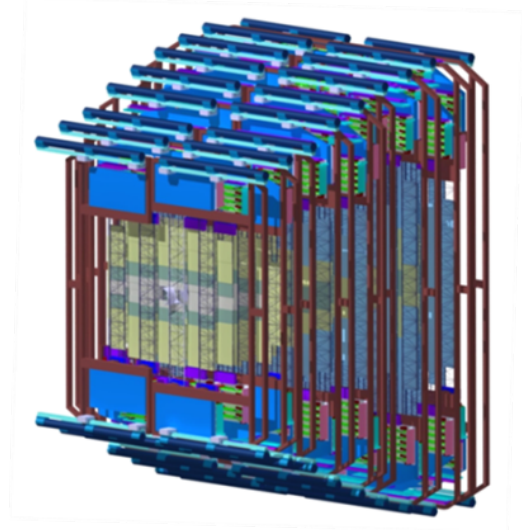


Figure 2.9: Engineering view of one of the stations composed of ladders piled up with silicon sensors (centre) and cooling plates (blue).

and $\text{Al}+\text{MgF}_2$ reflective coating (Fig. 2.10). The photo-detector plane where photons will be reflected will be built from Multi-Anode Photo Multiplier Tubes (MAPMT) and will be shielded from the magnetic field [34]. A photograph of the real-size RICH detector prototype detector wall under test at CERN beam-time is shown in fig. 2.11.

Muon Chamber System (MUCH): In the muon configuration of the CBM experiment the STS is followed by the MUon CHamber detector system. The main role of the MUCH is to detect the muon pairs from the decays of J/Ψ and light vector meson in an environment of high particle densities [4]. The MUCH detector system will provide particle tracking and perform momentum dependent muon identification using an instrumented hadron absorber. The absorber will be segmented into several layers with triplets of tracking Gas Electron Multiplier (GEM) detectors in the gaps [34]. The design consists from six absorber layers made of iron and 18 gaseous tracking chambers. These are divided into sectors as shown in fig. 2.12. The expected hit rates reach 3 MHz/cm^2 in the first detector system. At SIS-100 a MUCH start version will be used which will consist from

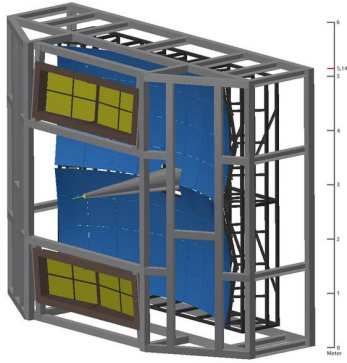


Figure 2.10: Engineering view of the RICH Detector (blue) with supported structures (grey) for the CBM experiment



Figure 2.11: Photograph of constructed 3 layers of RICH Detector walls under test during CERN beam-time

three chamber triplets with three absorbers [34]. A photograph of the prototype sectors of the Muon Chamber GEM detectors under test in VECC kolkata is shown in fig. 2.13.

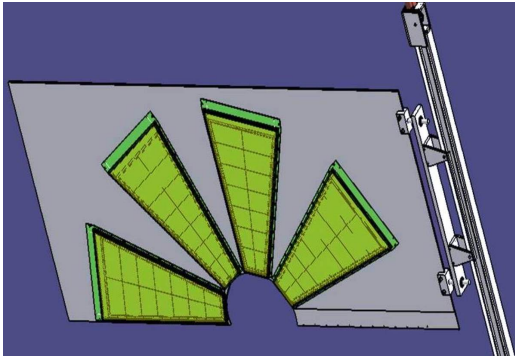


Figure 2.12: Engineering view of the Muon Chamber Detector Sector for SIS-100

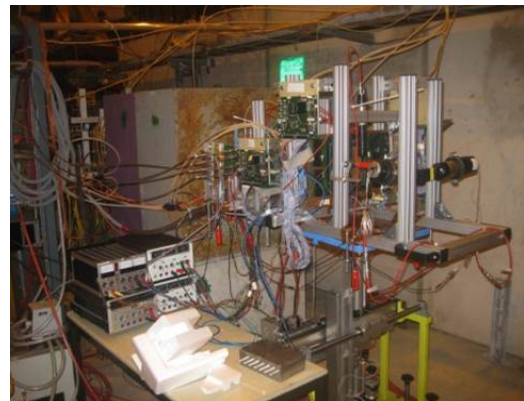


Figure 2.13: Photograph of constructed MUCH prototype module under test in VECC Kolkata

Transition Radiation Detector (TRD): The Transition Radiation Detector will be used for identification of electrons and pions with $p > \text{GeV}/c$ ($\gamma \geq 1000$) [4]. It will consist out of three transition radiation detector stations. The TRD

readout will be realized in rectangular pads providing resolution of $300 \mu\text{m}$ - $500 \mu\text{m}$ across and 3 mm - 30 mm along the pad [34]. Every second transition radiation layer is rotated by 90° . The pion suppression factor obtained will be well above 100 at electron identification efficiency 90%. The expected hit rate in TRD is up to 100 kHz/cm^2 . In the SIS 100 setup only one station of TRD will be used as an intermediate tracker between the STS and the Time-of-Flight wall 2.14 [34]. A Photograph of the prototype TRD set-up under test in CERN is depicted in fig. 2.15.

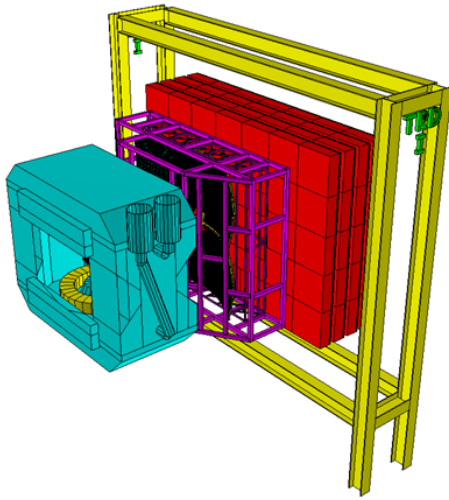


Figure 2.14: Engineering view of the Transition Radiation Detector (TRD) for SIS-100

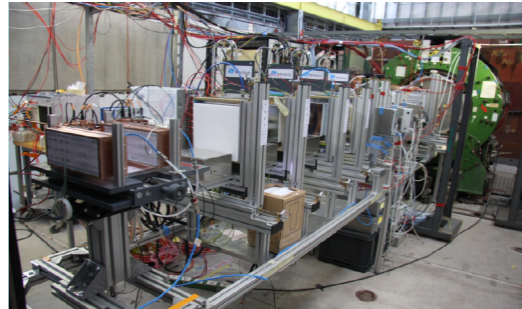


Figure 2.15: Photograph of constructed TRD prototype module under test in CERN

Time-of-Flight Wall (TOF): An array of Timing Multi-gap Resistive Plate Chambers will be used for hadron identification via time-of-flight measurements [4]. It will cover an area of 120 m^2 using pad structures for the inner areas and strip structures for the outer zones. The hit rates in the inner zones are expected to reach 25 kHz/cm^2 and 10 kHz/cm^2 in the outer areas. The required time resolution of the chambers is 80 ps . The engineering view of the TOF wall and a constructed TOF Module is shown in fig. 2.16 and 2.17) [34].

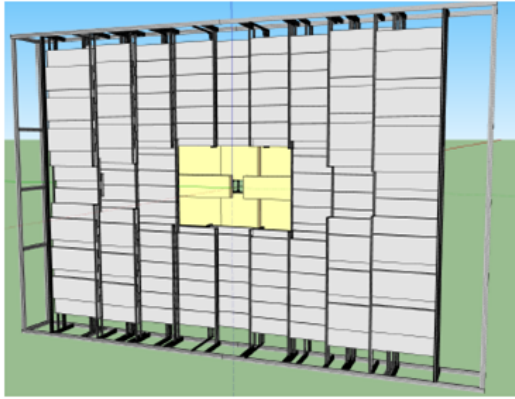


Figure 2.16: Engineering view of the Time-of-Flight (TOF) detector



Figure 2.17: Photograph of constructed TOF wall under test

CBM calorimeters: In the CBM detector the Electromagnetic Calorimeter (ECAL) will be used to measure photons and neutral mesons (π^0, η) decaying into photons (Fig. 2.18) [4]. The Projectile Spectator Detector (PSD) will provide measurements of centrality and reaction plane (Fig. 2.19). It is designed to determine the number of non-interacting nucleons from a projectile nucleus in nucleus-nucleus collisions. Both calorimeters have a "shashlik" structure build from lead/scintillator layers.

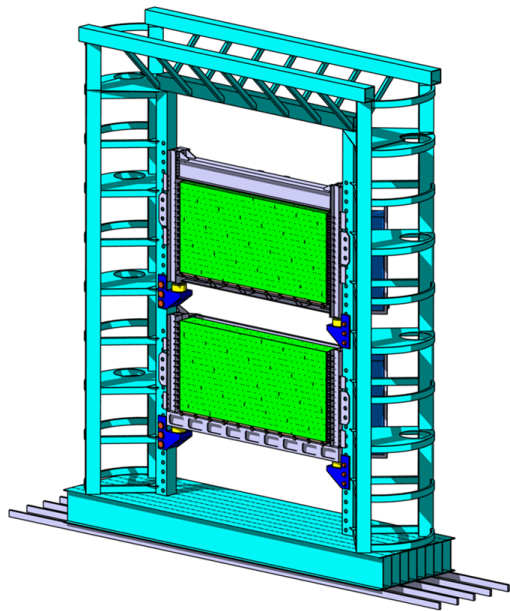


Figure 2.18: Engineering view of the ECAL detector



Figure 2.19: Photograph of construction of super module of PSD for the beam test at CERN

Chapter 3

Silicon Tracking System

The silicon tracking systems are widely used in many experiments. The first dedicated silicon tracker was used in NA11/NA32 experiments for the charged particle tracking and vertex measurements [35; 36; 37]. After its successful operation the same was implemented in many forthcoming experiments in high-energy physics. For example, LEP, DELPHI, CDF, AMS, D0, FERMI, HERA-B, ATLAS, CMS and many other experiments have successfully used the technique of segmented silicon detectors for charged particle tracking. A comprehensive overview of the history of silicon based tracking detectors can be found in [38]. The evolution and usage of the silicon in high-energy physics detectors is unprecedented. The total detector surface in the NA11 experiment increased from $0.005 m^2$ to almost $110 m^2$ in the CMS experiment at LHC, CERN. A comprehensive summary of the evolution of silicon detectors can be found in Ref. ¹ [39]. The CBM collaboration is building a silicon tracker with forward rapidity in a small volume using state-of-the-art technology to read more than 2 millions of channels with fast and free-streaming read-out electronics. The challenge is to develop low mass double-sided silicon micro-strip sensors. The technical challenges, constraints, feasibility studies, hit detection, reconstruction and tracking performance is discussed in the preceding section.

The Silicon Tracking System (STS) is the core tracking detector system of the CBM experiment. The STS is designed to be positioned in the field of a

1

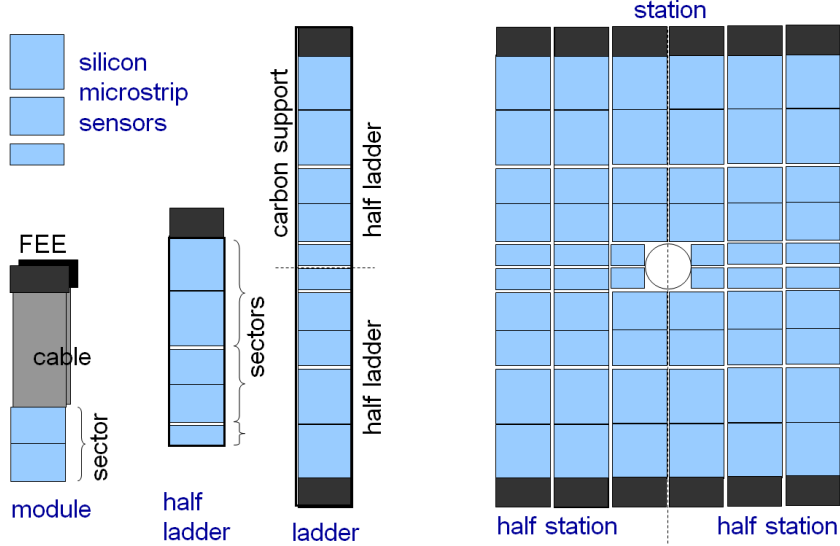


Figure 3.1: Conceptual design of the tracking station with building blocks such as ladder structure and modules.

large aperture superconducting dipole magnet of strength 1 T. The STS will be approximately 1 m long and will be housing a thermally encapsulated 2 m^3 volume. The detector system is planned to operate both in the modular start version with SIS-100 ion beam energies of the range 2-14 AGeV (proton up to 29 GeV), later with SIS-300 ion beam energies up to 45 AGeV (proton up to 90 GeV) [40]. The main task of the STS is to provide track reconstruction and momentum information of the charged particles. As stated in section 2.3, the multiplicity of rare observables is several order of magnitude less than the bulk observables. This constraints the requirement for detection of these rare observables - which in turn pushes the reaction rates up to 10 MHz. The multiplicity of the charged particles is up to 700 per event for Au+Au central 25 AGeV covering the polar angles $2.5^\circ < \Theta < 25^\circ$. The technical challenges faced by the silicon tracking detector project at the CBM experiment is discussed in section 3.1.

The STS is composed of 8 stations in a ladder-type structure having silicon micro-strip detectors as schematically in Fig. 3.1. A detailed 3-dimensional computer aided design (CAD) model of the silicon tracking system is shown in fig. 3.2 which consists of the detector modules mounted on different ladders on eight con-

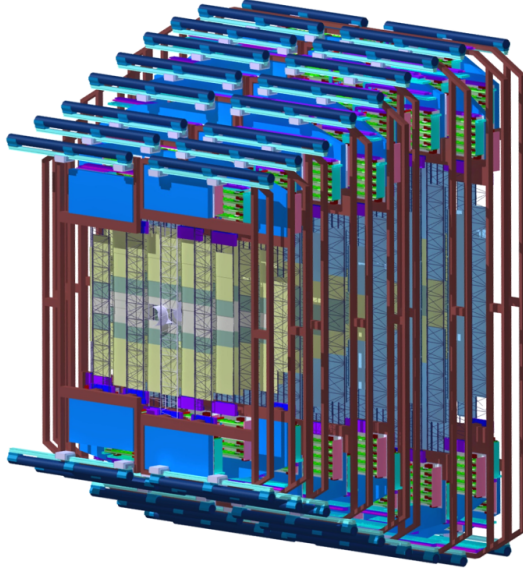


Figure 3.2: CAD design of the Silicon Tracking System with building blocks such as ladder structure and modules.

secutive tracker stations. The 8 STS stations are located downstream from the fixed-target at a distance of 30 cm to 100 cm (cf. fig. 3.3 (a)). The required momentum resolution is of the order of 1% and single hit spatial resolution is of the order of $25 \mu\text{m}$. This performance requires an ultra low material budget (expressed in radiation length), achieved by state-of-the-art ultra thin low-mass micro cables which connect the sensor to the front-end electronics located outside the active area of the detector. The frontal cross section of the engineering CAD design of the stations, shown in Fig. 3.3 (a) with the STS enclosed inside the H-shaped superconducting magnets, four micro-vertex detector (MVD) system in front of the eight silicon tracker stations (STS). Moreover, Fig. 3.3 (b) shows a tilted 3D view to the whole STS + MVD set-up enclosed in the magnet.

In total 1220 sensors of three sizes will be connected to more than 14000 read-out ASICs and about 2.1 million channels are to be read. The STS consists of total 106 ladders of 8 different types. Each Ladder consists of different modules, the STS comprises of about 900 modules of 25 different types. The active volume of the STS is built with double-sided silicon micro-strip sensors mounted over lightweight carbon fiber support ladders and read over ultra-light micro thin

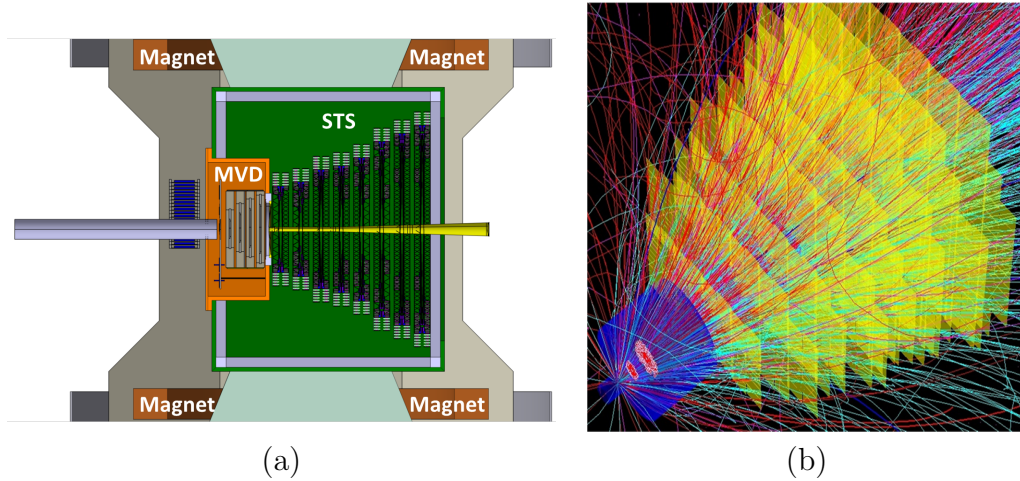


Figure 3.3: (a) An Engineering model of STS (Green), MVD (Orange) and the H-Shaped superconducting magnet section (Brown) and (b) Tracks from a central 25 AGeV Au+Au collision overlaid with the GEANT simulation of the STS tracking stations.

cables. The STS is designed for hit finding efficiency of 100% and track reconstruction $\geq 95\%$ for momenta $\geq 1 \text{ GeV}/c$ at small polar angles. The double sided micro-strip sensors are $300 \mu\text{m}$ thick and radiation hard up to a fluence of $1 \times 10^{13} \text{ n}_{eq}/\text{cm}^2$ ($1 \times 10^{14} \text{ n}_{eq}/\text{cm}^2$) (expressed in 1 MeV neutrons equivalent) ¹ compatible to CBM physics program for SIS-100 (SIS-300) at FAIR.

3.1 Technical challenges for STS

The STS project being the core tracking detector system has to respect several design constraints which includes, the polar aperture within a range of 2.5° to 25° , low material budget, 100% track efficiency (at small polar angles) and a fast readout chip [34]. A read-out strip pitch of $58 \mu\text{m}$ is chosen to match the design constraint for the required spatial resolution. The STS is designed to cope with the charged particles rates of about $10 \text{ MHz}/\text{cm}^2$ and this reduces by two orders of magnitude in the outermost region of the active area of the STS. A fast

¹1 MeV equivalent neutron fluence is the fluence of 1 MeV neutron producing the same amount of damage in a detector material as induced by an arbitrary particle fluence with a specific energy distribution.

self-triggered ASIC based electronics is under development with a shaping time of less than 5 ns, nevertheless for early prototyping n-XYTER electronics [41] is used with a shaping time of 20 ns. The STS also requires 100 % single hit detection efficiency and momentum resolution of about $\Delta p/p \approx 1\%$ for particles at 1 GeV/c. A UrQMD-generated central Au+Au collision at 25 GeV per nucleon is used as an input to the GEANT study of the STS shown in Fig. 3.3 (b). The STS detectors have to be able to resolve the track of 1000s of the charge particles at high interaction rates. These sensors have to be operational in a radiation environment of about $1 \times 10^{13} n_{eq}cm^{-2}$ for SIS-100 and $1 \times 10^{14} n_{eq}cm^{-2}$ for SIS-300 at FAIR. Details concerning the Silicon Tracking System at the CBM experiment can be found in the approved Technical Design Report [34].

3.2 Hit reconstruction in STS

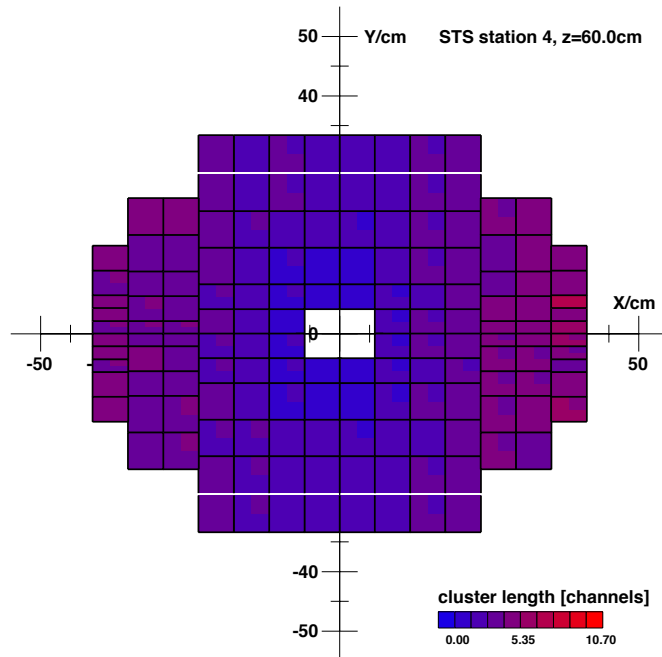


Figure 3.4: Cluster size distribution in the micro-strip sensors of STS station 4 for a threshold of 4000 electrons applied in the read-out electronics.

Simulations have been performed that include the complete chain of physical processes caused by the charged particles traversing the detector: from charge

separation in bulk silicon to digitization of the signal as an output. The first step of the STS hit reconstruction is performed by the cluster finder algorithms. A cluster is a group of adjacent fired strips in a sensor with a common time stamp. A constant signal threshold is applied for every channel. The total charge of a cluster is defined as the sum of the single strip signals. The cluster position is given by the centre-of-gravity method [42]. The cluster size distribution itself is presented in Fig. 3.4 for a threshold of 4000 electrons set in the read-out electronics. Due to inclination angles of tracks caused by the outwards bending magnetic field the cluster size increases towards the large polar angles.

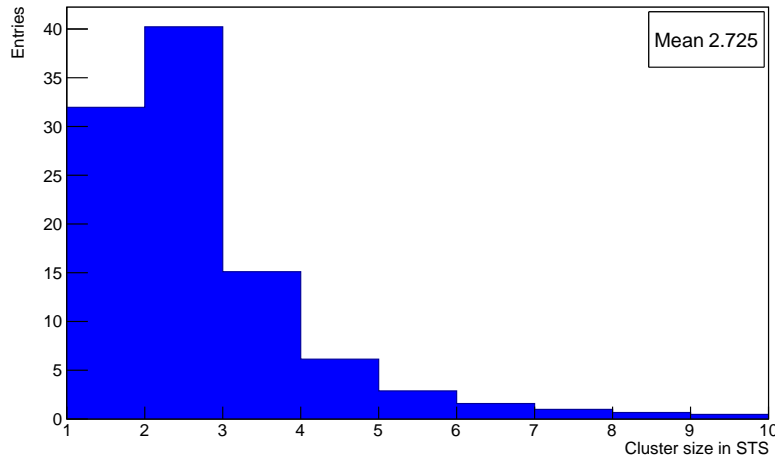


Figure 3.5: Distribution of cluster sizes for the entire STS.

3.3 Track reconstruction

The track finding algorithm in the STS detector system which is operated in an inhomogeneous magnetic field is based on the Cellular Automaton (CA) method [43]. Subsequent track and vertex fitting makes use of the “Kalman Filter” (KF). At first a set of track segments (tracklets) from hits on the neighbouring stations is created using the algorithms. A set of cuts which reflects the geometrical acceptance of tracks in STS (for e.g., forward tracks with minimum 4 hits and momentum exceeding 100 MeV/c), is applied to create tracks with enough hits to be reconstructed. Then the Kalman Filter based track fitting procedure is

used and a χ^2 fit is calculated to combine and reject tracks accordingly. The propagation of the tracks in an inhomogeneous magnetic field is described by a complex formula [44]. An example of UrQMD generated central Au+Au collisions at 25 AGeV projectile energy reconstructed with the STS is visualized in Fig. 3.6. The evaluation of the track reconstruction performance is based on

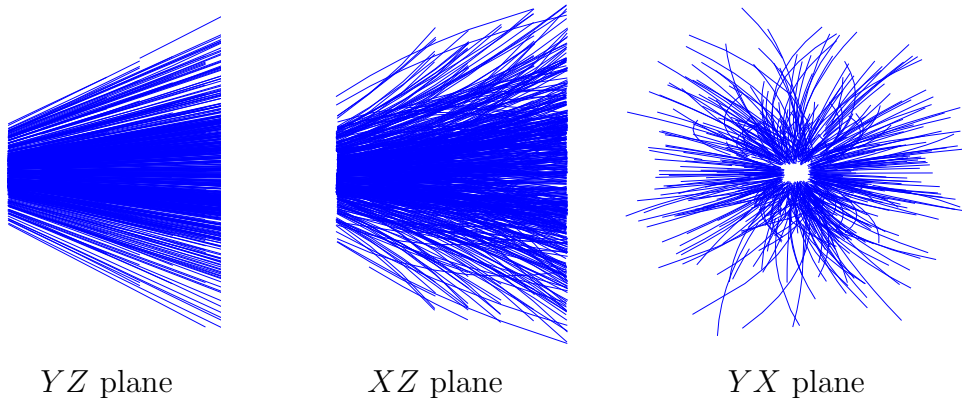


Figure 3.6: Display of reconstructed tracks from a central Au+Au collision at 25 AGeV projectile energy, shown in three different projections.

UrQMD central Au+Au events of 25 AGeV. The reference primary tracks (tracks from the particle produced close to interaction point) are reconstructed with efficiencies up to 96% depending on the particles momentum and the reconstruction efficiency of the secondary tracks (tracks from the decayed products) reaches up to 90% shown in Fig. 3.7. The momentum resolution obtained for primary tracks is shown in Fig. 3.8.

3.4 Particle identification

An important task of the STS is to precisely reconstruct weak decay topologies in order to measure strange and multi-strange hyperons. For this purpose, a dedicated software package (KF Particle) based on the Kalman Filter procedure was developed which reconstructs secondary vertices of track pairs or track multiplets with as high precision allowed by the high granularity of the STS. Geometrical (distance of closest approach) and topological (back-pointing of the mother track to the collision vertex) cuts allow to substantially reduce the random combinatorial background from primary tracks. The procedure can be repeated

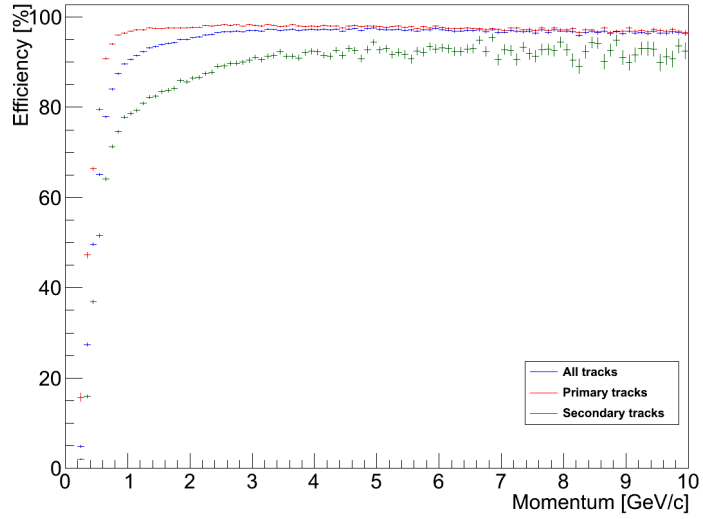


Figure 3.7: Track reconstruction efficiency in the STS as a function of the momentum for all tracks in central Au+Au at 25 AGeV projectile energy.

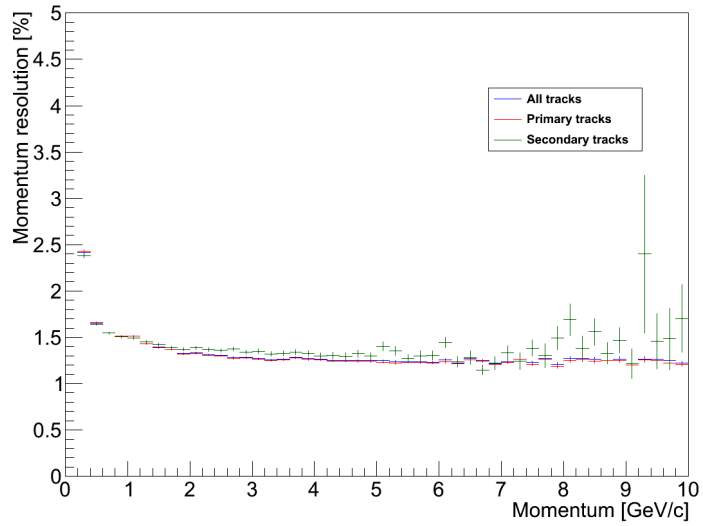


Figure 3.8: Momentum resolution in the STS as a function of the momentum for all tracks in central Au+Au at 25 AGeV projectile energy.

to reconstruct entire decay chains. In Fig. 3.9 simulated invariant-mass spectra for the decays are shown for $\Lambda \rightarrow p\pi^-$, $\bar{\Lambda} \rightarrow \bar{p}\pi^+$, $\Xi^- \rightarrow \Lambda\pi^-$ and $\Omega^- \rightarrow \Lambda K^-$ from 1×10^6 fully reconstructed central Au+Au collisions events at 25 AGeV. In both cases, a clear separation of signal from combinatorial background is obtained; the experiment is even sensitive to the rare Ω^- close to its production threshold. The same measurement technique will be applied for D mesons, but is

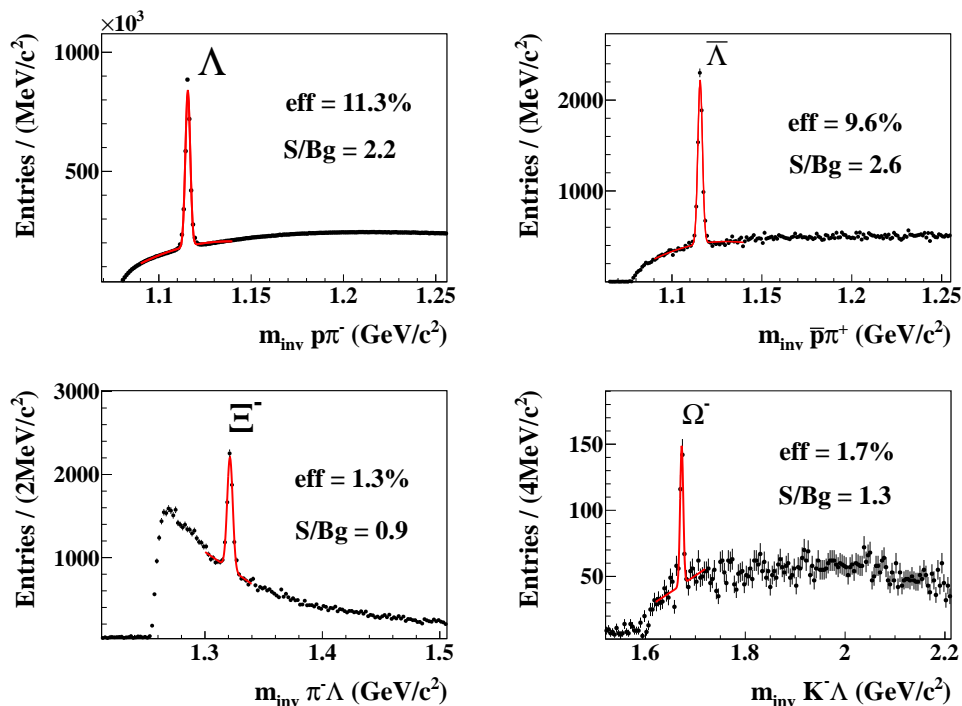


Figure 3.9: Invariant mass spectra for the hyperon decays: $\Lambda \rightarrow p\pi^-$ (left) $\bar{\Lambda} \rightarrow \bar{p}\pi^+$, $\Xi^- \rightarrow \Lambda\pi^-$ and $\Omega^- \rightarrow \Lambda K^-$ (right) central Au+Au collisions at 25 AGeV. p, π^-, K^- were identified by the TOF detector at $z = 10$ m with a time resolution of 80 ps. The simulated statistics results to 1×10^6 events at 25 AGeV.

much more challenging because of their extremely low multiplicities in the order of 10^{-5} per collision and short decay lengths ($c\tau = 312 \mu\text{m}$ for D^\pm and $123 \mu\text{m}$ for D^0). The STS detector alone is not capable of resolving displaced vertices on this scale. For the measurement of open charm, it will thus be operated together with a dedicated Micro Vertex Detector (MVD), built from silicon pixel sensors and located between the target and the STS (see Fig. 3.3(a)). Tracks are

first reconstructed in the STS and then extrapolated towards the MVD, where the corresponding high-precision pixel hits are associated. The combined MVD + STS system allows a reconstruction of displaced vertices with a precision of about $50 \mu\text{m}$ efficiently along the beam direction. This is sufficient to reconstruct the decays $D^0 \rightarrow K^- \pi^+$ and $D^+ \rightarrow K^- \pi^+ \pi^+$ and their charge conjugates as shown in Fig. 3.10. Detailed results concerning the tracking efficiencies and the physics performance concerning the CBM physics case could be found in the STS technical design report [34].

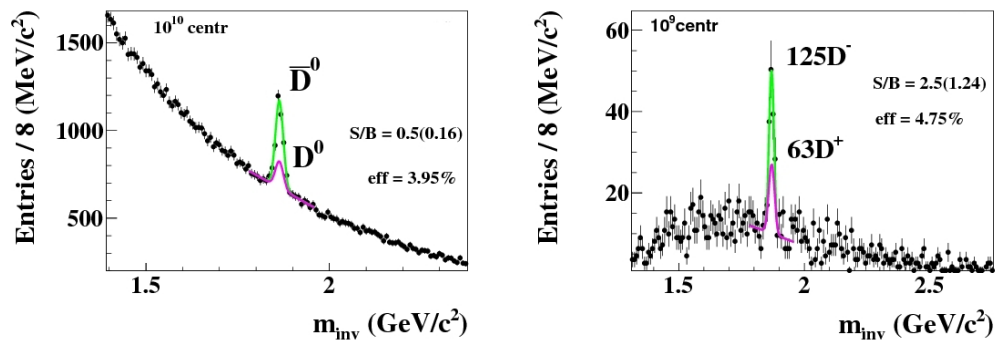


Figure 3.10: Invariant-mass spectra for the decays $D^0 \rightarrow K^- \pi^+$, $D^+ \rightarrow K^- \pi^+ \pi^+$ and their charge conjugates for 10^{10} and 10^9 central Au+Au collisions at 25 AGeV.

The results of the simulations indicate that the STS is capable of handling high multiplicity of tracks in the CBM collision environment. The physics performance studies demonstrate that the STS can reconstruct rare probes with good detection efficiency. The track reconstruction algorithms are in continuous development and we expect even better results in future.

3.5 Prototype sensors

The STS will be populated with double-sided silicon micro-strip sensors. These sensors will be mounted on a low-mass mechanical support structure made of carbon fibre-beams and will be read-out through a low mass multi-line fine-pitch flat cables by a front-end electronics located outside of the physics acceptance at the periphery of the STS stations.

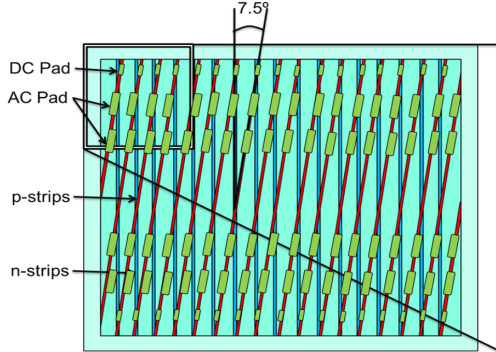


Figure 3.11: Schematic drawing of the 7.5 degree orientation of strips in prototype sensor

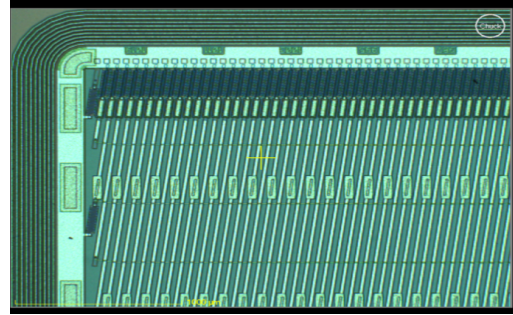


Figure 3.12: Photograph of a CBM05 prototype double sided silicon micro-strip sensor

Sensor specifications

The STS project considers double-sided silicon micro-strip sensors of different sizes. The silicon sensors are of type p-n-n structure. The strip length varies from 2 cm, 4 cm, 6 cm, 12 cm (daisy chained two sensors) depending upon the location on the STS ladder. These three types of sensors are $300 \mu\text{m}$ thick and has dimensions of $6.2 \text{ cm} \times 6.2 \text{ cm}$, $6.2 \text{ cm} \times 6.4 \text{ cm}$ and $6.2 \text{ cm} \times 2.2 \text{ cm}$ (see Figure. 3.11). The strips on p-side have a stereo-angle of 7.5 degrees (see Figure. 3.12). The double-sided sensors have 1024 strips per side per sensor to be read-out by front-end electronics. The strip pitch and width of the sensor are $58 \mu\text{m}$ and $18 \mu\text{m}$ respectively. Moreover, the sensor prototypes with smaller dimensions ($1.5 \text{ cm} \times 1.5 \text{ cm}$) with 256 strips on both sides orthogonal to each other have been produced along with large sensors for electrical characterization, thorough investigation and testing. The sensors are deemed to be radiation tolerant up to $1 \times 10^{14} n_{eq}/\text{cm}^2$ (equivalent to 1 MeV neutrons). A prototype sensor ($6.5 \text{ cm} \times 6.2 \text{ cm}$) tab-bonded to the read-out cable is shown in fig. 3.13.

The prototype sensors were produced from two vendors, namely, CiS Research Institute, Erfurt Germany [45] and Hamamatsu Photonics, Japan [46]. The chronological development of several prototype sensors have been enlisted in the technical design report [34].

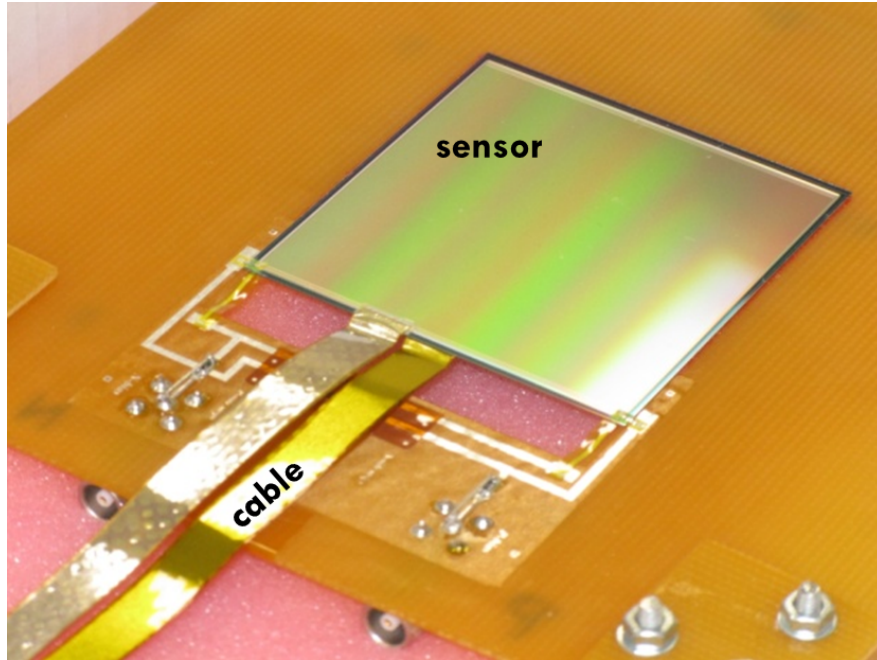


Figure 3.13: A prototype sensor tab-bonded to the read-out cable boarded on a printed circuit board.

Read-out cables

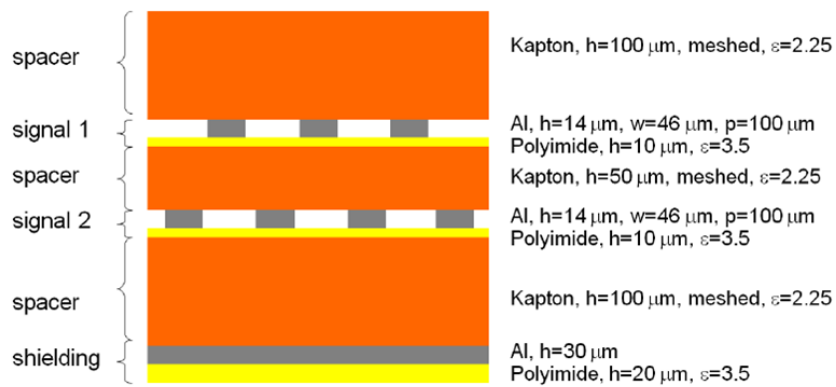


Figure 3.14: Schematic design of the prototype low-mass ultra thin read-out cables along with its parameters.

The STS project will employ state-of-the-art ultra-thin low-mass read-out cables for the signal transmission from the silicon sensors to the front-end elec-

tronics. The read-out cable for the STS must induce low mass budget into the tracking volume. The aluminium traces in the read-out cables are separated with a pitch of $116\ \mu\text{m}$ and the thickness of the total read-out cable is just $24\ \mu\text{m}$.

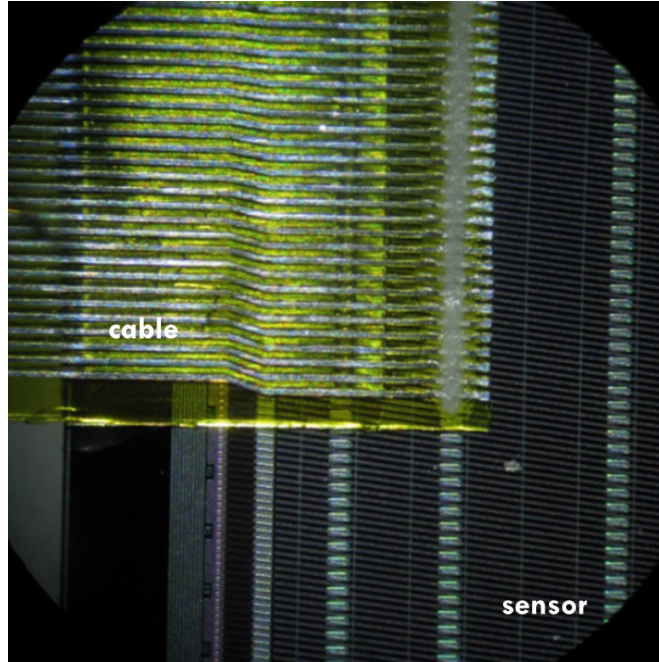


Figure 3.15: A photograph depicting the tab-bonded read-out cables on the sensors strips.

For a full size double-sided sensor, we need to attach 16 read-out cables to read 2048 channels. The read-out cables have two signal layers and one ground. Fig. 3.14 show the cross section of the read-out cable labelled with the design parameters and fig. 3.15 show a sensor tab-bonded to the read-out cable.

Front-end electronics

The STS project is utilizing the n-XYTER based chip for the front-end electronics. A dedicated front-end electronic chip is under development in collaboration with AGH Institute and Jagiellonian University Krakow, Poland. A test STS-XYTER prototype attached to 4 read-out cables is shown in fig. 3.16.

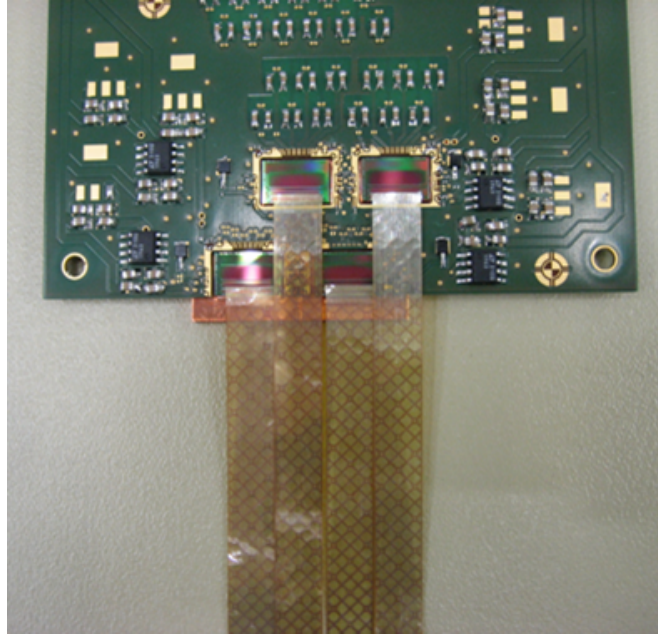


Figure 3.16: A photograph showing a test STS-XYTER prototype front-end electronics chip attached to 4 read-out cables.

Characterization and QA of prototype components

During the R&D phase as well as the pre-series and series production stage, the characterization of the silicon sensors, the front-end electronics, and the complete detector modules have to be performed. The present work reported in this thesis is confined to the development of procedures and techniques for the characterization and quality assurance of prototype sensors. It is evident that characterization of more than 1000 silicon micro-strip sensors and later of complete detector modules is very time consuming, and may damage the objects if not performed carefully. The aim of this project work can be divided into two parts:

- The first part is dedicated to develop a systematic procedure for the quality assurance (QA) for the double-sided silicon micro-strip sensors. This includes identification of various passive electrical tests for the prototype sensors and its frequency from the production to its assembly as a detector module. This part is reported and discussed in chapter 4.

-
- The second part is dedicated to characterization of more complex object like Detector Modules (Sensor + Read-Out Cables + Font-end Electronics). Therefore, an non-invasive photo-intrusive technique was developed which uses calibrated pulsed infra-red laser for the characterization and quality assurance. This part is reported and discussed in chapter 5.

Chapter 4

Characterization & QA of silicon sensors

A systematic procedure for the characterization [47] and quality assurance (QA) [48] has been developed for the prototype sensors. Moreover, a Laser Test System (LTS) for the QA has been developed as a next step to investigate uniformity, and integrity of the sensors (see chapter 5). The laser test system is equipped with pulsed infra-red laser to perform non-destructive tests of the detector modules (see section 5.5.2) which are the smallest non-repairable assembled unit of the STS.

The double-sided silicon micro-strip sensors need utmost care in production. The sensors which are received from the manufacturer have already been tested for the bulk properties. In order to be fail-safe some basic passive electrical characterization has to be performed. In this chapter, systematic electrical characterization and its application to quality assurance of the silicon sensors are discussed. The sensor needs careful characterization and investigation in order to understand its behaviour and help evaluating its operating condition for the experimental conditions expected at CBM. At the Detector Laboratory in GSI Darmstadt, one of our prime focus is to prepare systematic QA test procedures for our silicon sensors before mass production phase which is scheduled now to 2016.

Quality Assurance for silicon micro-strip sensors can be divided into three

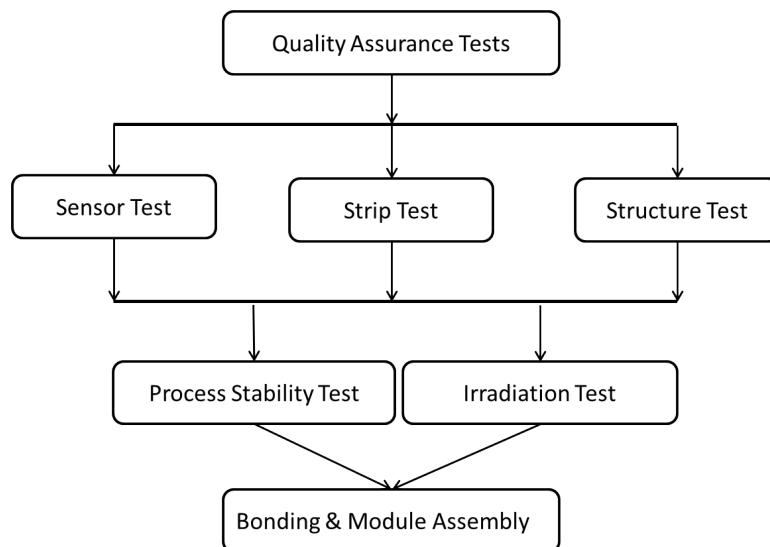


Figure 4.1: Steps in Quality Assurance tests for silicon micro-strip sensors.

main categories namely, “ Sensor Test ”dedicated to the investigation of overall condition, “ Strip Test ”dedicated to the investigation of performance at strip or inter-strip level, and “ Structure Test ”dedicated to investigate performance related to operation and efficiency. The steps in the quality assurance are explained by the schematic diagram in fig. 4.1. After the basic electrical characterization, qualified sensors are tested for investigating the production cycle with process stability tests and radiation hardness with irradiation tests. Finally, qualified sensors are made eligible for bonding and module assembly. The detector modules produced from the electrically qualified sensors are then again subjected to operation and performance test using the Laser Test System (discussed in next chapter). An ideal QA procedure must be smooth, non-invasive as much as possible, damage-less, time saving and possibility to gain maximum information out of each produced component. This requires a careful examination of all the tests. One needs to decide the number of such tests and its frequency required at each level of quality assurance. The QA tests includes visual/optical test, bulk leakage current characteristics and bulk capacitance characteristics categorized as “ Sensor Test ”, followed by pinhole test (or isolation test), coupling capacitance, strip current, bias resistance, inter-strip resistance and inter-strip capacitance categorized as “ Strip Test ”. This is then followed by current stability, hit detection

and detector efficiency test categorized “ Structure Test ”. The effect of radiation on leakage current and full depletion is also investigated which is categorized as ”Irradiation test”. The characterization and QA test on detector modules are discussed in the next chapter.

In the following section, systematic characterization procedures for the silicon micro-strip sensors for the STS are discussed.

4.1 Visual inspection

Visual inspection is an important test which is performed right after the sensors are delivered by the vendor. This test ensures that the sensor has no stray dust, no scratches or shorts within the active area of the sensor. These tests can be performed using a travelling microscope or a dedicated Wafer Prober in a clean room environment. This procedure provides a detailed understanding about any strip failures which develop as a result of inefficiency of the production cycle, etching process etc. The common strip failures observed are open strips, short-circuiting neighbouring strip, open implant, open implant at the via, open bias resistor, short-circuited bias resistors etc. Some of these strip failures are shown in Fig. 4.2,4.3 and 4.4 [for more information see ref. [49]].

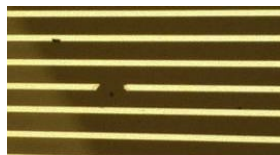


Figure 4.2: Broken strips or non-uniformity

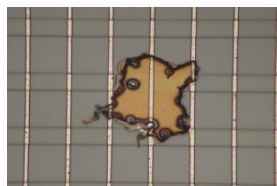


Figure 4.3: Scratch on sensor surface

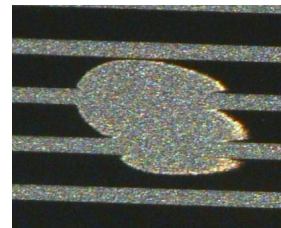


Figure 4.4: Shorts on the strips

4.2 Leakage current

The bulk measurement tests are the most crucial tests, which have to be performed on all sensors. This test provides information about the overall sensor

condition (including effect of ambient temperature), depletion voltage and operational voltage range. The leakage current is measured as a function of reverse-bias voltage applied across the micro-strip sensor using a voltage source [50].

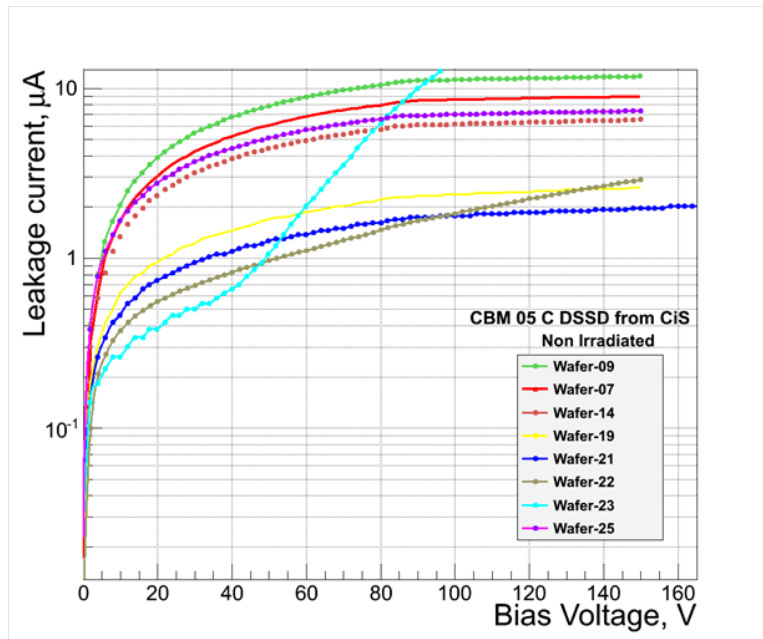


Figure 4.5: Leakage current measurement for CBM05 prototype sensor

This test has to be performed before the actual mounting of the sensor to a module. The sensor fulfils the acceptance criteria, if the average leakage current per strip is less than 5 nA. Measurement of one such leakage current test for the CBM05 prototype sensors (non-irradiated) is shown in Fig. 4.5.

4.3 Depletion voltage

Silicon micro-strip sensors require a reverse bias potential to create a region free from mobile carriers between the p-side and n-side. This region is called the depletion layer. The full depletion voltage (V_{fd}) is the bias voltage that extends the depletion layer in the entire depth of the bulk material of the sensor. This depletion region allows the charge liberated by a traversing ionizing particle which is then collected via the read-out electronics.

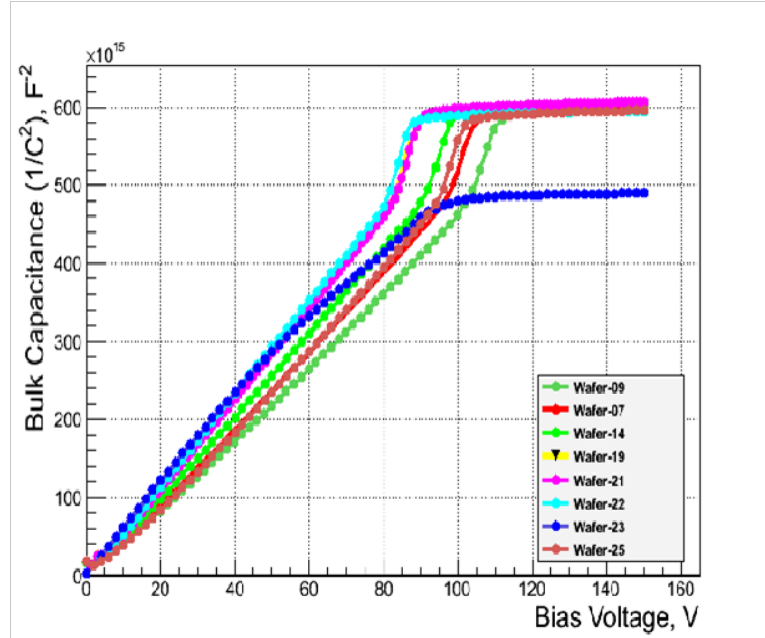


Figure 4.6: Depletion voltage measurement for CBM05 prototype sensor

To obtain the maximum charge collection efficiency (CCE), the silicon sensors are operated in an over depleted mode. The information of full depletion voltage (V_{fd}) is obtained from the knee point of inverse square capacitance as a function of biased voltage (Fig. 4.6). The depletion voltage provides crucial information about the operational voltage V_{op} . In most of the cases, it is recommended to operate the sensor at $V_{op} = V_{fd} + 20 V$.

4.4 Pinhole tests

The significance of pinhole test is to investigate the oxide layer between the AC pad (metal opening for bonding and read-out from strip) and DC pad (metal opening to access the implant for testing). Each prototype sensor is equipped with 4 AC pads and 1 DC pad per strip. A schematic representation of a pinhole is described in the Fig. 4.7.

The pinhole test is performed by connecting the AC and the DC pad of the same strip to a test voltage. The connections are made with the help of probe needles of the Wafer Prober. The current flowing between the AC and the DC

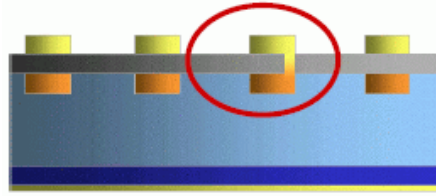


Figure 4.7: Schematic representation of pinhole in the implant

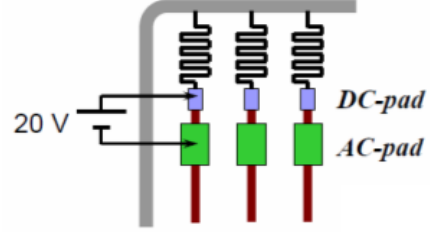


Figure 4.8: Circuit diagram for the pinhole test

pad is observed w.r.t the test voltage (see Fig. 4.8). When the insulation (between AC and DC pad) shows good performance, the leakage current does not exceed several fA. Whereas, if the leakage current observed is in the order of pA or more confirms the pinhole in the strip. This strip test is proposed to be performed for all sensors.

4.5 Coupling capacitance

The measurement of the coupling capacitance provides information on the signal transmission. The ratio of coupling and inter-strip capacitance affects the value of the signal transmitted to the read-out electronics. The coupling capacitance measurements were performed at the clean room environment.

A test voltage is applied to the AC and the DC pad of the same strip of a over depleted sensor to get coupling capacitance. Since, the coupling capacitance is strongly dependent on applied frequency above 1 MHz, this measurement is done using a low frequency (i.e., 10 kHz), see Fig. 4.10. During measurement, the neighbouring strips were connected to a virtual ground to avoid field distortions on the surface of the sensor (see Fig. 4.9). This strip test is proposed to be performed only at a maximum of 10% sensors. This is due to the fact that test involves mechanical pressure on the pads and increases the possibility of surface damage. Also, the measuring 10% sensors will provide enough confidence to predict the (non-)uniformity in the behaviour of a single batch of detectors.

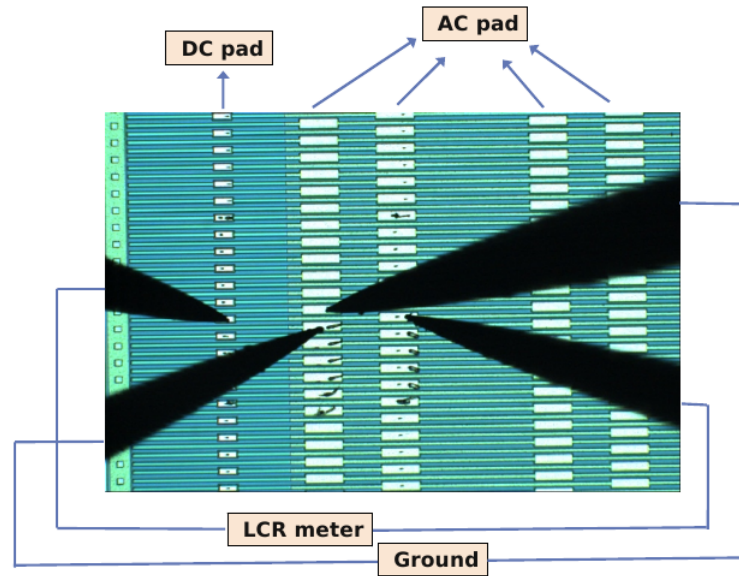


Figure 4.9: Coupling capacitance measurement: positioning of needles in the set-up

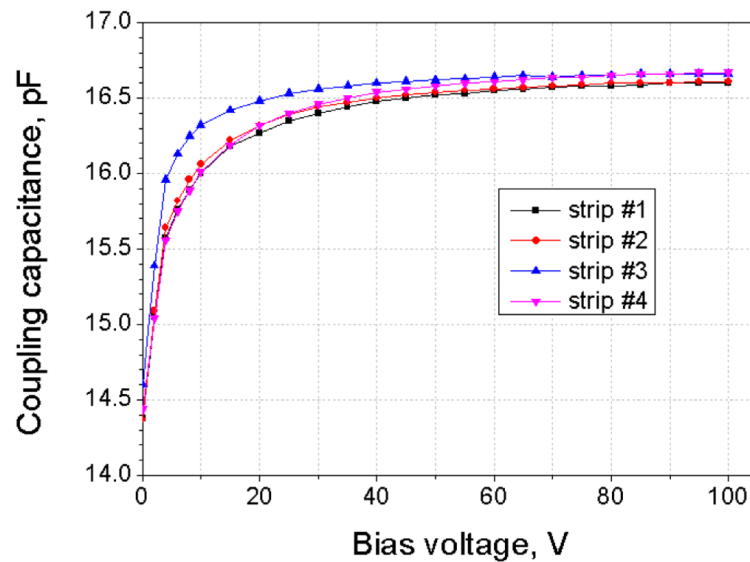


Figure 4.10: Coupling capacitance measurement at different strips for CBM02 prototype sensor

4.6 Inter-strip resistance

The value of the inter-strip resistance along with the inter-strip capacitance determines the number of strips over which the charge produced by an ionizing particle is distributed (clusters). Consequently, it describes the spatial resolution of the detector. The inter-strip resistance on the ohmic side of the sensor shows the quality of performance of the p^+ -stop structure. The measurement of inter-strip resistance is not trivial. In principle, the inter-strip resistance varies from sensor to sensor as it completely depends upon the production cycle, but the value is in the order of $100\text{ M}\Omega$.

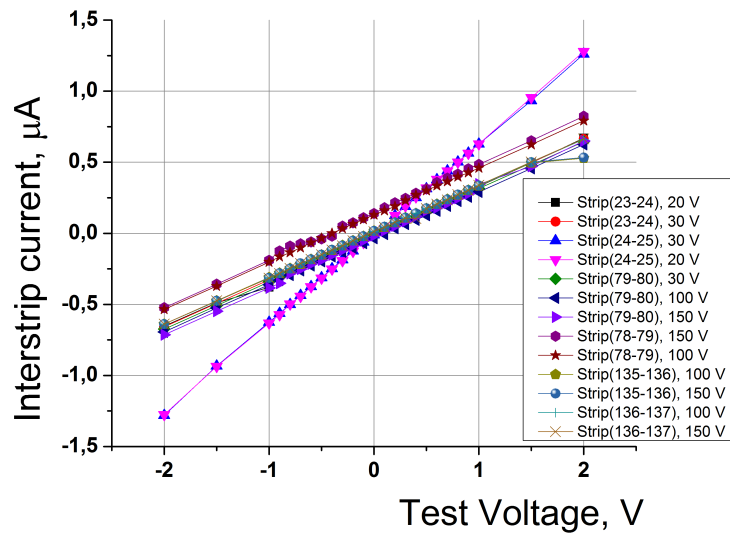


Figure 4.11: Inter-strip resistance measurement

As described in the previous section, it is mentioned that the following tests can only be performed with the biased sensor, and preferably in an over-depleted mode. A test voltage is introduced between two neighbouring strips ranging from $(-2\text{ V or }+2\text{ V})$ and the inter-strip current is measured. The inverse slope ($= \Delta V / \Delta I$) from current as a function of voltage gives the inter-strip resistance (see, Fig. 4.11). During the measurement, one should avoid the risk of distorting electrostatic fields within the inter-strip region of the sensor being under the full depletion voltage. This strip test is proposed to be performed only at a maximum

of 10% sensors. Also, the measuring a randomly selected 10% sensors will provide enough confidence to predict the (non-)uniformity in the behaviour of a single batch of detectors.

4.7 Inter-strip capacitance

In double-sided, AC-coupled silicon micro strip detectors, the signal-to-noise ratio is a function of detector capacitance. The coupling capacitance influences the signal strength and the inter-strip capacitance along with back plane capacitance affects the noise level. In addition, the resistance of the metal strip can influence the signal strength for fast shaping electronics.

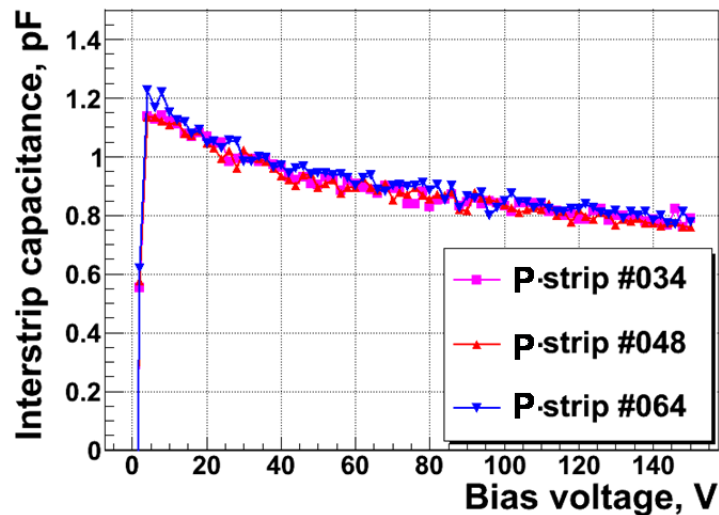


Figure 4.12: Inter-strip capacitance measurement

The parameter determining the capacitance is the geometrical shape (width and length) of the strip. The inter-strip capacitance can be lowered by reducing the width of the strips. In STS, sensors have a strip width of $18 \mu\text{m}$ and strip pitch of $58 \mu\text{m}$. The inter-strip capacitance are the main contribution to the noise level. One such measurement for the inter strip capacitance for the CBM03 sensor prototype is shown in Fig. 4.12. This strip tests is proposed to be performed only at a maximum of 10% sensors for the same reason.

4.8 Strip current

The current flowing through one strip is also an important factor that affects the performance of the silicon sensor. The strip current is defined as the current flowing through a single strip to the bulk when all other strip are either not connected or grounded. The average strip current measured in our prototype sensors is being shown in Fig. 4.13 and the effects of radiation on the strip current of the sensors is shown in Fig. 4.16. The values suggest that even at the highest radiation dose expected at CBM ($\geq 1 \times 10^{14} n_{eq}/cm^{-2}$), the average strip current remains below 2 nA/strip. This test confirms the radiation hardness of our prototype sensors.

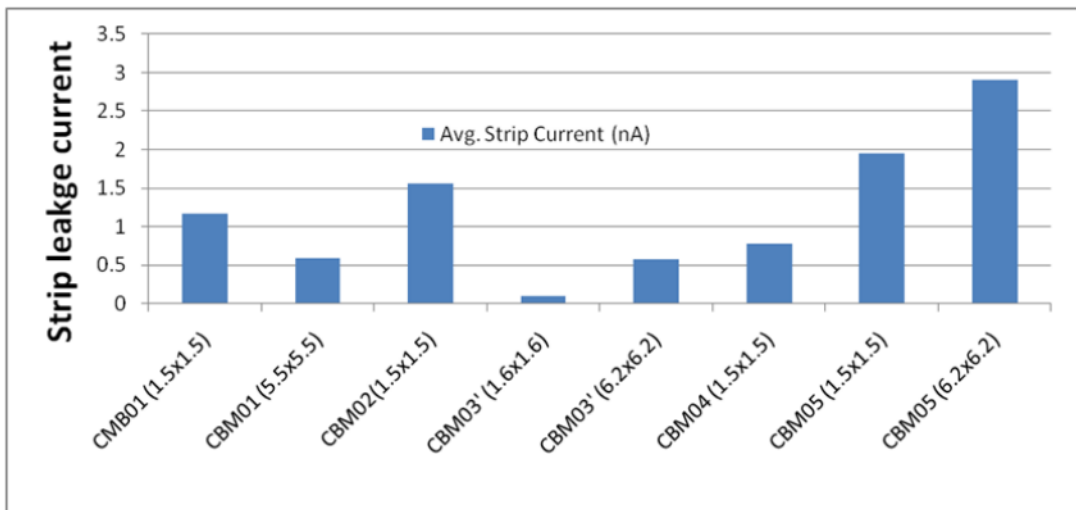


Figure 4.13: Average strip current on CBM-STS sensor prototypes of different families

4.9 Long term stability

One such test performed to derive the long-term stability is to observe the leakage current for a longer time (typically 48 hours) on a biased sensor at its intended operating voltage ¹.

¹At the CMS experiment at LHC-CERN, the typical time chosen for the long-term stability test of the silicon sensor was 2 days or 48 hours.

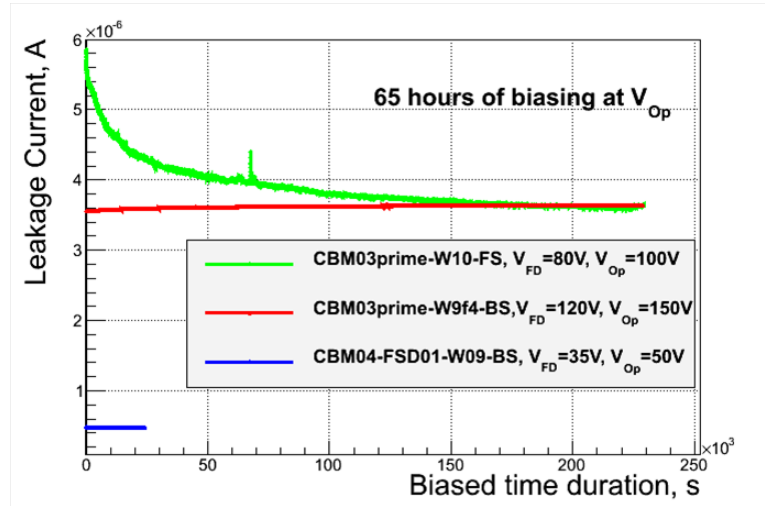


Figure 4.14: Long term stability measurement for sensors

The results from one such test performed for 60 hours are shown in Fig. 4.14. Since this is a process stability test, it is proposed to perform this test at least for 1% of the sensors per batch of a production cycle. The reason is following: the silicon sensor has to be investigated for the stability in the resistance of the bulk which is a parameter only affected by the processes involved during its production. The non uniformity observed in the long-term operation of the silicon sensors clearly indicates instability for longer operation. For the irradiated sensors, the test must be performed at sub-zero temperatures to avoid any thermal runaway and subsequent damage to the sensor.

4.10 Radiation tolerance

The sensors have to be operational in the high radiation environment. This needs to be investigated by having a test for confirming the radiation hardness of these prototype sensors. The basic post-irradiation effects are: increase in the bulk leakage current and the change in the depletion voltage due to defects formed by the irradiation. These defects heal over the time. This phenomenon of healing is called annealing.

Fig. 4.15, shows how the leakage current in our prototype silicon sensors ir-

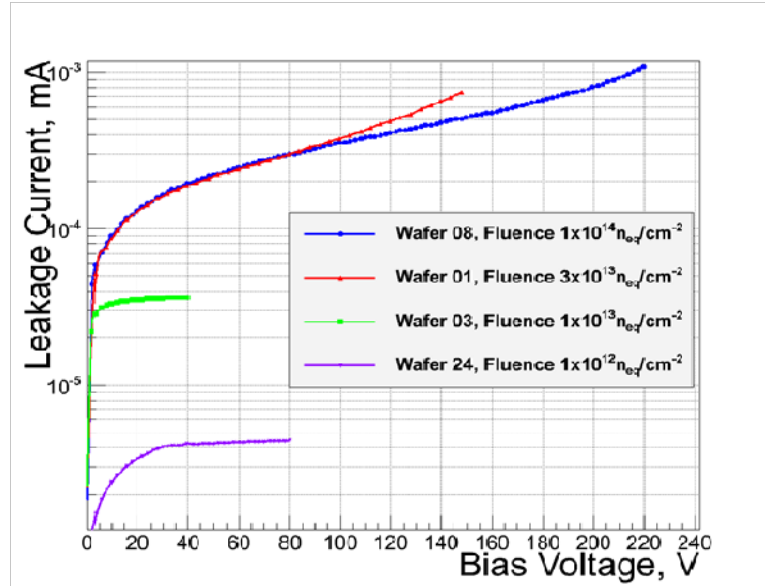


Figure 4.15: Leakage current measurement for radiation hardness

Fluence (n_eq/cm2)	Leakage Current (μ A)	Strip Current (μ A)
0.0E12	0.2	0.58
1.0E12	4.2	0.50
1.0E13	3.5	0.60
3.0E13	10.0	0.80
1.0E14	30.0	0.83

Figure 4.16: Effect of irradiation on leakage and strip current

Fluence (n_eq/cm2)	Depletion Voltage (V)	Operating Voltage (V)
0.0E12	35	55
1.0E12	30	50
1.0E13	12	32
3.0E13	80	100
1.0E14	100	120

Figure 4.17: Effect of irradiation on operating voltage

radiated with neutron at the TRIGA-III reactor in Ljubljana, Slovenia. The leakage current increases from nA for non-irradiated sensors (see fig. 4.5) to a range of μA for irradiated sensors. The change depends upon the radiation dose (represented in terms of 1 MeV neutron equivalent/ cm^{-2}), and also the change in depletion voltage which initially decreases to a minimum and later increases with increasing radiation dose is called “type inversion”. The effect of the radiation on the strip current and on the operating voltages are shown in Fig. 4.16 and 4.17. The colour code is to show increasing intensity of neutron radiation dose.

4.11 Summary of electrical characterization and QA

From the systematic characterization of the silicon micro strip sensors, important parameters and tests which are required to be performed on the sensors for its Quality Assurance has been identified and reported [47]. Systematic procedures include information and frequency of these tests to be performed. The various tests include:

1. Sensor Test: this test is proposed to be done on each and every sensor. Although the manufacturer provides the bulk characterization of the sensors with the delivery, it is recommended to perform basic tests to confirm the operational condition of the received sensors.
2. Strip Test: this test is proposed to be performed on at least 10% of the sensors. The reason for not performing strip test on all is as follows: several strip tests require manual/automated needle to probe the sensor surface, this makes it prone to possible scratches and damages caused mechanically on the sensor surface. Since, the strip tests on a few sensor is enough to predict the operational performance of the sensor, it is therefore recommended to have only 10% of the total produced sensors from a single batch to be exposed to strip tests.
3. Process stability and Irradiation test: This test is proposed to be performed on only 1% of the sensors produced per batch. The Radiation hardness,

Current and process stability test provides information about the (non-)uniformity during the production cycle, it is recommended to not to test more than 1% sensors. The process stability tests are either performed on prototype structure or they are destructive in nature. It is therefore recommended not to perform these tests on many sensors.

A more detailed version of the procedures of the passive electrical characterization is compiled as a note and can be found in Ref. [51]. The qualified sensors are sent for bonding and module assembly. It is also important to have a quality assurance performed after the assembly of the detector module. For the characterization and quality assurance of the detector modules a infra-red laser based testing system was developed and reported in the next chapter.

Chapter 5

Detector Characterization & QA using infra-red laser

5.1 Different methods of characterization

From NA11 (1978-1982) [52] to the most recent CMS experiment (2008-present) [53], silicon micro-strip sensors have played a decisive role in tracking of charged particles. Silicon detectors play a key role in particle detection, tracking efficiencies, primary or secondary vertices (coordinates) [54]. It is therefore of utmost requirement to have a systematic characterization of the sensors before they are employed to the experimental set-up. Silicon micro-strip sensors could be systematically characterized in three different ways:

1. Particle beam: Installing a set of silicon sensors are exposed to real-experimental conditions in a small scale. A beam of minimum ionizing particles (MIP) are shot on the silicon sensors (detectors) to test detection efficiency, tracking performance, operational parameters etc. (see fig. 5.1 (a))
2. Radioactive sources: Installing a small detectors set-up and collimating radioactive sources of alpha- (e.g., Americium-241) or beta- (e.g., Strontium-90) particles on the surface to study detection efficiency, charge collection, operational parameters etc. (see fig. 5.1 (b))
3. Lasers (red and infra-red): Installing a small detectors set-up and injecting

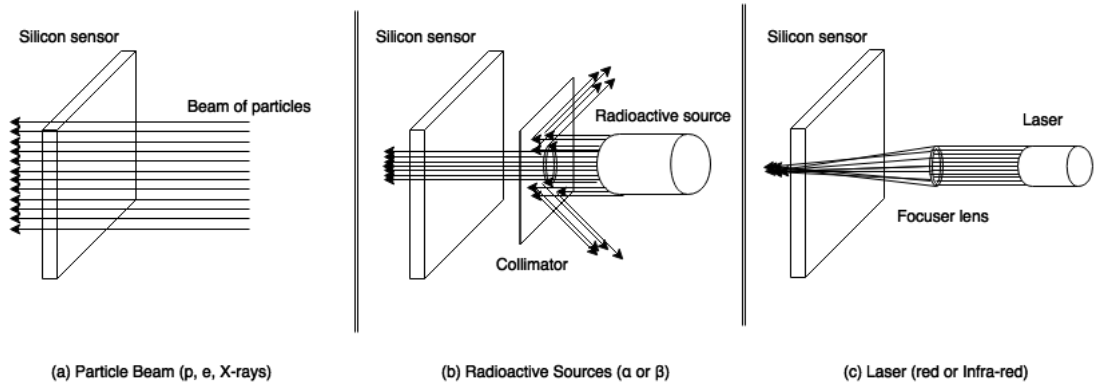


Figure 5.1: A schematic representation of three characterization methods adopted to investigate operational parameters for the silicon sensor, namely: (a) Particle beam (proton, electron, X-rays etc.), (b) Radioactive source (α or β) and (c) Laser (red or infra-red).

monochromatic beam of photon of specific wavelength (ranging from red to infra-red region) inducing charge in a very localized region (of the order of few microns) and study basic characteristics of sensor, charge division, detection, uniformity and verification of design parameters. For the investigation and characteristics of surface properties, red light (~ 980 nm) and for the bulk, infra-red light (~ 1060 nm) is utilized.(see fig. 5.1 (c))

Performance of the sensor (detector) could be characterized by investigating following parameters:

1. Charge Collection Efficiency (CCE)
2. Position resolution
3. Charge collection timing
4. Capacitive charge division
5. Hit detection efficiency
6. Cluster size
7. Noise accumulated

-
8. Signal-to-Noise ratio (S/N)
 9. Long term stability
 10. (Non-)Uniformity of the sensor response

It is interesting to know that all of these parameters or characteristics have to be investigated as a function of: (a) bias voltage, (b) front-end electronic (FEE) settings, (c) Magnetic field (if applicable), (d) radiation dose (if applicable), (e) angle of incidence, (f) ambient temperature of operation (if applicable) etc. Each of the above mentioned testing methods have both pros and cons associated with them. It must be understood that choosing a method for characterization does not mean ruling out the others. It is rather a staged or preferential approach to which methods shall serve best in the interest of understanding the sensor behaviour and its operational ability at a given stage of research and development. The list of pros and cons is been discussed below for all three methods:

1. For the particle beam tests:

- Pro: It is ultimate test for the sensors in all sense. It is an ideal method to answers most of the questions related to operation and functionality. CCE, S/N, and signal systematics could be studied with the precision of Landau distribution most probable value/mean fit. Timing could also be done using the trigger. Tracking efficiencies could also be investigated. Calibration and alignment procedures are not required more than once.
- Contra: This method is highly expensive to have as it need to relocate the experimental test set-up to a facility where desired beam could be obtained. The availability of this test is very limited. It needs tremendous amount of time to organize a particle beam test.

2. For the radioactive source tests:

- Pro: It is readily available in most of the cases and very inexpensive compared all the other options. It is create MIP-like scenario in the sensor bulk. Ideal for charge collection efficiency, hit detection efficiency and amplitude response.

-
- Contra: There is no position information available using the radioactive sources. The spectrum is quite broad. It is always required to have a good trigger for better results. Cuts in the systematics affects the results. Since position information is not available angular dependence which can be $\sim 15\%$ effect could not be precisely investigated. Cluster size and charge division are effected by the geometry of the set-up. Calibration and alignment procedures may be required on multiple occasions.

3. For the laser test:

- Pro: The installation cost is not cheap but once installed the system is readily available for the tests. It also provides the position information as you could focus the beam to a location of choice with precise knowledge. Verification of design parameters can be done with high precision. Ideal for localized studies and capacitive charge coupling investigations. Quick quality assurance could be performed on the overall response of the sensor. Bonding and mapping of the wire- or the tab-bonds to strips could be checked and identified, helpful for the tracking algorithms. Non-uniform exposure to the laser could be used to study the dynamics in the bulk of the silicon which is unique to the laser tests. Calibration procedure is required only once.
- Contra: The interaction mechanism to the sensor bulk with laser is different to that with the particles. Reproducibility depends highly on data acquisition set-up and absolute measurements are problematic. Due to different mechanism of creating e-h pairs in the bulk some of the effects are missing in the laser driven characterization procedure such as δ -electrons and the energy of the particles (dE/dx). On the other hand the measurements have additional effects to the procedure such as optical reflections both primary from the surface and the secondary from the internally from the bulk.

Analysing the pros and cons of these different methods, it is clear that although installation cost for laser based characterization is not cheap but once in-

Table 5.1: A list of parameters or characteristics of the silicon sensors which is required to be investigated and their possibility with different methods available.

Characteristics	Particle beam test	Radioactive sources test	Laser test
Charge collection efficiency (CCE)	Yes	Yes	Yes (with uncertainties)
Position resolution	Yes	No	Yes
Charge collection timing	Yes	Yes	Yes (External Trigger)
Capacitive charge division	Yes	No	Yes
Hit detection efficiency	Yes	Yes	Yes
Cluster size	Yes	Yes	Yes (Indirect)
Noise	Yes	Yes (limited with cuts)	Yes (limited to threshold)
Signal-to-Noise (S/N)	Yes	Yes	Yes (Indirect, not precise)
Amplitude response	Yes	Yes	Yes
Inter-strip capacitance	No	No	Yes (Indirect)
Coupling capacitance	No	No	Yes (Indirect)
Implant width	No	No	Yes (Metal width)
Operational voltage	Yes (Indirect)	Yes (Indirect)	Yes
Full Depletion Voltage	Yes (Indirect)	Yes (Indirect)	Yes
Broken wire-/tab-bonds	No	Yes (not precise)'	Yes
Mapping scheme	No	No	Yes
Strip current	No	No	Yes
Coupling capacitance to neighbouring strips	No	Yes (Indirect)	Yes
Non-uniformity in the bulk	No	No	Yes
Transient studies of parameters	No	No	Yes

stalled and configured, it is readily available for variety of investigations. Testing the sensors with laser has many advantages e.g, (1) beam of light with finite width is used instead of particles (as in other cases) helping in understanding charge sharing, surface effects locally and the bulk simultaneously, (2) spatial resolution of segmented silicon sensors can be evaluated better with focused localized beam of photons from laser than the test beam, (3) laser pulses ($\sim 5 - 15 \text{ ns}$) follows the trigger pulses good for pulse shape studies and (4) charge collection efficiency (CCE) measurements could be performed very accurately with some systematic uncertainties, (5) timing and delay in charge collection could be analysed alike in test beam with triggered electronics, (6) Designed parameters for the sensors could be verified easily and (7) (Non-)Uniformity of the sensor response could also be studied and analysed. A compiled list of characteristics (or parameters) associated to investigation and assurance of silicon micro-strip sensors with above mentioned methods of characterizations are summarised in the table 5.1. In the succeeding section, the laser induced charge generation in the silicon is explained (cf. section 5.3).

5.2 Interaction of light with silicon

Light is an electromagnetic wave which has wave properties but because of its wave-particle duality it behaves like a particle when entering material like semi-conductors (e.g., silicon). Both the wave and the particle properties of light should be considered when analysing its interaction with Silicon. Fig. 5.2 shows the electromagnetic spectrum divided into various categories based on frequency and wavelength [55].

In general, the beam of light approaching a semiconductor material would encounter six basic process described in fig. 5.3, such as reflection, refraction, diffraction, scattering, transmission and absorption [56]. Interaction with light provides an important experimental tool to study semiconductors. The particle associated with light, or with any electromagnetic wave is the photon. Photons incidenting on the surface of the silicon will be either reflected from the top surface, will be absorbed in the material (bulk) or, failing either of the above two processes, will be transmitted through the material. For photo-voltaic devices,

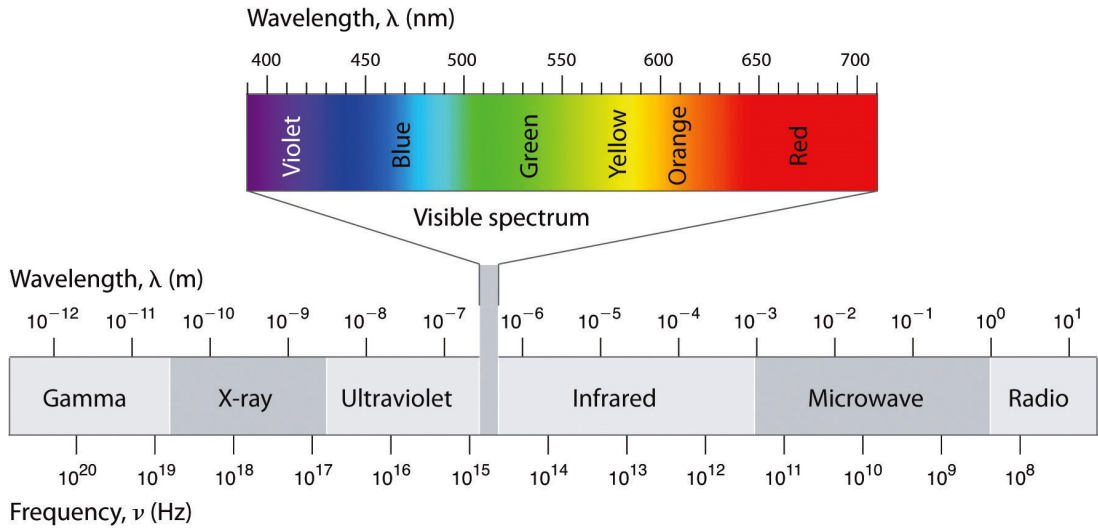


Figure 5.2: The spectrum of electromagnetic radiation, including wavelength ranges for the various colors in the visible spectrum

reflection and transmission are typically considered loss mechanisms as photons which are not absorbed do not generate power. If the photon is absorbed, it has the possibility of exciting an electron from the valence band to the conduction band. This property holds true for the analysis of the silicon sensors for tracking particles (explained in detail in section 5.4).

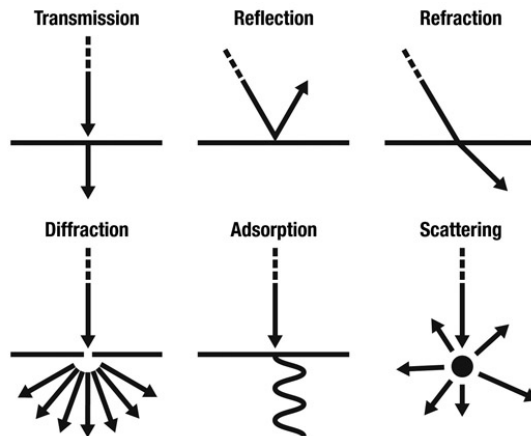


Figure 5.3: Various process during interaction of light (photons) with semiconductor materials

A key factor in determining if a photon is absorbed or transmitted is its

energy (E_{ph}). Therefore, only if the photon has enough energy, the electron will be excited into the conduction band from the valence band. The absorption of photons creates both a majority and a minority carrier. Photons falling onto a semiconductor material can be divided into three groups based on their energy compared to that of the semiconductor band gap (E_{gap}) [57]:

1. $E_{ph} < E_{gap}$: Photons with energy E_{gap} less than the band gap energy E_{gap} interact only weakly with the semiconductor, passing through it as if it were transparent (see fig. 5.4 (a)).
2. $E_{ph} = E_{gap}$: have just enough energy to create an electron hole pair and are efficiently absorbed (see fig. 5.4 (b)).
3. $E_{ph} > E_{gap}$: Photons with energy much greater than the band gap are strongly absorbed. However, the photon energy greater than the band gap is wasted as electrons quickly thermalize back down to the conduction band edges (see fig. 5.4 (c)).

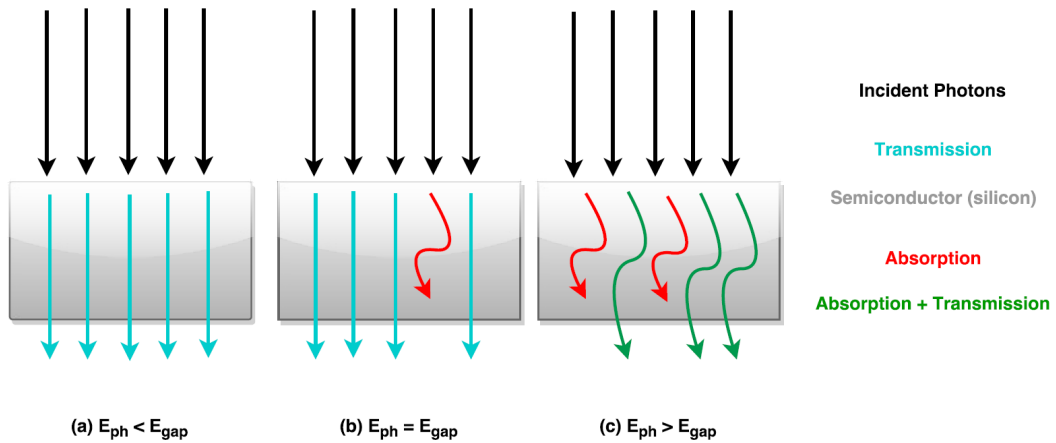


Figure 5.4: Schematic representation of the photon interaction with the semiconductor material based on the energy of the photon. The three situations are: (a) $E_{ph} < E_{gap}$, (b) $E_{ph} = E_{gap}$ and (c) $E_{ph} > E_{gap}$.

A photon can be characterized by its kinetic energy (E_{ph}) which is directly related to the wavelength of the light (λ) when the radiation is considered as a wave. The relation can be expressed as:

$$E_{ph} = \frac{hc}{\lambda} \quad (5.1)$$

where h is the Planck's constant ($6.626 \times 10^{-34} \text{ Js}$), c is the speed of light in vacuum ($3 \times 10^8 \text{ ms}^{-1}$) and λ is the wavelength of the light. If the photon energy is expressed in electron-volts ($1 \text{ eV} = 1.602 \times 10^{-19} \text{ J}$) and if the wavelength is expressed in nanometres then the formula above simplifies to:

$$E_{ph}[\text{eV}] = \frac{1240}{\lambda[\text{nm}]} \quad (5.2)$$

A large amount of photons constitutes a ray of light, this ray of light can be characterized by its parameters such as wavelength, intensity and the variation of this intensity over time. This could be understood as the amount of particles crossing an imaginary surface per unit of time. Particles interact with each other by exchanging particles or energy. A photon interacts with other particles by transferring its energy to the other atoms in the medium and thus exciting the loosely bound electrons to conduction band and thus creating a electron-hole (e-h) pair. As explained above, this exchange of energy happens if the maximum energy that the photon can bring is at least equal to the smallest quantum of energy that the other particle can accept. For a mono-crystalline Silicon lattice, this smallest quantum is 1.1 eV, referred to as the silicon band gap energy E_{gap} . As explained above, photons of energy below 1.1 eV (case: $E_{ph} < E_{gap}$) will go through the silicon without any interaction, the material is transparent [58]. This corresponds to 1125 nm according to equation 5.2.

Photons with energy above 1.1 eV (case: $E_{ph} > E_{gap}$) will not necessarily interact or be absorbed in the silicon but the probability of the interaction or absorption will depend on how much higher energy above the band gap ($E_{gap} = 1.1 \text{ eV}$) the photons comes with. There is a significant attenuation of the photon energy when light is transmitted through silicon (valid for all semiconductors) due to the probability of interaction and absorption. This probability absorption of light is proportional to the intensity (the flux of photons) for a given wavelength;

in other words, as light (beam of photons) passes through the silicon the flux of the photons is diminished by the fact that some of them are absorbed on the way through [59]. Therefore, the amount of photons arriving at a certain point in the silicon depends on the wavelength of the photons and the distance from the surface. The following equation describes mathematically the exponential decay of intensity of monochromatic (one-colour or approximately single-wavelength) light as it travels through a semiconductor (e.g., silicon):

$$F(x) = F(x_0) \exp(-\alpha(x - x_0)) \quad (5.3)$$

where $I(x)$ is the intensity at a point x [cm] below the surface of the semiconductor. $I(x_0)$ (or simply I_0) is the intensity at the surface point x_0 and α [cm^{-1}] is the absorption coefficient, which determines the penetration depth of light with certain wavelength into the semiconductor. This absorption coefficient (α) defines which percentage of the photons entering a one centimetre thick material will be absorbed [60]. By reasoning on a infinitesimal thickness of material (e.g., silicon) of thickness dx and integrating over the thickness of the material, one can deduct the Beer-Lambert law from the equation 5.3 giving the density of photons at a given depth for a given density of electrons entering the material:

$$I(x) = I_0 \cdot \exp(-\alpha \cdot dx) \quad (5.4)$$

From equation 5.4, one can define a penetration depth (d) as the thickness of the material required to absorb $1/e$ (37%) of the incoming photons (radiation). In other words, penetration depth for any wavelength of light could be defined mathematically as the thickness of the material where the intensity of the incoming photons (radiation) is reduced to $1/e$ of the total [61]. The wavelength important for our case is infra-red part of the electromagnetic spectrum shown in fig. 5.2. The reason for choosing the infra-red wavelength for the characterization of the silicon sensors (detector modules) is explained in succeeding section 5.4. By the way, pioneering work on the absorption of light in a medium has been performed by Lambert (1760) [62] and Beer (1852) [63].

$$\begin{aligned}
& \text{at } x = d \\
\Rightarrow I(x) &= \frac{1}{e} I_0 \\
\Rightarrow \frac{1}{e} I_0 &= I_0 \exp(-\alpha.d) \\
\Rightarrow d &= \frac{1}{\alpha}
\end{aligned} \tag{5.5}$$

5.3 Laser-induced charge generation

Silicon sensors for the tracking particle detectors are basically a pn-junction diode operated in the reverse bias mode. Since the bulk of the material in the sensor is either p- or n-type (e.g., n-type in this case), we can assume the sensors to be of one type of semiconductor for the bulk processes and analysis. Photons that are absorbed by bulk silicon bring energy to the nearby atoms they collide with, this energy is therefore used to let one or more electrons escape from their energy band (valence band -to- conduction band). These electrons become free and can be part of a conduction process (or in other words, reach to the conduction band). The excess energy heats up the crystal or activates phonon states. The electron hole left behind in the valence band will behave as a heavy positively charged particle. These freed electrons and holes increases in number depending on the intensity and energy of the photons above the band gap energy (E_{gap}). When the light (of any wavelength) penetrates the bulk silicon (or diode in this case), the diode reacts as a photo-diode.

The electron-hole (e-h) pairs generated outside the diode junction can also diffuse to the junction and participate in the detection mechanism. Since the diode is a junction of the two semiconductor materials differently doped, the junction of these two differently doped material creates a depletion region which is virtually free of mobile charges (mobile charges here refers to the charges which could help in conduction process). Even without applied bias (applied potential difference on the diode), the negative charges drift to the p-side and the positive charges drift to the n-side of the diode due to the so called built-in potential created at the junction. This potential developed is also called junction potential.

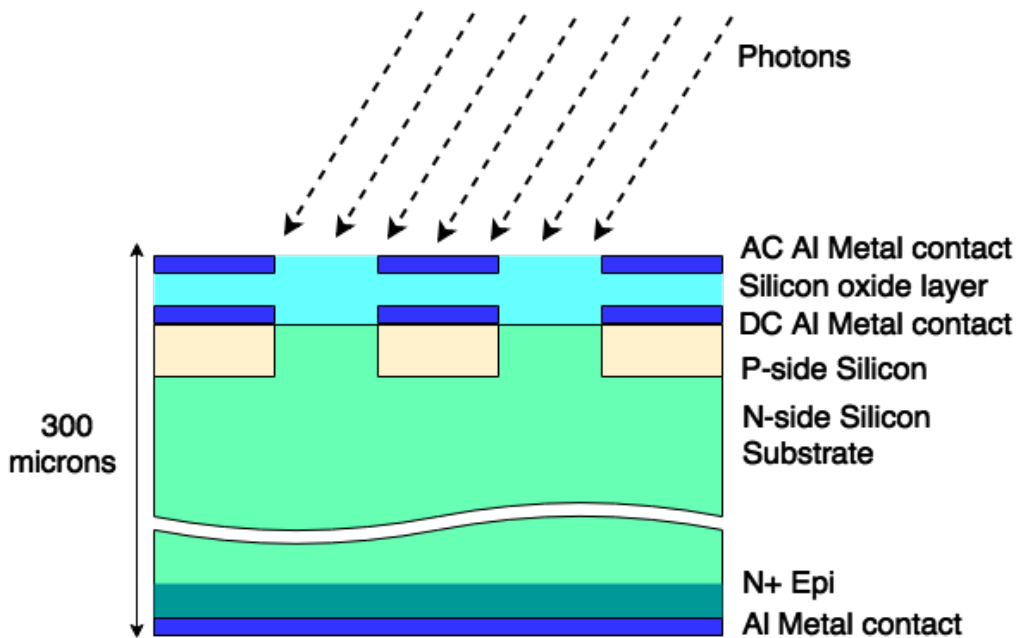


Figure 5.5: A schematic diagram representing a basic micro-strip silicon sensor structure. The sensor is of p-on-n type.

This flow of charges is a current and could possibly be measured by an electronic circuit. When the diode is biased to non-zero potential the junction potential increases gradually depleting the junction area of the majority carriers. When the diode is illuminated with the photons of certain wavelength (light), the total current is the sum of the photo-current inside junction, due to the carriers that have been drifted to the junction and the leakage current which is function of the temperature. Unfortunately the carriers do not last long. When an electron meets a hole they may annihilate each other, this process is called recombination. Recombination in silicon is an indirect process and the possibility for recycling the photon is not permitted from the point of view of quantum efficiency. This recombination process occurs on both N and P side of the diode but not in the depletion region (carrier free region). Other process which may contribute to recombination is the surface effects due to imperfect manufacturing, or with oxidised silicon on the surface etc. The carrier will need more time to reach junction and the probability of recombination increases with the distance of the carrier from the junction. The net contribution of the e-h pairs decreases when

the distance to junction increases. This depletion region is ideal for the detection and characterization of silicon sensors [64].

In order to have no more sources of e-h pairs in the bulk silicon substrate, the silicon diode (sensor) is biased with a small voltage. Fig. 5.5, shows a schematic representation of a basic micro-strip sensor with p-type implants on n-type substrate. The sensor has p-type (light yellow) implant in n-type substrate (light green) with access to implant via DC (blue) and bulk via AC metal contact (blue). The silicon oxide (light blue) uses a passive material between AC and DC pad providing a coupling capacitance to the each metal electrode (strip). The above fig. 5.5 has p-type implant which implies the depth of p-side is smaller in comparison to the n-side. The junction area (depletion region) increases with increasing external bias (potential) and saturates at the extreme of p-type implant sooner than the n-side. Therefore the p-side of the sensor remains depleted of the majority carrier while the n-side depletion region grows with increasing potential on the sensor and slowly reaches to the saturation. The full depletion of the bulk of the sensor is identified by saturation observed in the leakage current. The sensor now is in depleted mode, the voltage at which the sensor becomes free of majority carriers is termed as *depletion voltage* (V_{dep}). The leakage current of sensor increases with increasing bias potential until the depletion voltage is reached. Mostly, silicon sensors are operated at a higher voltage than the depletion voltage. It is termed as *operating voltage* (V_{op}) which is approximately 1.5 to 2 times the V_{dep} .

The silicon behaves differently to different wavelengths. This is due to the direct relation between wavelength and energy associated with each photon (see equation. 5.2). It is clear that for certain wavelengths (below the band gap energy, < 1.1 eV) the silicon shall remain transparent. Photons of these wavelengths will not be interacting with the silicon thus no current will be observed in the measuring circuit. While for photons with energy equal or higher than the band gap (≥ 1.1 eV) will be interacting with the bulk and thus will be absorbed partially or fully depending on their total energy. These photons will interact with the bulk and knock out electrons from valance to conduction band thus creating e-h pairs which can be detected or measured, some are absorbed partially and transmitted out of the bulk similar to a particle beam. This phenomenon

is well suited for characterizing the silicon sensors in the prototyping and the series production phase to analyse fundamental operation, manufacturing process, defects and so on. The reason to choose infra-red light for the characterization is explained and discussed in the next section.

5.4 Choice of wavelength for characterization

The absorption coefficient of a wavelength in a medium determines how far into a material light of a particular wavelength can penetrate before it is absorbed. In a material with a low absorption coefficient, light is only poorly absorbed, and if the material is thin enough, it will appear transparent to that wavelength. The absorption coefficient depends on the material and also on the wavelength of light which is being absorbed. For the purpose of the detector characterization and quality assurance we need to select a wavelength of light. The wavelength of light (λ) must fulfil following criteria making it suitable for the purpose of characterization:

1. $E_{ph} > E_{gap} \Rightarrow E_{ph} > 1.1 \text{ eV}$: The wavelength of the light must have energy higher than the band gap of the semiconductor material (here silicon) used for the sensors.
2. $d_{ph} > d_{Si} \Rightarrow d_{ph} > 300 \text{ }\mu\text{m}$: Penetration depth for the wavelength of light in the silicon (d_{ph}) must be larger with respect to the thickness of the bulk silicon (d_{Si}). Implying that part of the energy is absorbed and part of it is transmitted.
3. In order to study the bulk properties of the silicon sensor. The wavelength selected must be able to induce charges equivalent to minimum ionization particles (MIP). This is required as to mimic or simulate particle beam like scenario for the investigation and characteristics of the bulk silicon.

Infra-red light comes out to be the suitable wavelength for the purpose of characterization of the silicon sensors. The wavelength chosen is 1060 nm. From the equation. 5.2, infra-red light has energy greater than band gap of silicon. Fig. 5.6

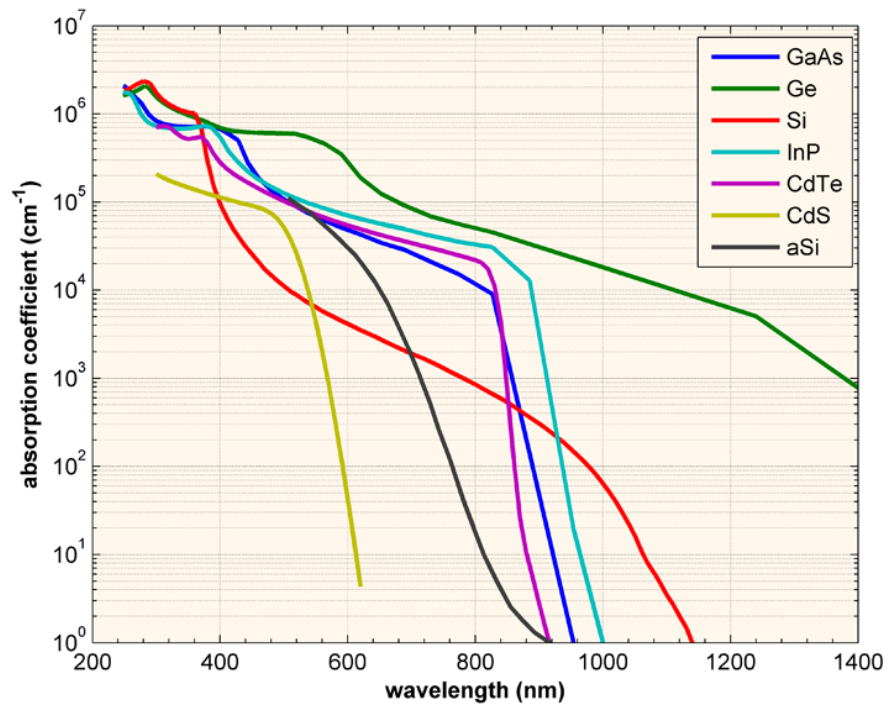


Figure 5.6: The absorption coefficient, in a variety of semiconductor materials at 300 K as a function of the vacuum wavelength of light. Silicon shown in red.

shows dependence of absorption coefficient (α, cm^{-1}) for various semiconductor materials (silicon in red) and the wavelength of light (λ, nm) from range 200 nm to 1400 nm of the electromagnetic spectrum. It suggests that the absorption (penetration) depth, d for light in silicon is $\sim 450 \mu m$ for the infra-red wavelength ($\lambda = 1060 nm$). Silicon sensors are photo-sensitive and in order to be sure about the sources of the induced current in the sensor, the measurement are performed in the light tight enclosure. The infra-red light lies in the non-visible part of electromagnetic spectrum (see fig. 5.2), making infra-red light highly reliable for the characterization and investigation as external sources (light sources) could be singled out in the light tight enclosure during every measurement. In the following section a comparison of the different methods of characterization procedures for silicon based micro-strip sensors (detectors) are discussed.

5.5 Laser Test System of the STS

From the above discussion, it is evident that the infra-red laser is a powerful tool to inspect and characterize the silicon sensors. This is one of the quality assurance techniques which could be used to characterize and understand the sensor response, integrity and charge sharing with in the inter-strip region [65]. Infra-red laser based characterization and investigation technique is not new and has been employed by many experimental and research groups such as, D-Zero - FNAL, USA (1993) [66], RHIC-BNL, USA (1995) [67], KEK, Japan (1996) [68], HERA-B, DESY Germany (1999) [65], CERN-PS, Switzerland (2003) [69], INFN, Italy (2006) [70], RD-50, Czech Republic (2006) [71], ATLAS - CERN, Switzerland (2007) [72], Charles University, Czech Republic (2007) [73], ALICE - CERN, Switzerland (2008) [74] etc. The Laser Test System (LTS) of the STS is unique and has to be made operational with challenging constraints. The challenges are as follows: (a) to characterize double-sided silicon sensors unlike in other experiments, (b) investigate large area of silicon sensors and modules, (c) account for smaller pitch to width ratio, (d) account for multiple reflection from the electrodes of the other side, (e) to operate with low threshold for noise reduction with naked detector and read-out cables. In other words, exposed to large amount of electro-magnetic radiation from front-end electronics of the set up.

A schematic representation of the laser induced charge generation in the silicon is depicted in fig. 5.7. In the process of inducing charge in to the silicon, the laser beam is guided with an optical fibre, which is attached to a focuser to inject charge (infra-red photons) into the sensor volume. The incident beam of focused photons arrive on the surface and are partially reflected and partly transmitted. The focused beam has a Gaussian-profile with a sigma of 12-15 μm depending on the working distance [75]. The photons interact with the bulk silicon and create e-h pairs. Infra-red photons of wavelength 1060 nm have a penetration depth of around 450 μm [64]. The prototype sensor from CBM-STs are only 300 μm thick so for the infra-red photons it will be transparent. In other words, the photons injected into the sensor volume will deposit energy and create electron-hole pairs and pass through, similar to in-beam particles. Since, it is needed to inject charge (q) which can mimic (or rather, simulate) the energy deposition similar to a minimum ionization particle (MIP) [76]. The thickness of the silicon sensor are 300 μm thick and the 1 MIP will deposit ≈ 22.4 kilo electrons [77]. From a detailed calibration of the n-XYTER [78] prototype front-end ASIC ¹ it has been derived that the 22.4 kilo electrons is equivalent to 176 ± 6 ADC units for our sensors [79].

The Laser Test System (LTS) of the STS is composed of 7 constituent blocks namely, (a) infra-red laser, (b) detector module, (c) front-end electronics, (d) step motor, (e) power supplies, (f) data acquisition and (g) device controls. A schematic representation of components of the laser set-up is shown in fig. 5.8.

5.5.1 Infra-red laser

A well customized infra-red pulsed laser operable in the range of 5-15 ns of pulse duration, wavelength of 1060 nm with possibility to operate in both internal and external trigger pulser is used from Sacher Lasertechnik [80] in this project (Technical Model No. TEC045-CAT). For the results shown in the following the laser was operated in pulsed mode with 10 ns pulses and a frequency of 38 kHz. The laser beam delivery system utilizes a optical fibre (length = 1 m) and a

¹An application-specific integrated circuit (ASIC), is an integrated circuit (IC) customized for a particular use, rather than intended for general-purpose.

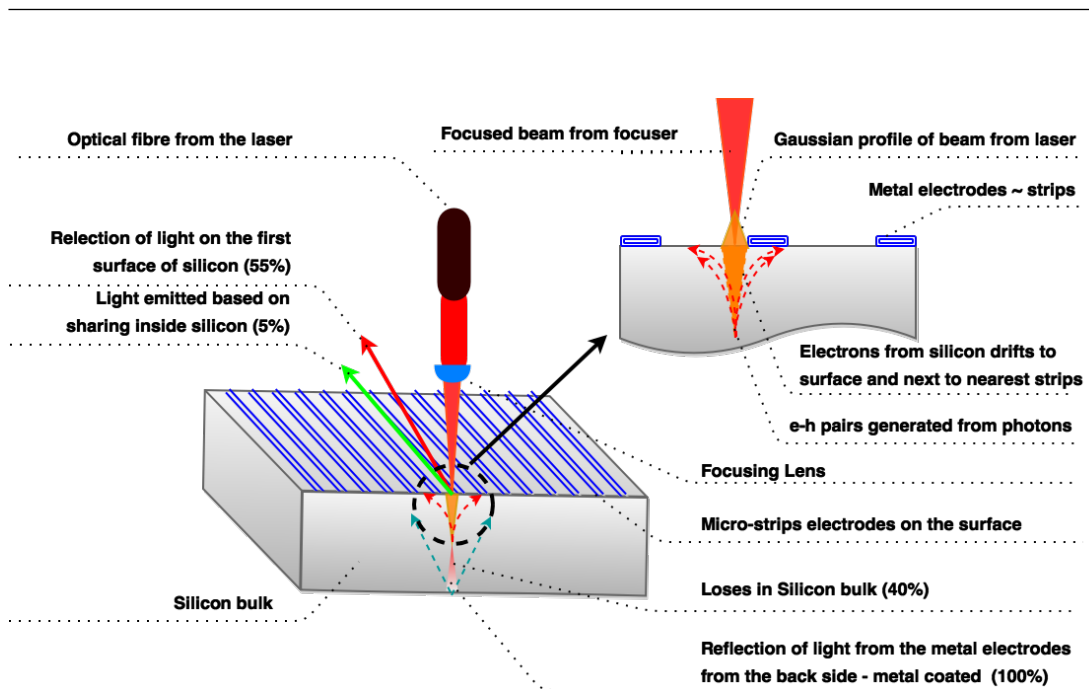


Figure 5.7: Schematics representation of the laser induced charge injection in the silicon micro-strip sensor.

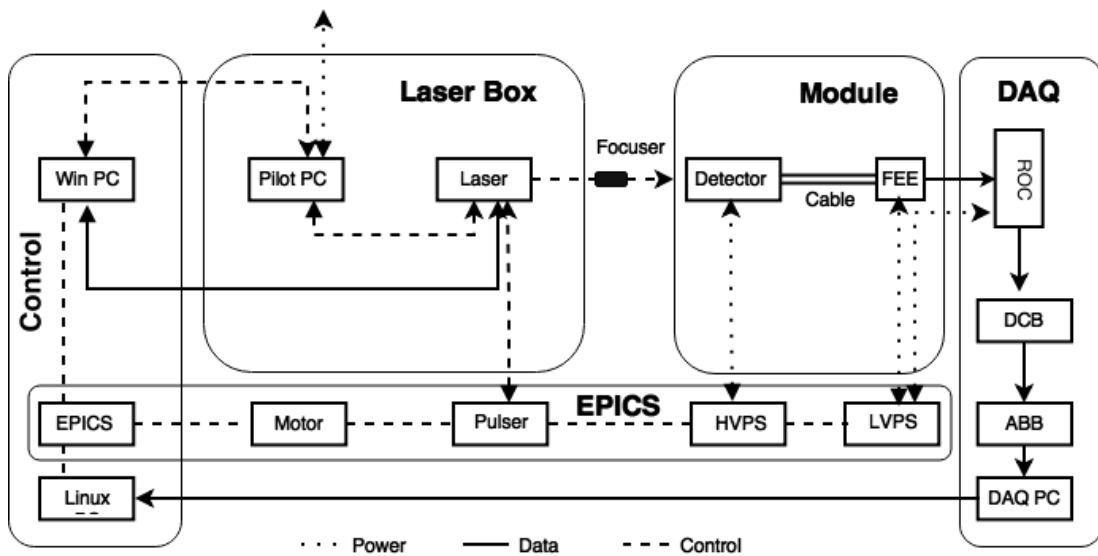


Figure 5.8: A schematic view to the connection of various components in the laser test set-up. It comprises of 5 block (a) Control, (b) Laser, (c) Detector module (sensor, cable and front-end electronics), (d) EPICS control sequencer and communicating all control devices (e) DAQ - Data Acquisition from read-out-control.

optical-lens focuser with a spot size (σ) around $12 \pm 2 \mu\text{m}$. (see section 5.7.3). The TEC045-CAT system is a diode laser system designed for pulsed operation of high power diode lasers but it is customised to suit the needs of the laser test set-up for the silicon sensors. The operating mean peak power is $\sim 3 \text{ mW}$. The pulse width could be tunable with a step of 2.5 ns from 5 -15 ns. The repetition rates can be varied from 16 kHz up to 67 kHz. The operational parameters can be pre-set via a RS-232 connector from any laptop/computer. An Pilot-OEM software is controlling the parameters which serves as a link between the laser diode and the controlling computer [81]. The laser spot has to be focused on a very localized region in the inter-strip gap. It is required to have a beam delivery system from the laser head to the sensor. This is achieved by the optical fibre which is connected using the standard plug-in type ST connector and mounts a optical lens to focus the beam (called Focuser) to the sensor surface. The specification for both beam delivery system (optical fibre) and the beam focuser (lens system) is enlisted in table 5.3.

Table 5.2: Specifications of the customised infra-red laser used in the set-up.

Feature description	Specification values
Wavelength	1060 nm (Pulsed and CW)
Operation mode	Single mode
Peak output power	<3 mW
Beam divergence	<5 mrad
Pulse length	5 ns - 15 ns
Repetition rate	16 kHz - 67 kHz
Trigger	Internal and External
Computer control	RS 232 connector
Power supply	9 VDC
Dimensions	Length: 76 mm, Diameter: 38 mm
Manufacturer	Sacher LaserTechnik GmbH, Marburg

5.5.2 Detector modules

The STS prototype 2013 is being built to study the system performance of the STS building block, the “ module ”. The detector module is smallest non-repairable

Table 5.3: List of specifications for the beam delivery system (optical fibre) and the beam focuser (lens system) in the laser test set-up.

Description	Specification
Beam delivery system - Optical fibre	
Beam delivery	Optical Fibre
Length	1.5 m
Mode of operation	Monomode
Bandwidth	600 nm - 1200 nm
Core diameter	6 microns
Cladding diameter	125 microns
Type	Plug-in type
Coupler type	ST connector
Coupling efficiency	60 %
Beam coupler	Collimator lens
Provider	Sacher LaserTechnik GmbH
Beam focuser	
Lens type	Single lens
spot size	Minimum 12 microns
Working distance	10 mm
Provider	AMS Technologies

assembled unit in the silicon tracker. It is comprising of a silicon micro strip sensor, a ultra thin low mass read-out cable and a front-end electronics. Fig. 5.9 shows a schematic and a prototype detector module placed adjacent to each other. In assemblies of the most recent prototype micro-strip sensor, read-out cables optimized for smallest possible capacitive load to the read-out electronics, and read-out with the prototype ASIC (n-XYTER) for the STS-project ¹, the full read-out chain is realized and made operational in laser test set-up discussed in succeeding sections.

Four types of modules will be built, differing in the number of sensors commonly read-out and the location of read-out strips on the sensor:

1. **M1**: One single-sensor module with the central sensor area read out through 128 channels on either side.

¹A Dedicated ASIC STS-XYTER for the STS is in development now.

-
2. **M2:** One single-sensor module with a corner region read out by 128 channels on either side.
 3. **M3:** One two-sensor module with daisy-chained sensors allowing to read out the corner region of the bottom sensor with 128 channels on either side.
 4. **M4:** One two-sensor module with daisy-chained sensors allowing to read out the central region of the bottom sensor with 128 channels on either side.

The objects with the numbered contacts (as coded on the silicon sensor itself) to which the read-pout cables are to be attached to. Fig. 5.10 illustrates the different detector modules (without the attached FEE board). A closer look to the tab-bonding ¹ between the sensor strips and the aluminium traces on the read-out cables is illustrated in fig. 5.11. The scheme of read-out and region of overlapping both sides strips for characterization of the silicon sensors is explained in a schematic diagram in fig. 5.12 [82]. The characterization procedures were performed for both long strips and short strips with single sensor module and double sensor daisy-chained sensor as well.

5.5.3 Front-end electronics and power supplies

The STS project is using a dedicated read-out controller (ROC) [34], and prototype ASIC - nXYTER [83] which is in development for FAIR's data acquisition [84]. The sensor is connected to front-end ASIC by ultra-thin read-out cable. This ASIC is then connected to ROC for transfer, stream and write the data on to the disc via optical links. The prototype sensors is reversed biased with CAEN [85] high voltage power supplies. Since all front-end electronics are required to be floating we use Hameg [86] low voltage powers supplies. The motor is also powered by the Hameg low voltage power supplies. The specification for both low voltage and high voltage power supplies are enlisted in the table 5.4.

¹Tape-automated bonding (TAB) is a process that places bare integrated circuits onto a printed circuit board (PCB) by attaching them to fine conductors in a poly-amide or poly-amide film, thus providing a means to directly connect to external circuits.

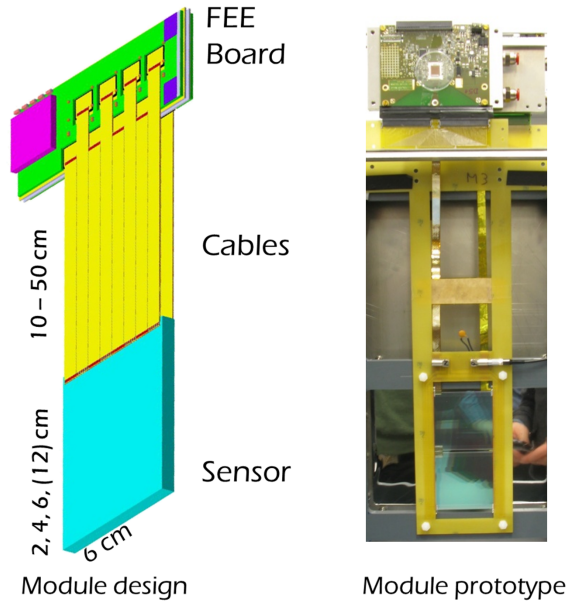


Figure 5.9: Schematic of the detector module and latest prototype placed adjacent

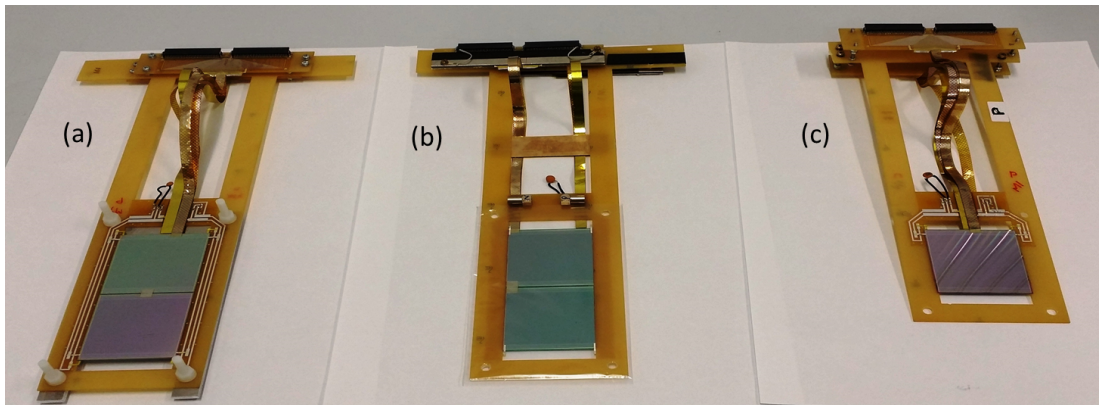


Figure 5.10: Prototype detector modules prepared with different length of ultra-thin low mass read-out cables. All detector modules are equipped with CBM05 prototype sensors which is double sided sensor of size $6.2 \text{ cm} \times 6.2 \text{ cm}$. (a) Detector module (M4) with 2 daisy-chained sensors read-out with 30 cm cable on the long strips (centre) (b) Detector module (M3) with 2 daisy-chained sensors read-out with 30 cm cable on the short strips (corner) (c) Detector module (M1) with 1 sensor read-out with 20 cm cable on long strips (centre).

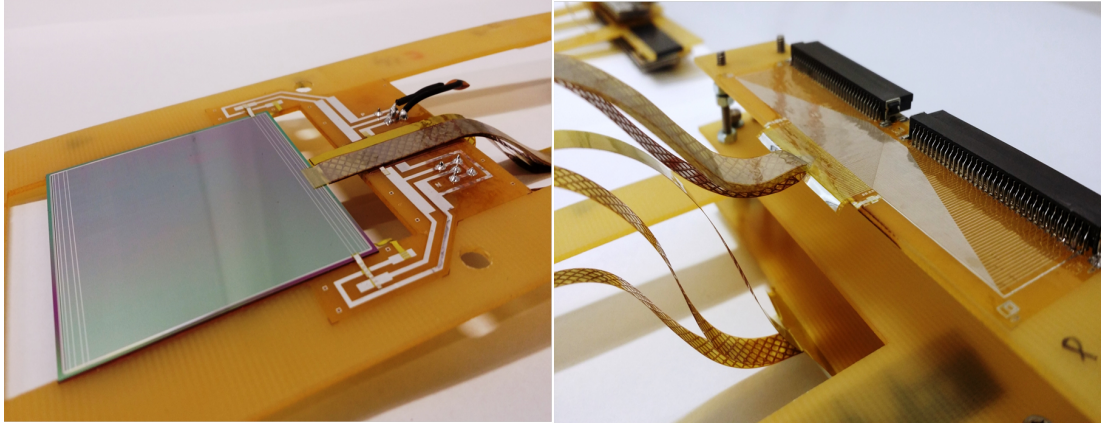


Figure 5.11: A closer look to the detector module. (a) (on the left): sensor surface - edges, strips connected to aluminium traces on read-out cables via tab-bonding and (b) (on the right): the connection to FEE board via the ERNI connectors.

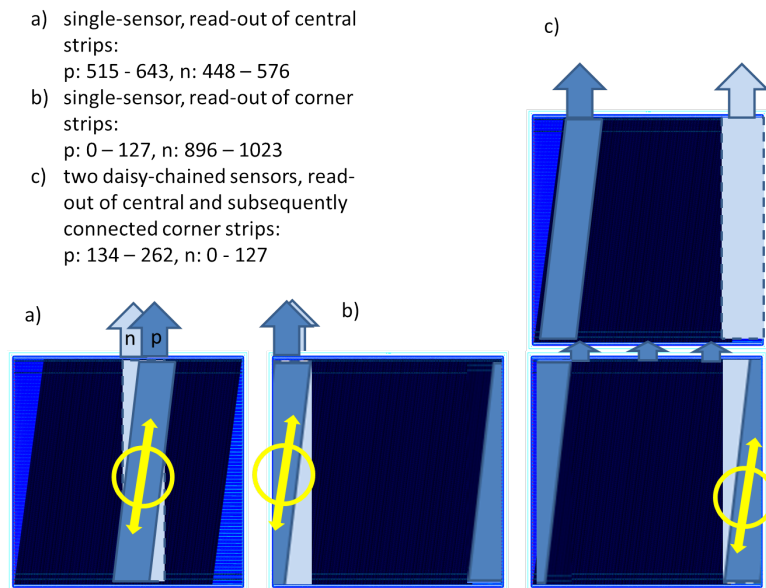


Figure 5.12: Illustration of the read-out area and the channel numbers for the connection to the read-out cable for the three prototype modules 2013. The sensor areas with two-coordinate readout that can be explored in test experiments are indicated in yellow colour. (a) Module - M1 (b) Module - M2 (c) Module - M4 (Module - M3 is not shown in the schematic.)

Table 5.4: Description of the specification of the low voltage and high voltage power supply units in the laser test set-up

Description	Specification
CAEN NDT1470	
Used for	High Voltage power supply
Type	NIM Module
Channels	4 channels in 2U NIM module
Voltage range	220 V/110 V AC plug for desktop operation
Output range	8 kV / 3mA output ranges
Max. output power	9 W (<3 kV output) and 8 W (>3 kV output)
Polarity	Channels with individually selectable positive or negative polarity
Connectors	SHV coaxial output
Remote connection	via USB or Ethernet
Grounding	Common floating
HAMEG HMP 4040	
Used for	Low Voltage power supply
Type	Programmable power supply
Channels	4 channels
Output Voltage range	per channel: 0 V - 32 V
Output current range	per channel: 0 A - 10 A
Max. Output power	160 W
Polarity	Positive
Remote connection	RS 232 and Ethernet

5.5.4 Step motor and EPICS control

The x-y step motor with a step size of $1 \mu\text{m}$ from Faulhaber [87] is used in the set-up for the scanning over the sensor surface. The motor is configured such that the total area of sensor could be scanned with customisable speed and steps. The z-axis is manually controlled for calibration of focuser over the sensor surface (see sec. 5.6). The step motor is controlled using the EPICS based control software [88]. Both x-y arms are equipped with position sensors which are magnetic and are controlled using EPICS sequencer programs with Control System Studio [89] as operator interface (OPI). The OPI is equipped with functionality to control motors separately (if needed). The pitch for the step motor can go as low as $0.33 \mu\text{m}/\text{step}$. While taking into account the backlash error in the mechanical movement of the step motor it was chosen to have a step size of $1 \mu\text{m}$ for the measurement scan. A snapshot of the Operator Interface based on Control System Studios is depicted in fig. 5.13.

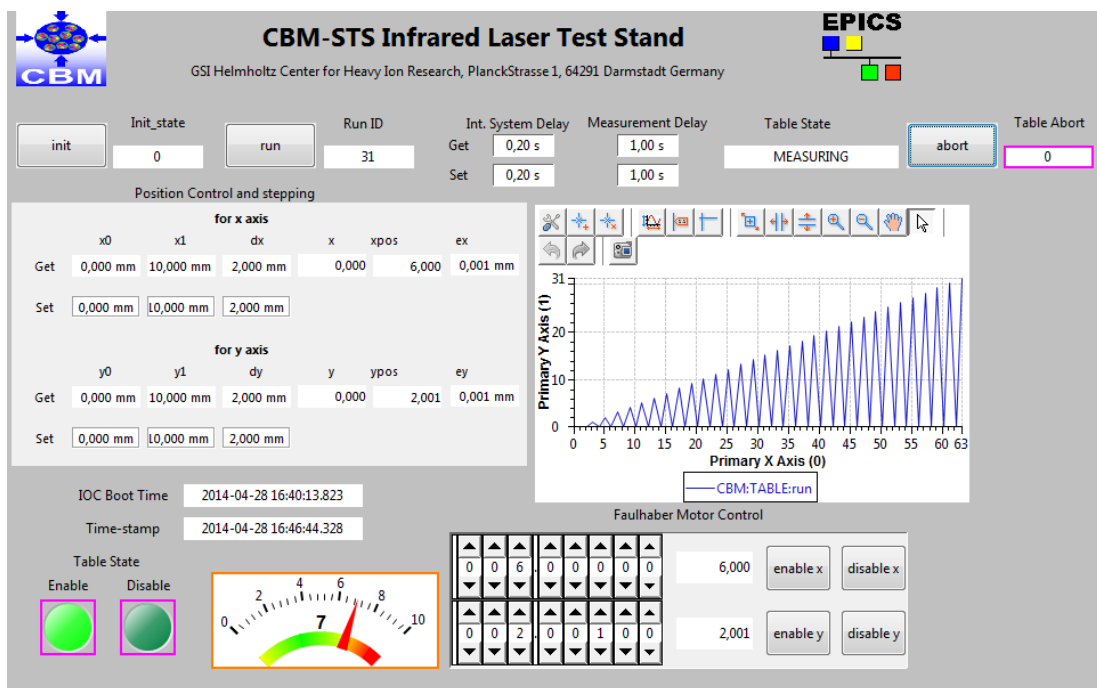


Figure 5.13: A snapshot of the operator interface (OPI) based on Control System Studio tools for the EPICS sequencer in the laser test set-up.

5.5.5 Data acquisition and analysis

Data acquisition is performed using the Data Acquisition Backbone Core (DABC) [90] framework and Go4 Analysis software [91] is used for on-line object analysis. The optical links are used for data transmission from the read-out controller boards (ROC) to the control PC. The system data synchronization is better with the optical links compared to Ethernet. The scheme of the connection in the laser test set-up is shown in fig. 5.8. The block diagram shows five main components of the laser test set-up namely, (a) Control - which includes computer/user interface programs to control laser, motor and start acquiring data when the system is ready, (b) Laser - which includes laser pilot pc, laser head and the beam delivery fibre optics, (c) Detector module which is plug-in-plug-out type includes the micro-strip sensor, ultra thin low mass read-out cable and the front-end electronics, (d) EPICS control sequencer and communicating all control devices including the power supply, motor, pulse generator (e) DAQ - Data Acquisition from read-out-control.

5.6 Calibration of laser test stand

A set of calibration procedures is to be performed before we inject charge and simulate the in-beam scenario using the infra-red laser. The procedure includes determination of optimum laser current (I_{laser}) for the sensor response and optimum distance of focuser over the sensor surface (z). Figure. 5.14, shows a systematic calibration method. This is performed by study of response from the sensor (number of activated strips) with different laser currents at different positions above the sensor surface. Thus, the minimum position of z on the curve provides the focused position ($z_{focused}$). Figure. 5.15, shows the laser current (I_{laser}) is tuned at a optimum focused position to collect signal from single strip. It is important to note that the calibrated laser position is subject to change if the detector module is moved or the changed. For every different module studied we have to start a calibration procedure to insure that the spot size is minimum and the working distance is optimal too. As soon as the calibration procedure is performed the system (detector module and the laser) is ready for

the characterization.

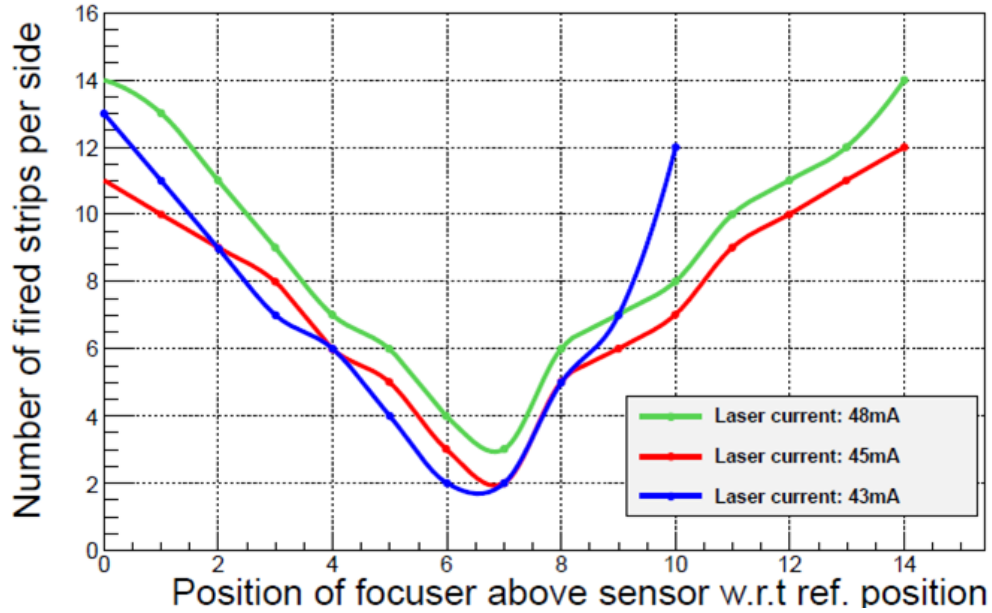


Figure 5.14: Calibration: Optimum distance for focuser and optimum laser current

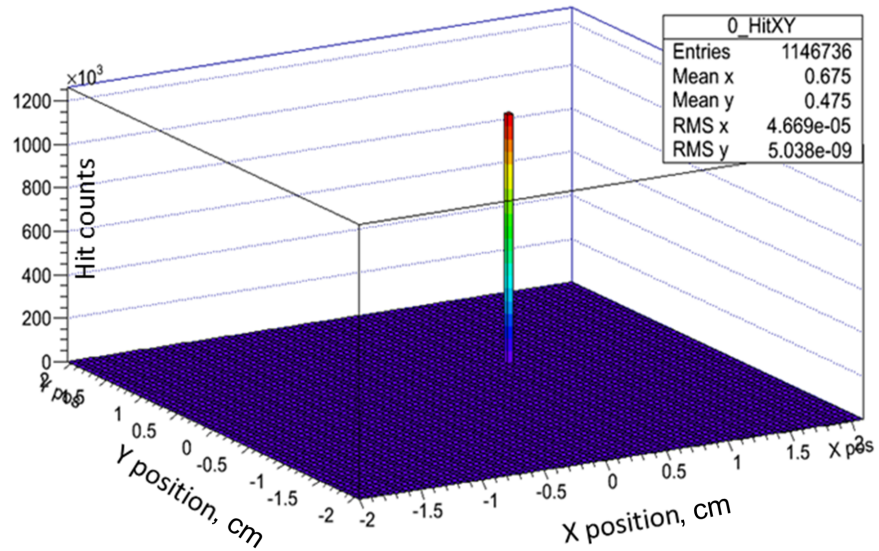


Figure 5.15: 3D lego plot showing the hit counts on focused position after calibration

5.7 Characterization results

The characterization and investigation of silicon micro-strip sensors which is possible using the pulsed infra-red laser is discussed in the sec. 5.1 and listed in the comparison to other methods in table 5.1. With the provided infra-red laser from Sacher, it is possible to do measurements in two possible ways, such as:

1. **Internal triggered mode** (using signal from internal pulse generator).
 - Laser current: 40 mA (for measurement scan and higher currents for calibration of focuser).
 - Frequency: 16 kHz (possible to go down to 10 kHz to 100 kHz).
 - Pulses: 10 ns (options Internal pulse generator : 5 ns, 7.5 ns, 10 ns & 15 ns).
2. **External triggered mode** (using TTL signal from pulse generator).
 - Amplitude: 3 V (in the range 2.2 V - 5 V).
 - Frequency: 10 kHz (or as low as 100 Hz for other cases such as MVD sensors with low rate capability read-out.).
 - Pulses: 10 ns (or as low as 1 μ s for other cases such as MVD sensors with low rate capability read-out.).

As listed above, external trigger mode is extremely useful in the cases when the data rate for the read-out ASIC (chip) is too high in internal trigger. The external trigger system was utilized for the spot size measurement with the CBM-Micro-Vertex-Detectors. Fig. 5.16 shows a photograph of the laser set-up stationed inside the light-tight box. It includes the laser head and beam delivery system (optical fibre) which is taking the laser beam to the focuser. The beam from the focuser is injected on to the detector module. The detector module is lying centrally below the laser focuser which is free to move in direction of choice (with some limitation for security reasons). Optical links from the read-out controller are acquiring the data which is controlled by the operator interface (see the scheme in fig. 5.8).

The major investigation or characterization reported are:

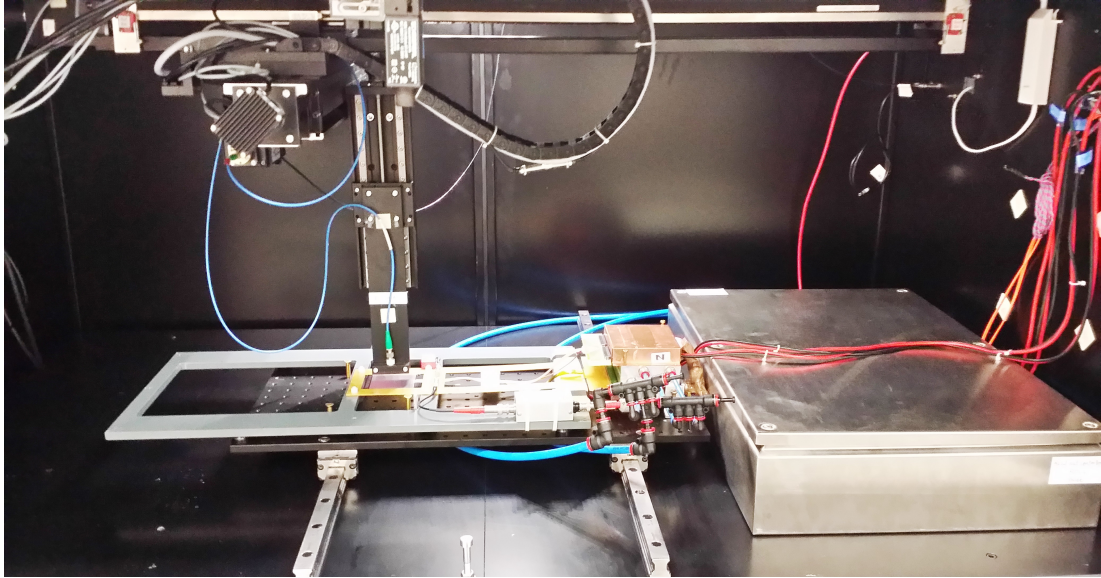


Figure 5.16: Photograph of the laser test set-up inside the enclosed light-tight box.

1. **Sensor integrity and amplitude response:** This provides a quick check on many significant parameters after the sensor is tab-bonded and connected to a FEE.
2. **Charge sharing and the η function:** This provides microscopic health of the detector giving access to locally study the properties of the detector module and its operational ability.
3. **Spot-size measurement and verification of designed parameters:** This measurement provides a mechanism to study all measurements in detail. It provides access to the geometric design parameters and help verify them in a non-invasive manner.

5.7.1 Sensor integrity and response

The laser beam after the calibration is injected using the focuser on the n-side and both sides are read-out simultaneously. Figure. 5.17 and figure. 5.18, shows plots with fraction of amplitude of charge collected at each individual strip on p- and n-side respectively. The amplitudes plotted are obtained at a defined

position on the sensor surface when laser moves from left to right with equivalent steps of $2 \mu\text{m}$ each. The observed response to the charge injection for both p- and n-sides proves uniformity and integrity of strips on the sensor. The charge is also collected by next nearest neighbour but its contribution to total charge is minimal. The dip (or, local minima) observed at the centre of the n-strip is explained by the metal reflection and field distortion. This phenomenon is used to extract or determine the spot size (σ) for detailed analysis. (see Section 5.7.3)

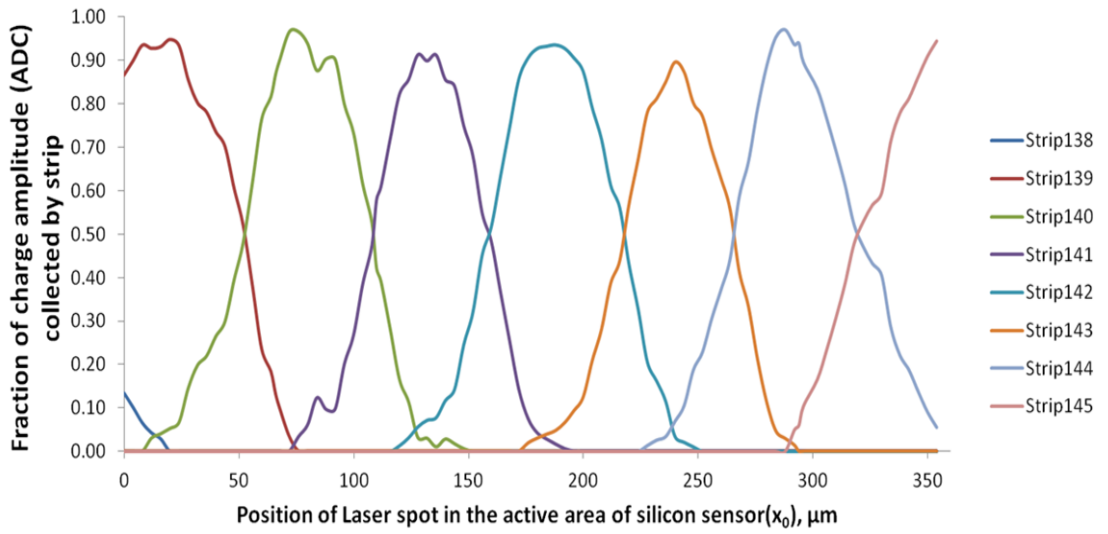


Figure 5.17: Fractional amplitude of charge amplitude collected at p-side

5.7.2 Charge sharing and η function

The η function is used to explain the charge division or sharing with in the inter-strip region of the silicon micro-strip sensors. The ratio amplitude of the charge collected at a position (x) to the strip on the right (A_R) to the total amplitude of the charge collected by both left (A_L) and the right strip (A_R) is called the η function [92]. Mathematically,

$$\eta(x) = A_R / (A_L + A_R) \quad (5.6)$$

or,

$$\eta(x) = A_L / (A_L + A_R) \quad (5.7)$$

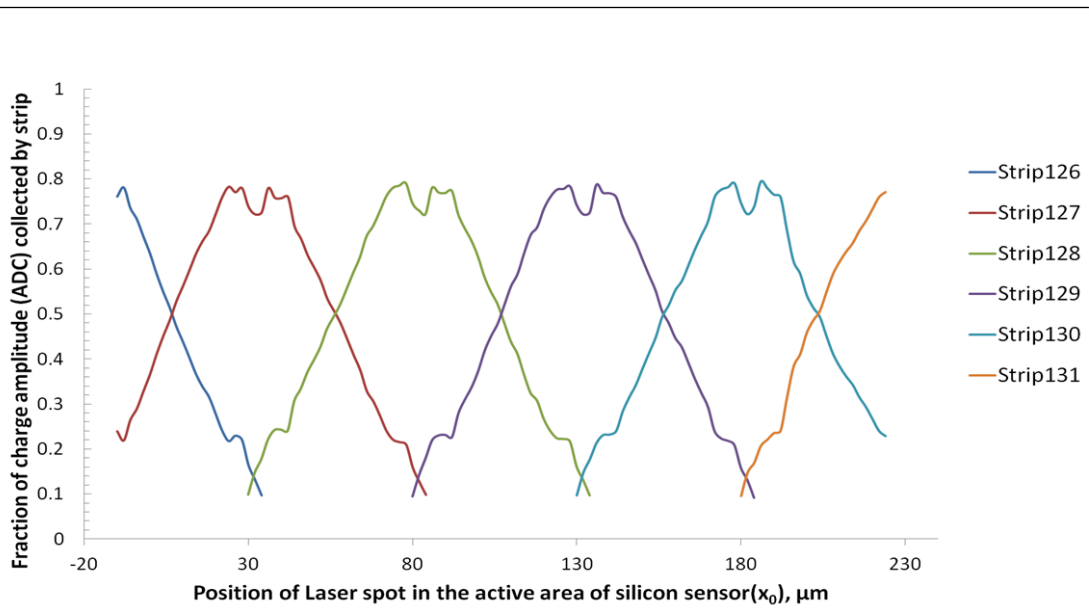


Figure 5.18: Fractional amplitude of charge amplitude collected at n-side depending on the strip under consideration.

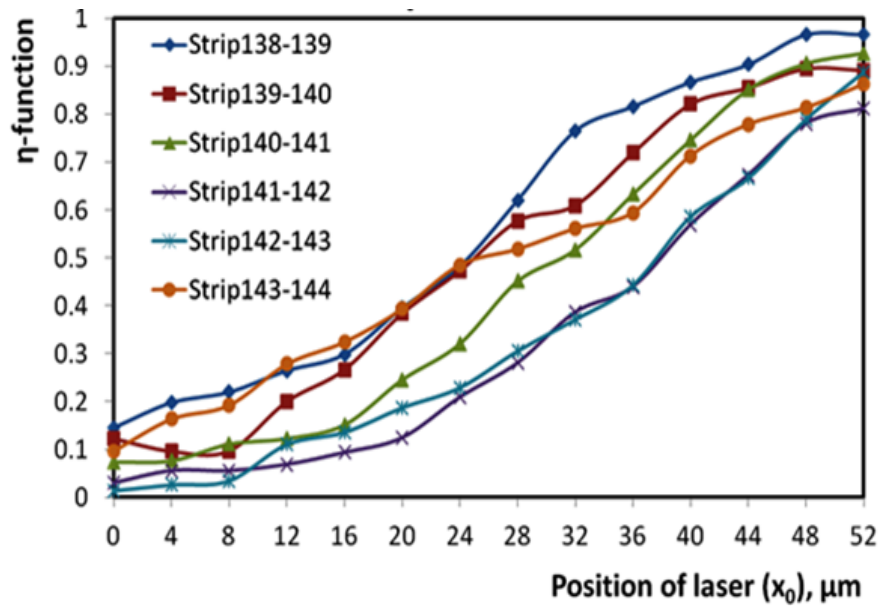


Figure 5.19: η function for p-side strips of CBM05 prototype sensor

Fig. 5.19 and 5.20 shows the η function plotted as a function of the mean position of the laser spot (x_o). The η function for the p-side shows similar but different slopes from one to the other. This could be possible because of variation

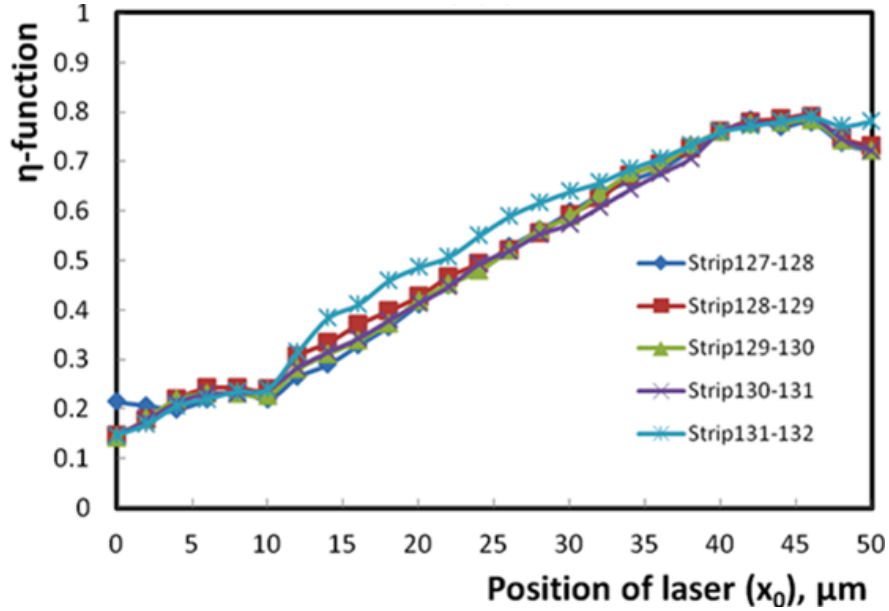


Figure 5.20: η function for n-side strips of CBM05 prototype sensor

in the electrical field around the implant and also the charge accumulated or lost due to multiple reflection on the n-side. Whereas, the η function for the n-side describes the uniformity in the response of all the strips with same slope. The dip on the edge is observed due to reflections from the metallisation on the top of the each strip. The results shows that if the charge is injected locally in a region of $5 \mu\text{m}$ close to the strip the charge lost to the neighbouring strip is $\leq 7\%$ for p-side and $\leq 17\%$ on n-side. The charge lost to the neighbour from the n-side is explained by the reflection and distortion of the field around the metal electrodes.

5.7.3 Spot-size measurement

Introduction

The laser spot-size can be measured in-situ during the measurement (laser measurements at LTS). As the laser spot (assuming to be a Gaussian distribution) with mean position, x_o moves over the laser strips (aluminium metal pads), it is observed that the total charge collected as a cluster with total strips activated has a local minima (ref. plot total amplitude charge collection). These local minima are due to the reflectance and lower absorption of infra-red light photons

in the metal (ref. table reflectance and absorption coefficient for 1060 nm for aluminium, silicon and silicon-di-oxide).

Test sensor

The Sensor CBM02 has a strip width (w) of 18 μm and strip pitch (p) of 50 μm . From the manufacturer the spot size (σ) of the laser at a working distance (d) = 10 mm is 15 μm . The sensor under test (from CiS Forschungsinstitut GmbH, Erfurt) has a thickness (t) of 300 μm . The test sensor is double sided has 256 strips orthogonally oriented on each side to be read out.

Method and calculation

As mentioned in section 5.7.1, the peculiar observation of the dip at the centre of the strip can be used to extract or to determine the spot size (σ) of the laser beam. We calculate the spot size in-situ we can consider three scenarios, two are the limiting cases and one which is relevant to our system. This can be explained by a simple analytical picture in figure. 5.21 for the extreme cases e.g.,

1. **Case A: Spot size (σ) \ll width of the metal strip (w)**

In this limiting case as the, $\sigma \ll \tilde{w}$, we assume there is no diffraction in the material and having considering only the surface reflection from the aluminium pads. It is clear that the region under the strip (n-strips in our case) would behave as an umbra (region of complete darkness) and the total charge collection (total ADC value) would certainly drop down to zero (see fig. 5.21 Case A).

2. **Case B: Spot size $\sigma \gg$ width of the metal strip (w)**

Similarly, in this limiting case as the width of the spot size (σ) is infinitely large in comparison to the strip width (w) there will be no region of umbra (region of complete darkness) and total charge collection in the region will always be the same. In more realistic situation, when the spot size is very large and moves with a mean position (x_o) there will be very little difference

in the total charge collection (total ADC value) from the activated strips (see fig. 5.21 Case B).

3. Case C: Spot size $\sigma \sim$ width of the metal strip (w)

In this case where the $\sigma \sim w$, it is clear that there will be local minima in the total charge collection (total ADC value). Since the laser spot is a Gauss distribution (assumed) it moves with a mean position (x_o) and it is clearly evident that the total charge collection will gradually decrease, reach a local minima and then recover back as laser beam (distribution) moves over the metal strip (see fig. 5.21 Case C). The width of the local minima (S) is a convolution of both metal strip (w) and spot size (σ).

The width of the local minima (S) observed at centre of the strip is a convolution of both σ and w . Mathematically,

$$S = \sigma + w \quad (5.8)$$

or spot size (σ) can be defined as:

$$\Rightarrow \sigma = S - w \quad (5.9)$$

Since the strip width (w) is known for the test sensor, in order to calculate the spot size (σ) we need to determine the width of the minima (S) from the total charge collection on the strip (n-strips in our case).

In order to check the validity of the method, the measurements were repeated with some defocused beam of laser on to the sensor. Analytically, the width of the minima shall increase if the spot-size is increased and vice-versa. Fig. 5.22, demonstrates the proof of the principle that when the laser focuser was moved away from the focuses position ($z_{focused}$) to a defocused position in z the width of the minima observed at centre of the each strip comes out to be different. The spot-size of the focused laser at 10 mm working distance is $12 \pm 2 \mu\text{m}$. The most important feature of this measurement of the spot-size is, it is calculated from the ongoing scan of the measurement. This method enables to know exactly the

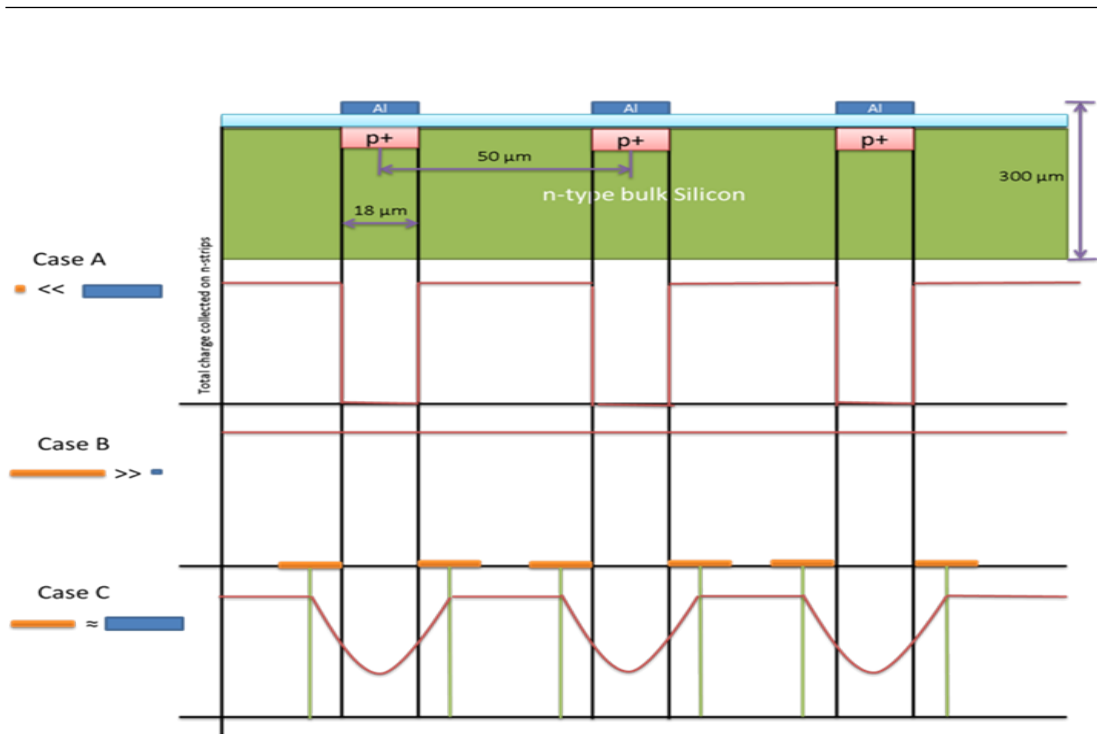


Figure 5.21: Analytical method to determine the spot-size of the laser using width of local minima

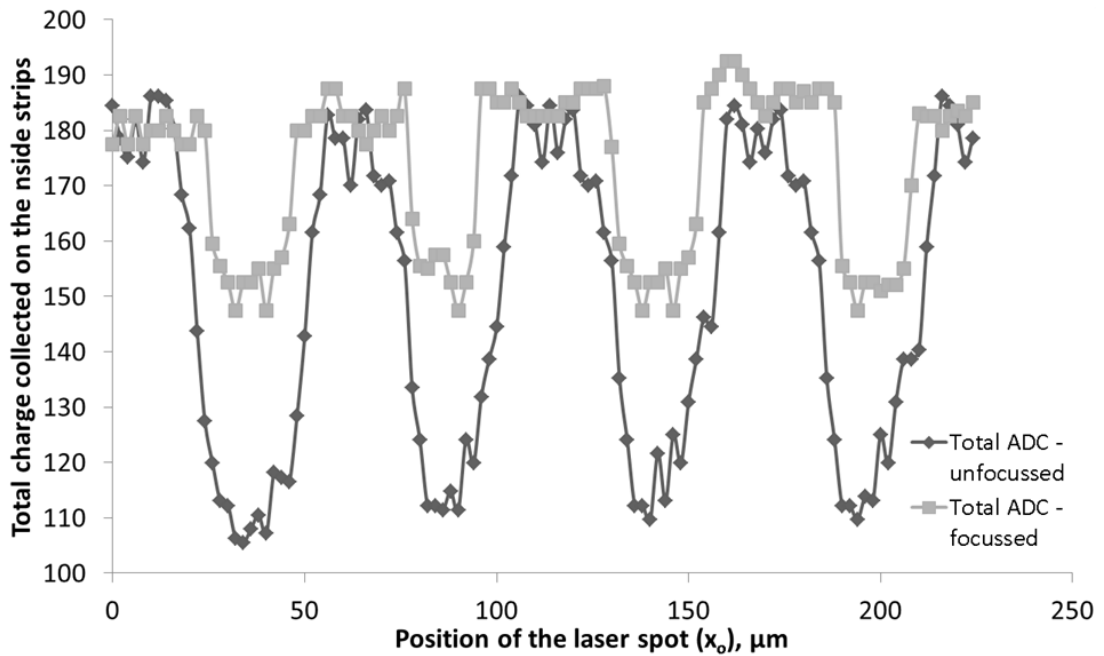


Figure 5.22: Total charge amplitude collected by all strip as function of laser position

spot-size of the laser during the measurement is performed. This measurement also act as a quality assurance parameter while analysing data from the laser scan too.

5.8 Summary of Characterization and QA with LTS

Systematic characterization procedure for the quality assurance of prototype detector modules was developed. The pulsed infra-red laser has proven to be significantly useful tool in the investigation of operational and verification of designed parameters. The fig. 5.23 shows block diagram of various characterization and quality assurance test categorized into (a) QA-Bonding, (b) QA-Sensor, and (c) QA-Strip.

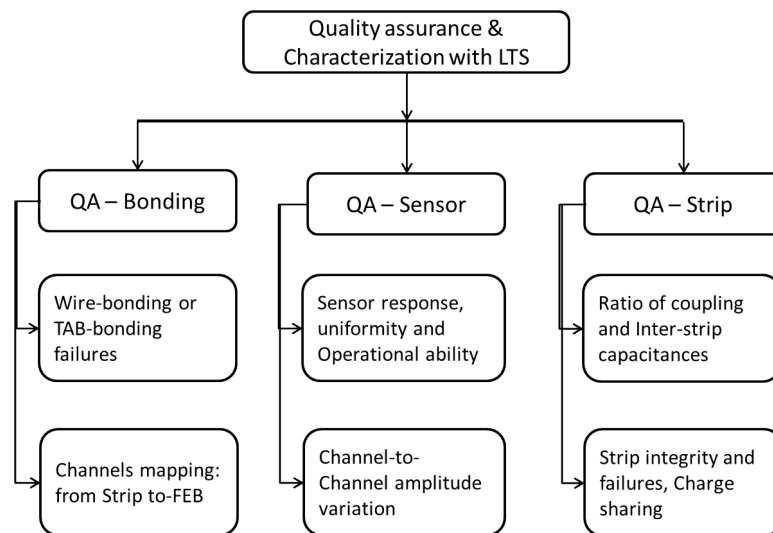


Figure 5.23: Schematic representation of the quality assurance and characterization possible with the Laser Test System at the STS.

A significant outcome of the laser based charge injection and sensor characterization was, the laser test were non-invasive in nature, local as well as bulk study, able to simulate beam-like scenario in the bulk, access to many characteristics of the detector module in one single experiment. The laser injection of charge

made it possible to study the capacitive charge division in the inter-strip region, investigate charge sharing at different bias voltages, amplitude response or a large area through regular scans and the (non-)uniformity in the amplitude response. The dedicated laser scan made it possible to study the designed parameters like mapping of channels, bonding failure, strip integrity, width of the implant, and the ration of coupling to inter-strip capacitance. As the all parameters can be investigated based on a single laser scan, it will be easy to perform quality assurance tests on more than one detector module per day. The Laser Test System is fully equipped to perform all characteristic and operational tests enabling it to be used in future for the quality assurance and characterization of the detector modules in the pre-series and series production phase.

Chapter 6

In-beam measurements with protons

In December 2013 [93], and 2014 [94] qualified prototype detector modules were configured into several detector systems for the Silicon Tracking System (STS). These prototypes were tested in a 2.4 GeV/c proton beam at the COSY synchrotron of the Jülich Research Centre, Germany. The goals of the Silicon Tracking System were [95]:

1. Perform a full system test with several detector modules in a common data stream..
2. Measure the amplitude response of the latest prototype detector modules (M1, M2, M3 and M4) from CBM05 and irradiated prototype sensors from CBM06, including the dependence of the bias voltage.
3. Study the correlation of the signal amplitude ion the p- and n-sides of the sensors.
4. Study the charge sharing and its angular dependence of beam incidence for the detector modules.
5. Investigate the feasibility in operating a irradiated detector and its amplitude response (CBM06 sensor), including the dependence with temperature and bias voltage.

-
6. Study the operational capability of the front-end electronics in the floating mode.

6.1 Experimental set-up

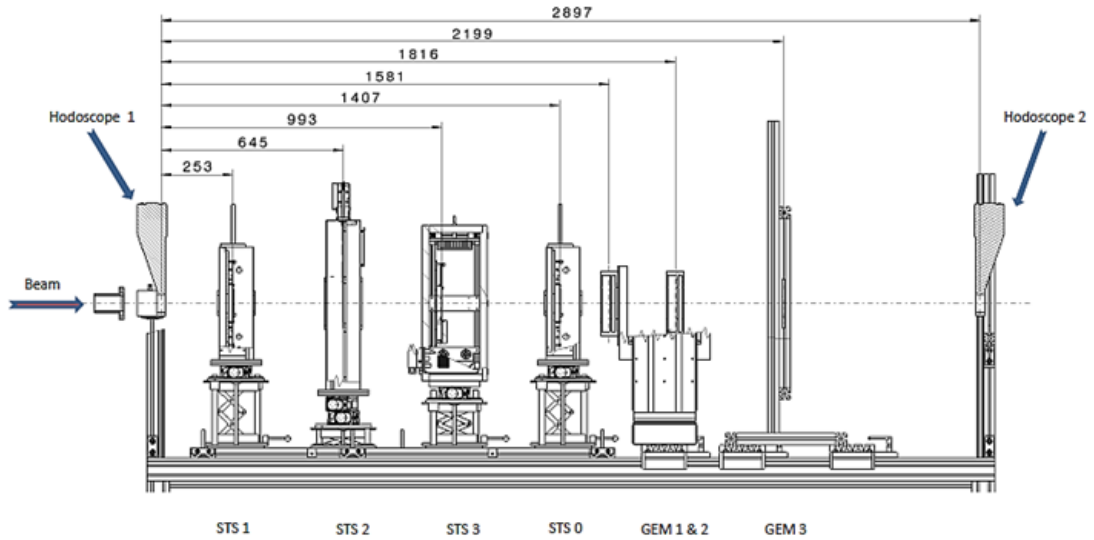


Figure 6.1: Schematic of the Beam time set-up at COSY-Jülich Research Centre

A schematic diagram of the experimental set up comprising STS stations, GEM stations and Hodoscopes is shown in Fig. 6.1. The beam direction is travelling from left to right on the axis (as shown). The set up consists of 2 Hodoscopes (Hodoscope 1 and 2) as reference detectors, 4 silicon micro-strip prototype detector systems (STS 0,1,2,3). The STS stations host one prototype detector per box at normal temperature except for STS 0 which is temperature controlled as the detector is irradiated up to dose of $2 \times 10^{14} n_{eq}/cm^2$. The detector is irradiated for the worst case scenario for STS detectors or close to limit of irradiation dose acquired after 5 years of operation at SIS-100 energies at CBM. The list of specification for the reference detectors i.e., Hodoscopes and silicon micro-strip sensors is enlisted in table 6.1. Similarly the specification for the latest test sensors (STS 3) and detector modules (STS 2) is enlisted in table 6.2.

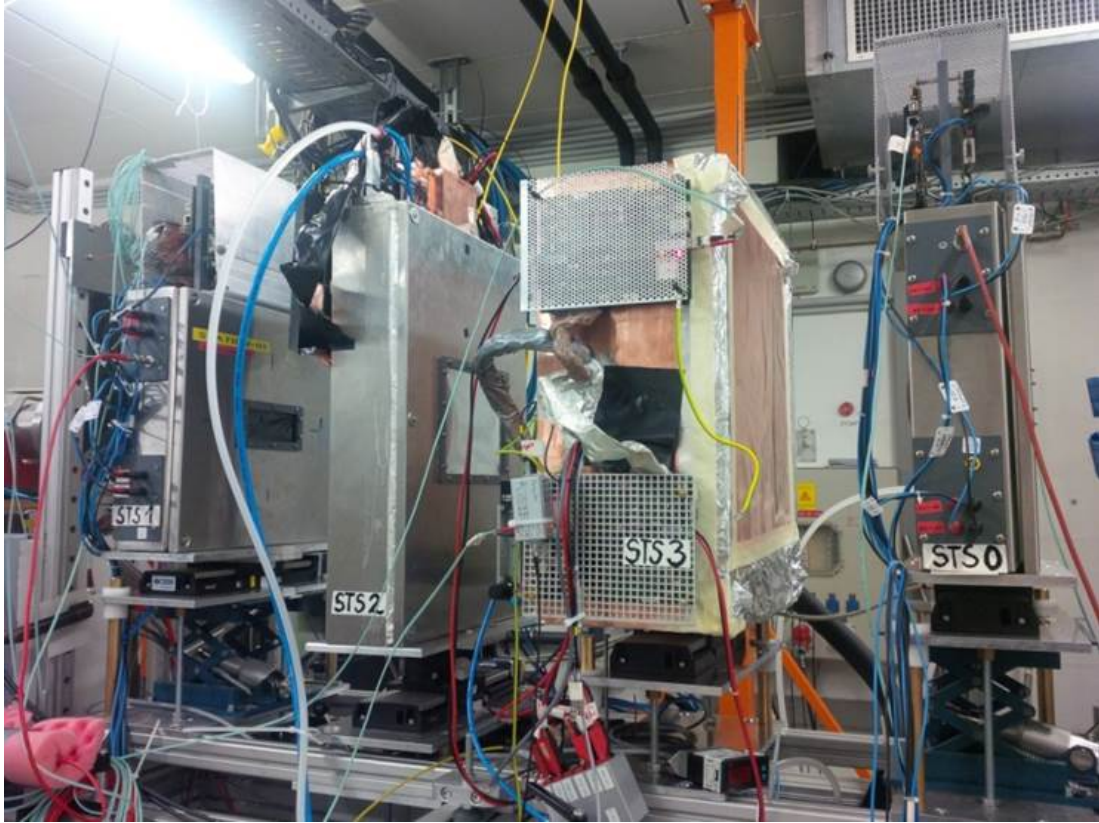


Figure 6.2: Snapshot of the Beam time set up with STS station with reference sensors and modules under test

6.2 Analysis of the beam-data

The analysis for the in-beam measurements at COSY-synchrotron is in progress now and acquired data is still under investigation. Although, with in the scope of the characterization of silicon micro-strip sensors the analysis preliminary analysis of the in-beam measurement data was performed by fellow colleagues (Anna Senger [96] and Hanna Malygina [97]). In order to see the and compare the results preliminary results are discussed and presented.

Amplitude response, MPV

The most probable signal amplitude was determined from the data of many runs, with the sensors operated at various bias voltages. The amplitude spectra, were

produced with the requirement of coincidence with the scintillator, but without the selection of clusters from the good-working region of the detectors. To determine the position of the Landau peak on each of the spectrum, the top of each peak was fitted with a third order polynomial, and the maximum was extracted. In all cases the fitting curve described well the shape of the distribution. Examples of the obtained fits are shown in Fig. 6.3 and 6.4.

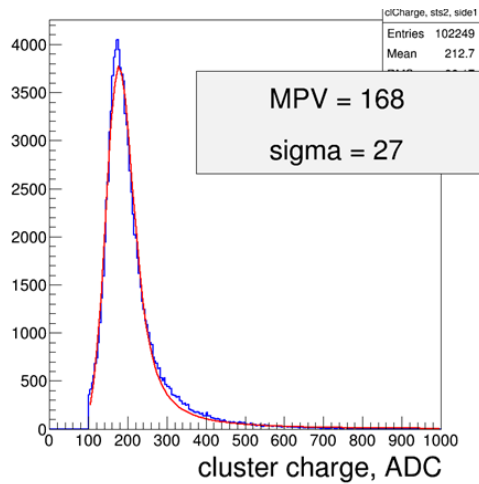


Figure 6.3: Non-Irradiated sensor: Total cluster amplitude spectra from the P-side of station STS 03.

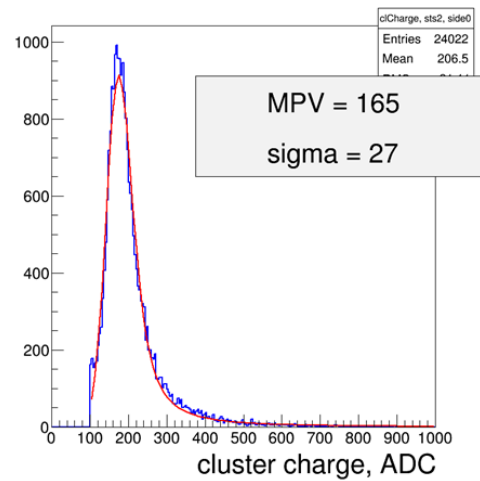


Figure 6.4: Non-Irradiated sensor: Total cluster amplitude spectra from the N-side of station STS 03.

In both cases the coincidence with the scintillator signal was required. Clusters from only the good regions were selected. For the comparison similar total cluster of the charge collected was obtained for irradiated sensors too. (see fig. 6.5 and 6.5. The drop in the MPV of the total charge accumulated in the cluster distribution is seen as a effect of radiation dose. It is important to understand that the loss decrease in the MPV of the total charge is less than 20 %.

Correlation on both sides

In the ideal situation, one must expect to observe the same signal amplitude on both p- and n-sides of the detector module. This is because the free electrons and hole are produced in the pairs. In is important to know that it cannot be denied that the charge production mechanism is no biased towards the electrons

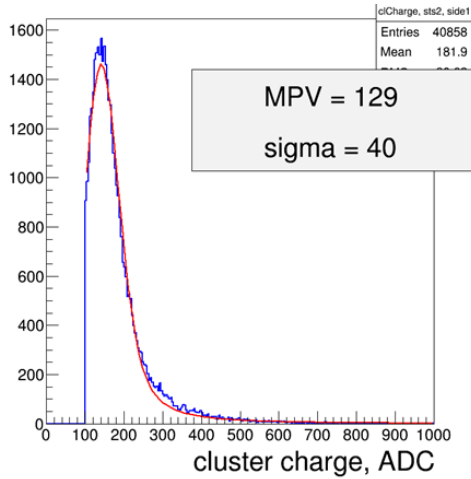


Figure 6.5: Irradiated Cluster Charge Pside

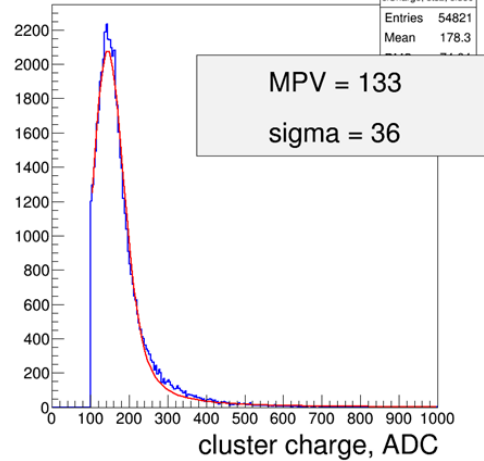


Figure 6.6: Irradiated Cluster Charge Nside

or holes but practically the charge collection is what we observe and not the charge production. The parameter of correlation is the charge collection is important tool in the investigation of the charge collection. In fig. 6.7 and 6.8 shows the correlation in the charge collection of the irradiated and non-irradiated sensor respectively.

It must be noted that the only selection applied to prepare the distribution of the correlation observed was the coincidence with the scintillator. This requirement, however, does not have a significant impact on the result, because a similar selection is applied implicitly. Indeed, to plot the amplitude correlation, clusters on the opposite sides of the sensor, that coincide in time, are selected. If the noise hit rate is moderate, the probability of a random coincidence of a real hit with a noise hit on the opposite side is very small, so the noise is suppressed. In the station 0 a clear amplitude correlation can be seen, as expected. A rough estimate of the ratio of the amplitudes, taking into account the difference of calibration coefficients for positive and negative signals, gives $A_{n-side}/A_{p-side} \sim 0.99$. The fact that there is no difference in the charge collection efficiencies is an indication for a good performance of the sensor. In station 1 the ratio of the amplitudes is $A_{n-side}/A_{p-side} \sim 1.09$. This indicates a charge collection inefficiency on the p-side of at least 8% (assuming full charge collection on the n-side of the detec-

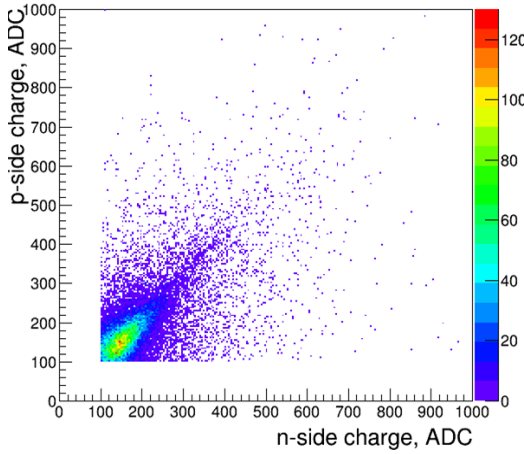


Figure 6.7: Correlation of the total cluster amplitude on the p- and n-sides in stations STS 00).

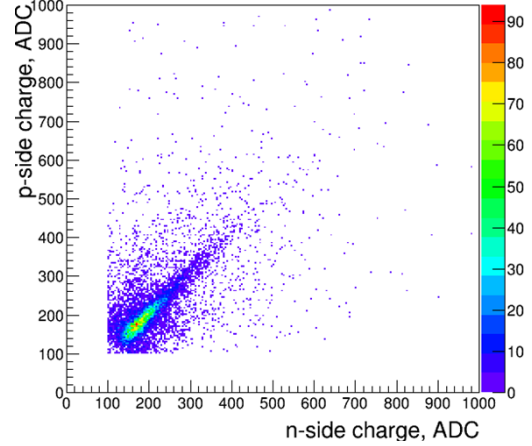


Figure 6.8: Correlation of the total cluster amplitude on the p- and n-sides in stations STS 01

tor) [98].

Radiation tolerance

Radiation hardness (or tolerance) is one of the main requirements for the STS detectors. The radiation load of $10^{13} \text{ n}_{eq}/\text{cm}^2$ is expected to be the dose on the innermost sensors of the first stations during the operation at SIS-100, and up to $10^{14} \text{ n}_{eq}/\text{cm}^2$ at SIS-300 [34]. The Radiation hardness of the CBM06 sensors was also tested in the proton beam. Four sensors (one non-irradiated) was tested. The irradiated sensors had fluences of $1 \times 10^{13} \text{ n}_{eq}/\text{cm}^2$, $5 \times 10^{13} \text{ n}_{eq}/\text{cm}^2$ and $1 \times 10^{14} \text{ n}_{eq}/\text{cm}^2$. The cool-box station STS03 was dedicated to the irradiated sensors. it was controlled for temperature in the range (0 to -8 degrees Celsius). Four sensors were tested in the beam and the preliminary charge collection from the p- and n-side of the detectors is shown in the fig. 6.9 and 6.10. It was observed that the total collected charge was moving towards left (low values) with increasing dose on the detector module.

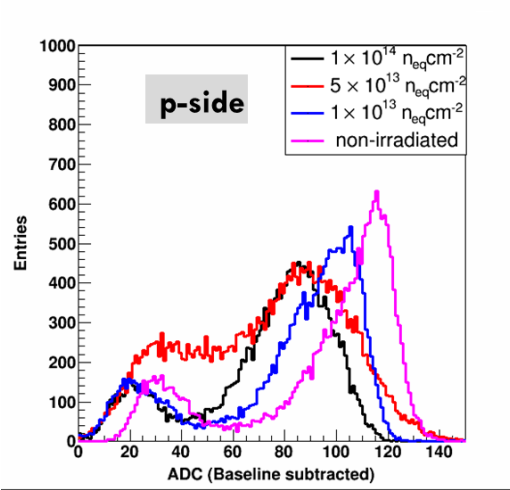


Figure 6.9: Radiation Tolerance Pside

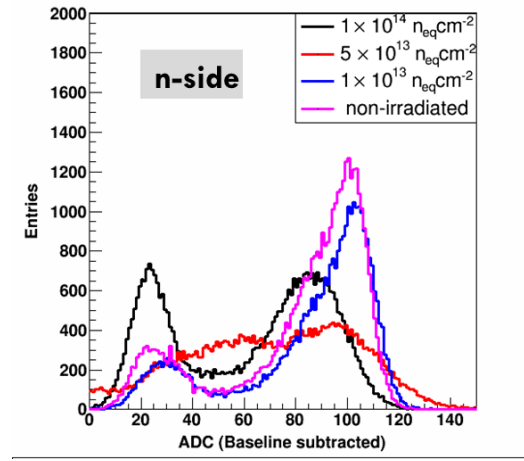


Figure 6.10: Radiation Tolerance Nside

Charge sharing function, η

As, in the station STS 02, which was equipped with a possibility to be rotated remotely around its vertical axis, CBM-05 prototype sensors with n-side having 0° stereo-angle, p-side with 7.5° , $285 \pm 15 \mu\text{m}$ thick were under a test aiming at studying charge sharing (see table 6.2 for detailed specification). The front-end electronics were triggered by a Hodoscope 0. The equivalent noise charge of about 8 ADC was observed and the threshold of 20 ADC was set in the cluster finder to cut off the noise from the incoming signal. From sec. 5.7.2, charge sharing between two fired strips is described by $\eta = A_R / (A_R + A_L)$ with $A_{R(L)}$ being the signals on the right (left) strip of the cluster [92]. The left panel in fig. 6.11 shows the measured distribution of η . Positions and widths of the peaks depend on characteristics of the sensor and the readout electronics (e.g. strip pitch, signal-to-noise ratio, coupling capacitance, threshold, etc.). For inclined tracks the η -distribution is essentially asymmetric. The position of the cluster with respect to the left strip can be calculated as $x_\eta = p \left(\int_0^\eta \frac{dN}{d\eta'} d\eta' \right) \left(\int_0^1 \frac{dN}{d\eta'} d\eta' \right)^{-1} = p f(\eta)$, where p is the strip pitch and $f(\eta)$ is obtained from measurements (see the right panel of Fig. 6.11) [96].

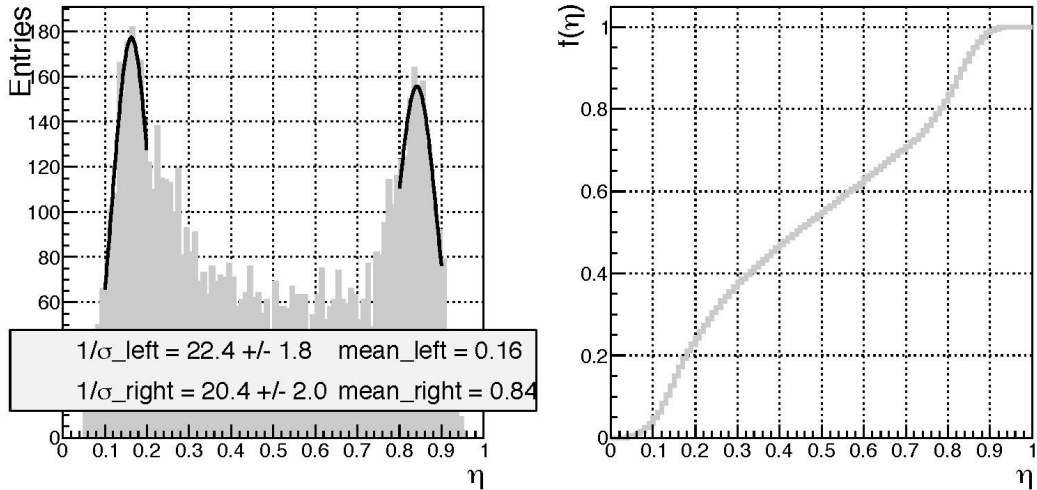


Figure 6.11: *Left:* η measured for p-side of CBM05 with Gaussian fitting the peaks. *Right:* $f(\eta)$. Perpendicular tracks.

Cluster size

It was observed that the cluster size distribution at different beam incidence angles is a good tool to verify the simulations of charge sharing in a silicon strip detector (implemented in the advanced model of the digitizer in CBMRooT). Figure 6.12 presents a typical distribution at one angle. The underestimation of 1-strip clusters number can be (at least partially) explained by the uncertainties in the NXYTER calibration and charge losses in the sensor. Assuming the n-XYTER calibration as reported [79] to be accurate, the reconstructed charge (Fig. 6.13) is observed to be smaller than the one modelled¹. It indicates presence of additional effects which play a role. Another way to agree measurements and simulation is assuming that we loose 15% of charge in sensor (additionally to 5% losing due to the trigger signal delay). Imposing 20% less charge from the sensor than expected from its thickness alone (on top of the 5% loss due to the trigger signal delay affecting the signal sampling in the ASIC) yields a better agreement.

Fig. 6.11 confirms that the modules depicted similar charge sharing behaviour

¹The Simulated charge sharing mechanism and calculation was performed by Hanna Malygina) [96]. It is not reported here but discussed in order to compare it with the measurements in-beam.

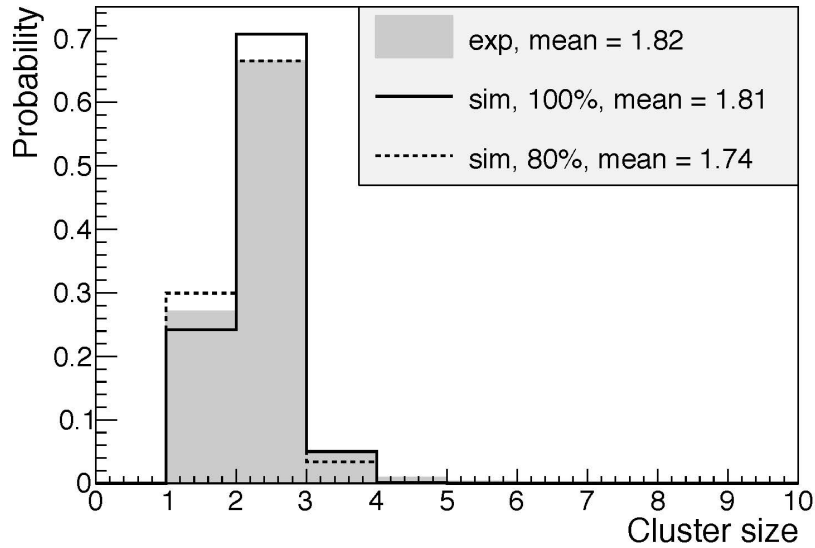


Figure 6.12: Cluster size distribution for slightly inclined tracks (10^0). Experimental data for n-side (the gray filled histogram), simulations with no (the solid line) and 20% (dashed) additional charge loosing.

in the inter-strip region in the beam-test as it was in the laser test. (see section 5.7). From the fig. 5.19 and 5.20 in preceding chapter, the charge sharing function for the module as measured with the laser test set-up is confirmed in the proton beam test result. The detailed investigation is in progress and shall be reported by the working group later. More detailed version of analysis and progress can be found in CBM progress report 2013 [99] and 2014 [100].

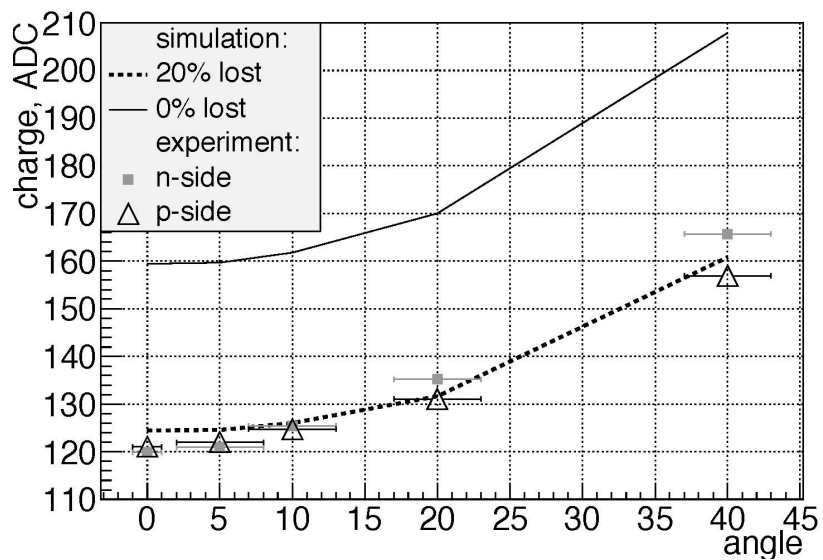


Figure 6.13: Most probable registered charge in dependence of track angles. The points show the experimental data from beam-time 2013 (the open triangles – p-side, the filled squares – n-side, the uncertainties in the angle measurements are drawn with bars) and the modelled data are represented by the lines (the solid line – no charge losses in the sensor, the dashed – 20% losses).

Table 6.1: Specification for the reference detectors in the beam-time set-up i.e., Hodoscopes (1 and 2) and the silicon prototype detectors stations (0 and 1)

Description	Specification
Hodoscopes 01 and 02	
Role	Reference detector and alignment
Type	Oriented 2 arms in X and Y axes
Size	10 cm × 10 cm
Channels to read	64 channels per arm via DABC
Mode of operation	using Read-out controller
Trigger	Yes, via Aux. signals
FEE Board	n-XYTER based read-out
Read-out	Optics- and Ethernet
Temperature of operation	Ambient Room Temperature
Provider	Hamamatsu Photonics, Japan
STS Station 00 and 01	
Role	Reference silicon detector for tracking
Type	Double sided with orthogonal strips
Channels to read	256 channels per side
Strip pitch	50 microns
Size (area)	1.5 cm × 1.5 cm
Thickness	285 ± 15 microns
Mode of operation	via DABC using Read-out controller
Trigger	Yes, via Aux. signals
FEE Board	n-XYTER based read-out
Temperature of operation	Ambient Room Temperature
Radiation Dose	Non-irradiated sensor
Provider	CiS Forschungsinstitut, Erfurt

Table 6.2: Specification for the latest prototype detectors in the beam-time set-up i.e., STS 02 and STS 03

Description	Specification
STS Station 03	
Role	Latest prototype sensor
Type	Double sided with stereo angled strips on p-side
Size (area)	6.2×4.2 cm
Thickness	300 ± 15 microns
Name (Batch)	CBM-06
Channels to read	1024 channels available, 32 channels per side
Strip pitch	58 microns
Mode of operation	via DABC using Read-out controller
Trigger	Yes, via Aux signals
FEE Board	n-XYTER based read-out
Temperature of operation	Cooled via liq. Nitrogen to 0 to -8 C
Radiation Dose	Irradiated sensor $2 \times 10^{14} n_{eq}/cm^2$
Provider	Hamamatsu Photonics, Japan
STS Station 02	
Role	Latest prototype detector module
Type	Double sided with stereo angles on p-side
Size (area)	6.2×6.2 cm
Thickness	285 ± 15 microns
Name (Batch)	CBM-05
Channels to read	1024 channels available, 128 channels per side connected
Strip pitch	58 microns
Mode of operation	via DABC using Read-out controller
Trigger	Yes, via Aux signals
FEE Board	n-XYTER based read-out
Temperature of operation	Ambient Room Temperature
Radiation Dose	Non-irradiated sensor
Provider	CiS Forschungsinstitut, Erfurt

Chapter 7

Conclusions and outlook

Significant progress in development of the STS detector module is achieved. Prototype silicon micro-strip detectors were constructed, tested and quality assured. The gained experience in construction of the detectors will be applied in designing the STS detector module.

A systematic procedure for the passive electrical test of silicon micro-strip sensors was developed and reported. A list of quality criterion is also proposed in order to help decide eligibility parameters while selecting sensors for constructing detector modules and ladders. This experience shall be of great importance in defining the quality criterion and procedures for the quality assurance during the pre-series and the series production.

A Laser Test System (LTS) has been developed for prototype sensor characterization and quality assurance for detector modules. The LTS has demonstrated the possibility to study the sensor amplitude response, uniformity and integrity over the sensor surface, charge sharing in the inter-strip region, verification of designed parameters and the in-situ laser spot size measurement crucial for analysis of data. Thus, it has been demonstrated that the infra-red ($\lambda = 1060 \text{ nm}$) laser tests can simulate in-beam scenario for the minimum ionizing particle to study performance of the prototype sensors for the CBM experiment at FAIR. The laser set-up has studied the most basic unrepairable unit of the silicon tracker. This experience with control over noise to signal, calibration of laser beam and possibility to study inter-strip region is extremely significant. Automatic scanning procedures has been developed using the EPICS sequencer. A dedicated user

friendly operator interface is available for analysis.

Successful operation of the detector prototypes in the experiments in the proton beam was demonstrated. The CBM05 sensors are proven to withstand the radiation load of $1 \times 10^{14} n_{eq}/cm^2$. A preliminary analysis of the beam-time data was presented. The charge sharing in the detector modules with proton beam confirmed the laser measurements in laboratory. This conforms the measurements at laboratory with laser are reliable and reproducible. A detailed investigation for the beam data is in progress.

An ideal probing system would be simple, inexpensive to operate, non-invasive (or minimal damage to test equipment) and compatible for the existing test structures. However, the characterization of silicon micro-strip sensors or detector modules commonly performed using either the passive electrical test, radioactive source test or in-beam test for the full functionality. It is important to recognize the fabrication techniques are getting smarter and density of the structures on the silicon sensors is only increasing. Thereby confirming the approach of non-invasive photo-intrusive technique of measurements to be crucial and significantly less damaging. Laser induced charge generation and characterization technique has made characterization of complex bulky detector modules possible. It has also proven to be a reliable method for verification and investigation of key parameters of silicon sensors which is usually not exactly available employing other methods.

Techniques for characterization of the sensors, detector modules were developed and worked out. They will be applied for quality assurance of the components during the pre-series and the series production, as well as for further studies of the detector properties for their realistic simulations.

References

- [1] A. Andronic, D. Blaschke, P. Braun-Munzinger, J. Cleymans, K. Fukushima, L.D. McLerran, H. Oeschler, R.D. Pisarski, K. Redlich, C. Sasaki, H. Satz, and J. Stachel. Hadron production in ultra-relativistic nuclear collisions: Quarkyonic matter and a triple point in the phase diagram of {QCD}. *Nuclear Physics A*, 837(12):65 – 86, 2010. [viii](#), [2](#), [4](#)
- [2] C. Höhne. Physics of compressed baryonic matter. *Journal of Physics: Conference Series*, 420(1):012016, 2013. [viii](#), [2](#), [6](#)
- [3] J. Randrup and J. Cleymans. Maximum freeze-out baryon density in nuclear collisions. *Phys. Rev. C*, 74:047901, Oct 2006. [3](#)
- [4] B. Friman, C. Höhne, J. Knoll, S. Leupold, J. Randrup, R. Rapp, and P. Senger. *The CBM Physics Book: Compressed Baryonic Matter in Laboratory Experiments*, volume 814. Springer-Verlag Berlin Heidelberg, 1 edition, 2011. [3](#), [15](#), [17](#), [19](#), [20](#)
- [5] Y. Aoki, S. Borsanyi, S. Drr, Z. Fodor, S.D. Katz, S. Krieg, and K. Szabo. The qcd transition temperature: results with physical masses in the continuum limit ii. *Journal of High Energy Physics*, 2009(06):088, 2009. [3](#), [4](#)
- [6] A. Bazavov, T. Bhattacharya, M. Cheng, C. DeTar, H.-T. Ding, Steven Gottlieb, R. Gupta, P. Hegde, U. M. Heller, F. Karsch, E. Laermann, L. Levkova, S. Mukherjee, P. Petreczky, C. Schmidt, R. A. Soltz, W. Soeldner, R. Sugar, D. Toussaint, W. Unger, and P. Vranas. Chiral and decon-

-
- finement aspects of the qcd transition. *Phys. Rev. D*, 85:054503, Mar 2012. [3](#), [4](#)
- [7] M. Stephanov, K. Rajagopal, and E. Shuryak. Signatures of the tricritical point in qcd. *Phys. Rev. Lett.*, 81:4816–4819, Nov 1998. [3](#)
- [8] Becattini, Francesco and Bleicher, Marcus and Kollegger, Thorsten and Schuster, Tim and Steinheimer, Jan and Stock, Reinhard. Hadron Formation in Relativistic Nuclear Collisions and the QCD Phase Diagram. *Phys. Rev. Lett.*, 111:082302, 2013. [4](#)
- [9] S Borsanyi. Thermodynamics of the qcd transition from lattice. *Nuclear Physics A*, 904:270c–277c, 2013. [4](#)
- [10] Y Aoki, G Endrődi, Z Fodor, SD Katz, and KK Szabo. The order of the quantum chromodynamics transition predicted by the standard model of particle physics. *Nature*, 443(7112):675–678, 2006. [4](#)
- [11] I. Arsene, I.G. Bearden, D. Beavis, C. Besliu, B. Budick, H. Bggild, C. Chasman, C.H. Christensen, P. Christiansen, J. Cibor, R. Debbe, E. Enger, J.J. Gaardhje, M. Germinario, O. Hansen, A. Holm, A.K. Holme, K. Hagel, H. Ito, E. Jakobsen, A. Jipa, F. Jundt, J.I. Jrdre, C.E. Jrgensen, R. Karabowicz, E.J. Kim, T. Kozik, T.M. Larsen, J.H. Lee, Y.K. Lee, S. Lindahl, G. Lvhidden, Z. Majka, A. Makeev, M. Mikelsen, M.J. Murray, J. Natowitz, B. Neumann, B.S. Nielsen, D. Ouerdane, R. Paneta, F. Rami, C. Ristea, O. Ristea, D. Rhrich, B.H. Samset, D. Sandberg, S.J. Sanders, R.A. Scheetz, P. Staszal, T.S. Tvetter, F. Videbk, R. Wada, Z. Yin, and I.S. Zgura. Quarkgluon plasma and color glass condensate at rhic? the perspective from the {BRAHMS} experiment. *Nuclear Physics A*, 757(12):1 – 27, 2005. First Three Years of Operation of {RHIC}. [4](#)
- [12] K. Adcox, S.S. Adler, S. Afanasiev, and Phenix Colloboration. Formation of dense partonic matter in relativistic nucleusnucleus collisions at rhic: Experimental evaluation by the {PHENIX} collaboration. *Nuclear Physics A*, 757(12):184 – 283, 2005. First Three Years of Operation of {RHIC}. [4](#)

REFERENCES

- [13] Z Fodor and S Katz. Critical point of qcd at finite t and μ , lattice results for physical quark masses. *Journal of High Energy Physics*, 2004(04):050, 2004. 4
- [14] P de Forcrand and O Philipsen. Towards the qcd phase diagram. *Proc. of Sc. (LAT2006)*, 130, 2006. 4
- [15] C. Höhne. The Compressed Baryonic Matter experiment at the future accelerator facility in Darmstadt. *Nuclear Physics A*, 749(1-4 SUPPL.), 2005. 4
- [16] Kenji Fukushima and Tetsuo Hatsuda. The phase diagram of dense qcd. *Reports on Progress in Physics*, 74(1):014001, 2011. 4, 6
- [17] L. McLerran. The phase diagram of qcd and some issues of large $n(c)$. *Nucl.Phys.Proc.Suppl.*, 195:275–280, 2009. 4
- [18] S. Seddiki. The compressed baryonic matter experiment. *Journal of Physics: Conference Series*, 503(1):012027, 2014. 6
- [19] H. Stoecker and C. Sturm. The facility for antiproton and ion research {FAIR} cosmic matter in the laboratory. *Nuclear Physics A*, 862863(0):92 – 97, 2011. The Sixth International Conference on Physics and Astrophysics of Quark Gluon Plasma (ICPAQGP-2010). 7, 9
- [20] Appa - atomic, plasma physics and applications. <http://www.fair-center.eu/for-users/experiments/appa-external.html>. Accessed: 2015-07-12. 7
- [21] Cbm - compressed baryonic matter experiment. <http://www.fair-center.eu/en/for-users/experiments/cbm.html>. Accessed: 2015-07-12. 7
- [22] Nustar - nuclear structure, astrophysics and reactions. <http://www.fair-center.eu/en/for-users/experiments/nustar.html>. Accessed: 2015-07-12. 7

-
- [23] Panda - anti-proton annihilation at darmstadt. <http://www-panda.gsi.de/>. Accessed: 2015-07-12. 7
- [24] P. Senger. The Compressed Baryonic Matter experiment at FAIR. *Nuclear Physics A*, 862-863(1):139–145, April 2011. 9
- [25] W. Ehehalt and W. Cassing. Relativistic transport approach for nucleus-nucleus collisions from {SIS} to {SPS} energies. *Nuclear Physics A*, 602(34):449 – 486, 1996. 10
- [26] W. Cassing, E.L. Bratkovskaya, and A. Sibirtsev. Open charm production in relativistic nucleusnucleus collisions. *Nuclear Physics A*, 691(34):753 – 778, 2001. 10
- [27] A. Andronic, P. Braun-Munzinger, and J. Stachel. Hadron production in central nucleusnucleus collisions at chemical freeze-out. *Nuclear Physics A*, 772(34):167 – 199, 2006. 10
- [28] P. Senger. CBM/FAIR capabilities for charm and dilepton studies. In *5th International Workshop on Critical Point and Onset of Deconfinement - CPOD 2009*. 11
- [29] A. R. Bodmer. Collapsed nuclei. *Phys. Rev. D*, 4:1601–1606, Sep 1971. 12
- [30] J.K. Ahn, S. Ajimura, H. Akikawa, B. Bassalleck, and A. Berdoz. Production of $(\lambda\lambda)h-4$ hypernuclei. *Phys.Rev.Lett.*, 87:132504, 2001. 12
- [31] H. Takahashi, J.K. Ahn, H. Akikawa, S. Aoki, and K. Arai. Observation of a $(\lambda\lambda)he-6$ double hypernucleus. *Phys.Rev.Lett.*, 87:212502, 2001. 12
- [32] R. H. Dalitz, D. H. Davis, P. H. Fowler, A. Montwill, J. Pniewski, and J. A. Zakrzewski. The identified $\lambda\lambda$ -hypernuclei and the predicted h-particle. *Proceedings of the Royal Society of London A: Mathematical, Physical and Engineering Sciences*, 426(1870):1–17, 1989. 12

-
- [33] J. Steinheimer, C. Sturm, S. Schramm, and H. Stcker. Strange perspectives at fair. *Journal of Physics G: Nuclear and Particle Physics*, 37(9):094026, 2010. [12](#)
- [34] J. Heuser, W. Müller, V. Pugatch, P. Senger, C. J. Schmidt, C. Sturm, and U. Frankenfeld. *[GSI Report 2013-4] Technical Design Report for the CBM Silicon Tracking System (STS)*. GSI, Darmstadt, 2013. [13](#), [15](#), [16](#), [17](#), [18](#), [19](#), [20](#), [25](#), [26](#), [31](#), [32](#), [71](#), [93](#)
- [35] B. Hyams, U. Koetz, E. Belau, R. Klanner, G. Lutz, E. Neugebauer, A. Wylie, and J. Kemmer. A silicon counter telescope to study short-lived particles in high-energy hadronic interactions. *Nuclear Instruments and Methods in Physics Research*, 205(12):99 – 105, 1983. [22](#)
- [36] E. Belau, J. Kemmer, R. Klanner, U. Ktz, G. Lutz, W. Mner, E. Neugebauer, H.J. Seebrunner, and A. Wylie. Silicon detectors with 5 m spatial resolution for high energy particles. *Nuclear Instruments and Methods in Physics Research*, 217(12):224 – 228, 1983. [22](#)
- [37] R. Bailey, E.R. Belau, T. Bhringer, M. Bosman, V. Chabaud, C. Damerell, C. Daum, G. de Rijk, H. Dijkstra, A. Dwurazny, S. Gill, A. Gillman, R. Gilmore, L. Grlich, Z. Hajduk, C. Hardwick, W. Hoogland, B.D. Hyams, J. Kemmer, R. Klanner, U. Ktz, G. Ltjens, G. Lutz, J. Malos, W. Mner, E. Neugebauer, G. Polok, M. Rozanska, K. Rybicki, H.J. Seebrunner, U. Stierlin, R.J. Tapper, H.G. Tiecke, M. Turala, G. Waltermann, P. Weillhammer, F. Wickens, L.W. Wiggers, A. Wylie, and T. Zeludziewicz. A silicon strip detector telescope for the measurement of production and decay of charmed particles. *Nuclear Instruments and Methods in Physics Research Section A: Accelerators, Spectrometers, Detectors and Associated Equipment*, 226(1):56 – 58, 1984. [22](#)
- [38] M. Turala. Silicon tracking detectorshistorical overview. *Nuclear Instruments and Methods in Physics Research Section A: Accelerators, Spectrometers, Detectors and Associated Equipment*, 541(12):1 – 14, 2005. Development and Application of Semiconductor Tracking Detectors Proceedings

- of the 5th International Symposium on Development and Application of Semiconductor Tracking Detectors (STD 5) Development and Application of Semiconductor Tracking Detectors. 22
- [39] F. Hartmann. *Evolution of Silicon Sensors Technology in Particle Physics*, volume 231 of *Springer Tracts in Modern Physics*. Springer, Available online: <http://www.springer.com/series/426>, 2009. 22
- [40] FAIR International Steering Committee. Green paper: The modularized start version. Technical report, Facility for Anti-proton and Ion Research GmbH, Darmstadt - Germany, 2009. 23
- [41] AS Brogna, S Buzzetti, CJ Schmidt, HK Soltveit, U Trunk, W Dabrowski, T Fiutowski, R Szczygie, and P Wiacek. The n-xyter reference manual. 26
- [42] V. Bartsch, W. de Boer, J. Bol, A. Dierlamm, E. Grigoriev, F. Hauler, S. Heising, and L. Jungermann. An algorithm for calculating the lorentz angle in silicon detectors. *Nuclear Instruments and Methods in Physics Research Section A: Accelerators, Spectrometers, Detectors and Associated Equipment*, 497(23):389 – 396, 2003. 27
- [43] I. Kisel. Event reconstruction in the CBM experiment. *Nuclear Instruments and Methods in Physics Research, Section A: Accelerators, Spectrometers, Detectors and Associated Equipment*, 566(1):85–88, October 2006. 27
- [44] S. Gorbunov and I. Kisel. Event reconstruction in the cbm experiment. Technical Report FAIR-QCD-CBM-04, DESY Zeuthen, Platanenallee 6, 15738 Zeuthen, Germany, 2004. 28
- [45] Cis forschungsinstitut gmbh, erfurt germany. <http://www.cismst.org/>. 32
- [46] Hamamatsu photonics, japan. <http://www.hamamatsu.com/>. 32
- [47] Pradeep Ghosh. Track measurement in the high multiplicity environment at the CBM Experiment. *Journal of Physics: Conference Series*, 503(1):012028, April 2014. 37, 49

-
- [48] P. Ghosh. Systematic characterization and quality assurance of silicon micro-strip sensors for the Silicon Tracking System of the CBM experiment. *Journal of Instrumentation*, 9(07):C07001–C07001, July 2014. 37
- [49] T. Bergauer. Silicon sensor research and development for cms upgrade. <http://indico.cern.ch/event/268876/>, October 2013. Presentation in a workshop related to the CMS upgrade. 39
- [50] S.C. Seidel, N.L. Bruner, M.A. Frautschi, M.R. Hoferkamp, and A. Patton. Studies of double-sided silicon microstrip detectors. *Nuclear Instruments and Methods in Physics Research Section A: Accelerators, Spectrometers, Detectors and Associated Equipment*, 383(1):128 – 136, 1996. Development and Application of Semiconductor Tracking Detectors. 40
- [51] P. Ghosh, I. Sorokin, T. Balog, P. Larionov, and M. Singla. Characterization procedures for silicon microstrip sensors of the cbm-sts. CBM-STs Note 2013-01, Feb 2013. 50
- [52] J. Kemmer. Fabrication of low noise silicon radiation detectors by the planar process. *Nuclear Instruments and Methods*, 169(3):499 – 502, 1980. 51
- [53] J.-L. Agram. {CMS} silicon strip tracker performance. *Physics Procedia*, 37:844 – 850, 2012. Proceedings of the 2nd International Conference on Technology and Instrumentation in Particle Physics (TIPP 2011). 51
- [54] F. Hartmann. Silicon tracking detectors in high-energy physics. *Nuclear Instruments and Methods in Physics Research Section A: Accelerators, Spectrometers, Detectors and Associated Equipment*, 666:25 – 46, 2012. Advanced Instrumentation. 51
- [55] W. D. Callister and D. G. Rethwisch. *Materials Science and Engineering, 5th edition*. John Wiley & Sons, Incorporated, 2001. 56
- [56] J.I. Pankove. *Optical Processes in Semiconductors*. Dover Books on Physics. Dover Publications, 2012. 56

-
- [57] B. J. McParland. *Photon Interactions with Matter*. Springer Publications, 2010. 58
- [58] H. Nikjoo, S. Uehara, and D. Emfietzoglou. *Interaction of Radiation with Matter*. Taylor & Francis Publications, 2012. 59
- [59] Absorption of light and absorption coefficient. <http://www.pveducation.org/pvcdrom/pn-junction/absorption-of-light>. Accessed: 2015-07-12. 60
- [60] A. Goetzberger, J. Knobloch, and B. Voss. *Crystalline Silicon Solar Cells*. 60
- [61] Absorption coefficient. <http://www.pveducation.org/pvcdrom/pn-junction/absorption-coefficient>. Accessed: 2015-07-12. 60
- [62] J.H. Lambert. Photometria sive de mensura et gradibus luminis, colorum et umbrae (photometry, or, on the measure and gradations of light, colors, and shade). *Augsburg ("Augusta Vindelicorum"), Germany: Eberhardt Klett, 1760*, page 391, 1760. 60
- [63] Beer. Bestimmung der absorption des rothen lichts in farbigen flssigkeiten (determination of the absorption of red light in colored liquids). *Annalen der Physik und Chemie*, 86:78–88, 1852. 60
- [64] D. Arnaud. White paper: Spectral response of silicon image sensors. www.aphesa.com/downloads/download2.php?id=1, April 2009. Accessed: 2015-07-12. 63, 67
- [65] I. Abt, S. Masciocchi, B. Moshous, T. Perschke, R. H. Richter, K. Riechmann, and W. Wagner. Characterization of silicon microstrip detectors using an infrared laser system. *Nuclear Instruments and Methods in Physics Research, Section A: Accelerators, Spectrometers, Detectors and Associated Equipment*, 423(2-3):303–319, March 1999. 66
- [66] M. Vaz, S. Cihangir, and P. Rapidis. Pulsed laser for testing silicon strip detectors. Technical Report FERMILAB-TM-1849, Fermi national Accelerator Laboratory, July 1993. 66

-
- [67] S. Shaheen, J. Boissevain, W. Collier, B.V. Jacak, J.S. Lock, P. Roybal, J. Simon-Gillo, W. Sondheim, J.P. Sullivan, and H. Ziock. Characterization and quality control of silicon microstrip detectors with an infrared diode laser system. *Nuclear Instruments and Methods in Physics Research Section A: Accelerators, Spectrometers, Detectors and Associated Equipment*, 352(3):573–578, January 1995. 66
- [68] Y. Unno, Y. Iwata, T. Ohsugi, T. Kohriki, T. Kondo, S. Terada, H. Iwasaki, and Y. Yamada. A new laser test stand for simulating charged-particle tracks. *Nuclear Instruments and Methods in Physics Research, Section A: Accelerators, Spectrometers, Detectors and Associated Equipment*, 383(96):238–244, 1996. 66
- [69] G. Casse, P. P. Allport, S. F. Biagi, T. J V Bowcock, a. Greenall, and P. R. Turner. Characterisation of an inhomogeneously irradiated microstrip detector using a fine spot infrared laser. *Nuclear Instruments and Methods in Physics Research, Section A: Accelerators, Spectrometers, Detectors and Associated Equipment*, 512(1-2):60–70, October 2003. 66
- [70] D. Passeri, a. Marras, P. Placidi, M. Petasecca, and L. Servoli. A laser test system for characterizing CMOS active pixel sensors. *Nuclear Instruments and Methods in Physics Research, Section A: Accelerators, Spectrometers, Detectors and Associated Equipment*, 565(1):144–147, September 2006. 66
- [71] Peter Kodyš, Kazuhiko Hara, and Pavel. Laser tests of detectors for ATLAS Tracker Upgrade. 2006. 66
- [72] Zdeněk Doležal, Carlos Escobar, Szymon Gadomski, Carmen Garcia, Sergio Gonzalez, Peter Kodyš, Petr Kubík, Carlos Lacasta, Salvador Marti, Vasiliki a. Mitsou, Gareth F. Moorhead, Peter W. Phillips, Pavel ezníček, and Radan Slavík. Laser tests of silicon detectors. *Nuclear Instruments and Methods in Physics Research, Section A: Accelerators, Spectrometers, Detectors and Associated Equipment*, 573(1-2):12–15, April 2007. 66
- [73] Pavel Bažant, Jan Brož, Zdeněk Doležal, Zbyněk Drásal, Peter Kodyš, Peter Kvasnička, and Pavel ezníček. Laser measurement of absolute charge

- collection efficiency of a silicon detector. *Nuclear Instruments and Methods in Physics Research, Section A: Accelerators, Spectrometers, Detectors and Associated Equipment*, 581(1-2):306–309, October 2007. 66
- [74] G Batigne, S Beolé, E Biolcati, E Crescio, D Falchieri, G Mazza, F Prino, a Rashevsky, L Riccati, a Rivetti, S Senyukov, and L Toscano. Characterization of the ALICE Silicon Drift Detectors using an infrared laser. *Journal of Instrumentation*, 3(06):P06004–P06004, June 2008. 66
- [75] P. Ghosh. Characterization of silicon micro-strip sensors with a pulsed infrared laser system for the cbm experiment at fair. *Journal of Instrumentation*, 10(03):C03029, 2015. 67
- [76] H. Bischel, D. E. Groom, and S. R. Klein. 27. passage of particles through matter. 67
- [77] *Development of Readout System for the CALET Scintillating Fiber Detector*, volume 2297 of *Proceedings of ICRC 2001*. Copernicus Gesellschaft, 2001. 67
- [78] A. S. Brogna, S. Buzzetti, C. J. Schmidt, H. K. Soltveit, U. Trunk, W. Dabrowski, T. Fiutowski, R. Szczygie, and P. Wiacek. *The n-XYTER Reference Manual, Chip Version 1.0*. 67
- [79] I. Sorokin, T. Balog, V. Krylov, and C. J. Schmidt. Transconductance calibration of n-xyter 1.0 readout asic. *Nuclear Instruments and Methods in Physics Research A*, 714:136–140, June 2013. 67, 95
- [80] Sacher laser technik. <https://www.sacher-laser.com/>, 2013. Solutions for the spectroscopy measurements. 67
- [81] Sacher LaserTechnik GmbH, Sacher Lasertechnik GmbH, Rudolf-Breitscheid-Str. 3-7, 35037 Marburg, Germany. *Operational Manual and Technical specifications for the TEC045 CAT - Nanosecond Pulsed Laser Series*, 2013. 69

-
- [82] J. M. Heuser and T. Balog. Description of the prototype sts module for laboratory and in-beam tests in 2013. CBM-STs Note 2013-04, April 2013. [71](#)
- [83] A.S. Brogna, S. Buzzetti, W. Dabrowski, T. Fiutowski, B. Gebauer, M. Klein, C.J. Schmidt, H.K. Soltveit, R. Szczygiel, and U. Trunk. Nxyter, a {CMOS} read-out {ASIC} for high resolution time and amplitude measurements on high rate multi-channel counting mode neutron detectors. *Nuclear Instruments and Methods in Physics Research Section A: Accelerators, Spectrometers, Detectors and Associated Equipment*, 568(1):301 – 308, 2006. New Developments in Radiation Detectors Proceedings of the 10th European Symposium on Semiconductor Detectors 10th European Symposium on Semiconductor Detectors. [71](#)
- [84] *An universal read-out controller*, volume 5 of *TOPICAL WORKSHOP ON ELECTRONICS FOR PARTICLE PHYSICS 2010, 2024 SEPTEMBER 2010, AACHEN, GERMANY*. Journal of Instrumentation - JINST, 2010. [71](#)
- [85] Caen: NIM high voltage power supply, June 2015. NDT1470 4 Ch Reversible 8 kV/3 mA (8 W) NIM/Desktop HV Power Supply Module. [71](#)
- [86] Hameg: Programmable power supply unit, 2013. Model: HAMEG - HMP4040. [71](#)
- [87] Dr. Fritz Faulhaber GmbH and Co. KG. faulhaber - communication and function manual. <http://www.faulhaber.com>, August 2014. Version: 4th issue, 27.08.2014. [75](#)
- [88] J. B. Anderson M. R. Kraimer, A. N. Johnson, W. E. Norum, J. O. Hill, B. Franksen R. Lange, and P. Denison. *EPICS Application Developers Guide*. Argonne National Laboratory, USA, epics base release 3.14.12.4 edition, February 2015. [75](#)
- [89] Control system studio: An eclipse-based collection of tools to monitor and operate large scale control systems, such as the ones in the accelerator

- community. it's a product of the collaboration between different laboratories and universities. <http://controlsystemstudio.org/>. 75
- [90] Jörn Adamczewski-Musch, Hans G Essel, and Sergei Linev. The dabc framework interface to readout hardware. *Nuclear Science, IEEE Transactions on*, 58(4):1728–1732, 2011. 76
- [91] J. Adamczewski-Musch, D. Bertini M. Al-Turany, H. G. Essel, and S. Linev. *The Go4 Analysis Framework Reference Manual v5.0*. GSI Helmholtzzentrum GmbH, Planckstrasse 1, 64291 Darmstadt Germany, 5.0 edition, June 2015. 76
- [92] R. Turchetta. Spatial resolution of silicon microstrip detectors. *Nuclear Instruments and Methods in Physics Research A*, 335, june 1993. 80, 94
- [93] T. Balog, J. Heuser, and *et. al.* In-beam test of prototype modules for the cbm silicon tracking system. Technical report, 2014. 88
- [94] V. Friese* and C. Sturm*, editors. *CBM Progress Report 2014*. GSI, Darmstadt, 2015. 88
- [95] J. Heuser, R. Adak, T. Balog, S. Chattopadhyay, D. Dementyev, A. Dubey, D. Emschermann, J. Eschke, V. Friese, P. Ghosh, T. Heinz, Khomyanov V, P. Koczan, P. Larionov, W. F. J. Müller, W. Niebur, A. Oanca, F. Uhlig, J. Saini, S. Samanta, M. Singla, I. Sorokin, C. Sturm, C. Stüller, D. .varga, A. Wolf, and P. Zumbbruch. Test of prototype cbm detector components with proton beams at cosy. Technical report, GSI, Darmstadt, Germany, 2015. 88
- [96] H Malygina, A Senger, I Sorokin, and V Friese. Charge sharing in microstrip sensors: experiment and simulation. CBM Progress Report 2014 Page 26, GSI Helmholtzzentrum, Darmstadt, 2015. 90, 94, 95
- [97] H Malygina and V. Friese. Internal note-cbm-sts: Digitizer for the silicon tracking station. CBM-STS Note 2013-07, September 2013. 90

REFERENCES

- [98] I. Sorokin. *Characterization of silicon microstrip sensors, front-end electronics, and prototype tracking detectors for the CBM experiment at FAIR*. PhD thesis, Fachbereich Physik der Johann Wolfgang Goethe-Universität in Frankfurt am Main, March 2013. 93
- [99] Volker Friese and Christian Sturm. CBM Progress Report 2013, 04 2013. <https://www-alt.gsi.de/documents/DOC-2014-Mar-16.html>. 96
- [100] Volker Friese and Christian Sturm. CBM Progress Report 2014, 04 2015. <https://www-alt.gsi.de/documents/DOC-2015-Apr-43.html>. 96

Zusammenfassung

Die Experimente am Compressed Baryonic Matter (CBM) Detektorsystem der Facility for Antiproton and Ion Research (FAIR) haben zum Ziel, das Phasendiagramm der starken Wechselwirkung im Bereich hoher Netto-Baryondichte zu erforschen. Ideale Voraussetzungen für diese Experimente bieten Schwerionenkollisionen im FAIR-Energiebereich, da sie die Möglichkeit eröffnen, hochkomprimierte Kernmaterie im Labor herzustellen und zu untersuchen. Die besondere experimentelle Herausforderung für das CBM-Experimente besteht dabei in der Untersuchung multi-differentialer Observablen und von Teilchen mit sehr geringem Produktionsquerschnitt mit bisher unerreichter Präzision. Dies umfasst auch multi-strange (anti-) Hyperonen, kurzlebige Hadronen Zerfälle (Charm-Teilchen) und Di-Leptonen. Für Präzisionsmessungen und das Tracking hadronischer, leptonischer und photonischer Sonden wird ein Detektorsystem bestehend aus verschiedenen Komponenten geplant.

Das CBM-Experiment verfügt über folgende Detektoren: ein Micro-Vertex-Detektor (MVD), der den Zerfalls-Vertex kurzlebiger Teilchen misst. Ein Silicon Tracking System (STS), der die Bahnen geladener Teilchen im Feld eines Dipolmagneten verfolgt. Ein Ring Imaging Cherenkov Detector (RICH) wird zur Identifizierung von Elektronen und zur Unterdrückung von Pionen im Impulsbereich von bis zu 10 GeV/c genutzt. Ein Transition-Radiation-Detector wird zur zusätzlichen Unterdrückung der Pionen und zur Identifizierung von Elektronen mit Impulsen oberhalb von 1,5 GeV/c verwendet. Ein Flugzeitdetektor wird für die Identifizierung von Hadronen über Flugzeitmessungen genutzt. Die elektromagnetischen Kalorimeter von CBM werden die Photonen und neutralen Mesonen messen, die in Photonen zerfallen. Der Projectile-Spectator-Detector wird die Zentralität und die Reaktionsebene bestimmen. Zum Nachweis von Myonenpaaren aus dem Zerfall von Vektormesonen (Charmonium, Phi-, Omega- und Rho-Mesonen) wird der RICH-Detektor durch eine Kombination von Hadronenabsorbern und Myonenkammern (MUCH) ersetzt.

Die vorliegende Arbeit befasst sich mit der Entwicklung des zentralen Detektors des CBM-Experiments, dem Silicon Tracking System (STS). Das STS befindet sich im Feldvolumen (ca. 1 m³) eines Dipolmagneten und besteht aus acht Ebenen mit insgesamt 1292 doppelseitigen Silizium-Mikrostreifen-Sensoren. Mithilfe des STS können bis zu 1000 geladene Teilchenspuren pro Kern-Kern Wechselwirkung gemessen und rekonstruiert werden, mit einer Reaktionsrate von bis zu 10 MHz, einer Impulsauflösung von $\Delta p/p = 1\%$, und einer Rekonstruktionseffizienz von über 95%. Der STS ist für eine

Strahlungsdosis von bis zu $1 \times 10^{14} \text{ n}_{\text{eq}}/\text{cm}^2$ ausgelegt ($\text{n}_{\text{eq}} = 1 \text{ MeV}$ Neutronen äquivalente Strahlungsdosis). Die Detektorsignale werden über Mikrokabel mit extrem geringer Massebelegung von der freilaufenden Front-End-Elektronik ausgelesen, die sich an der Peripherie der Detektorebenen außerhalb der aktiven Fläche befindet.

Die Charakterisierung der Sensoren, der Front-End-Elektronik und der kompletten Detektormodule ist ein wesentlicher Bestandteil der Entwicklungsphase und der Vorserien- und Serienproduktion. Die Charakterisierung der mehr als 1000 Silizium-Mikrostreifen-Sensoren und anschließend der kompletten Detektormodule ist sehr zeitaufwendig und muss mit großer Sorgfalt durchgeführt werden, um die Objekte nicht zu beschädigen.

Die vorliegende Arbeit gliedert sich in zwei Teile. Im ersten Teil wird die Entwicklung eines systematischen Verfahrens zur Qualitätssicherung (QS) der doppelseitigen Silizium-Mikrostreifen-Sensoren beschrieben. Dies umfasst die Definition der verschiedenen passiven elektrischen Tests für die Prototypensensoren von der Produktion bis hin zur Montage der Detektormodule. Der zweite Teil beschreibt die Charakterisierung komplexer Objekte wie die Detektormodule (Sensor + Auslekabel + Front-End-Elektronik). Dazu wurde ein nicht-invasives licht-intrusives Verfahren entwickelt, das einen kalibrierten gepulsten Infrarotlaser für die Charakterisierung und Qualitätssicherung verwendet.

A. Charakterisierung und Qualitätssicherung für die Prototyp-Sensoren

Neben der Entwicklung eines systematischen Verfahrens zum passiven elektrischen Test der Silizium-Mikrostreifen-Sensoren wurde eine Liste von Qualitätsmerkmalen erarbeitet, um Kriterien zu definieren, die eine Auswahl geeigneter Sensoren für die Herstellung von Detektormodulen und -leitern erlauben.

Ausgehend von der systematischen Charakterisierung der Silizium-Mikrostreifensensoren konnten für die spätere Qualitätskontrolle wichtige Parameter bestimmt und Tests entwickelt werden. Die systematischen Prozeduren schließen Informationen über die Tests selber sowie deren Häufigkeit ein. Abbildung 1, zeigt den systematischen Ansatz in der Qualitätskontrolle von Siliziumsensoren im STS-Projekt. Die Tests umfassen:

- **Sensortest:** Dieser Test sollte bei jedem einzelnen Sensor gemacht werden. Obwohl der Hersteller seine Chargen testet, empfiehlt es sich, zusätzlich Basistests zur Sicherstellung der Funktionalität der erhaltenen Sensoren durchzuführen.
- **Streifentest:** Diese Test sollte bei rund 10 % der Sensoren durchgeführt werden. Auf das Testen aller Sensoren kann jedoch verzichtet werden, da verschiedene manuelle oder

automatisierte Streifentests Nadeln als Messfühler für die Sensoroberfläche nutzen. Dadurch kann dieser Test möglicherweise Kratzer oder andere mechanische Schäden auf der Sensoroberfläche verursachen. Außerdem kann der Streifentest auf nur wenigen Sensoren die operationale Leistungsfähigkeit des gesamten Sensorstreifens vorhersagen.

- **Prozessstabilitäts- und Bestrahlungstest:** Es wird empfohlen, diesen Test bei lediglich 1 % der Sensoren pro Charge durchzuführen. Die Strahlungsempfindlichkeit, die Current-Stabilität und Prozessstabilitätstests geben Informationen über (Un)-Regelmäßigkeiten im Produktionszyklus. Diese Stabilitätstests sind destruktiv und beschränken sich daher entweder auf Prototyp-Sensoren oder -Strukturen.

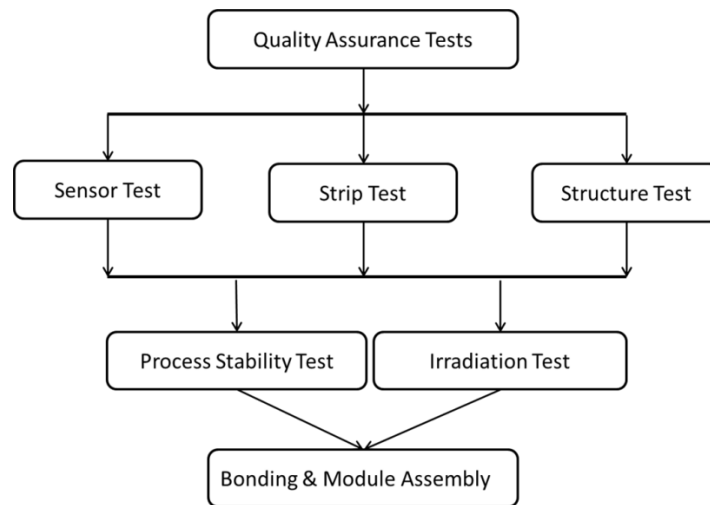


Abbildung 1: Schritte in der Qualitätskontrolle der Silizium-Mikrostreifensensoren

Alle qualifizierten Sensoren sind dazu geeignet, gebondet und zu Detektormodulen zusammengesetzt zu werden. Diese Module sind komplexe Objekte und erfordern daher besondere Vorsicht bei Zusammenbau, Handhabung und Prüfung. Die Module werden daher nicht-invasiven licht-intrusive Tests unter Verwendung eines Infrarotlasers ausgesetzt. Die hier vorgeschlagenen Techniken und Kriterien zur Qualitätssicherung kommen bei der Vorserien- und Serienproduktion der Sensoren zum Einsatz.

B. Charakterisierung und Qualitätssicherung für die Detektormodule

Das Lasertestsystem (LTS) wurde für die Charakterisierung von Sensor-Prototypen sowie für die Qualitätskontrolle von Detektormodulen entwickelt. Das LTS ermöglicht die Untersuchung der Sensoramplitude und deren Uniformität und Integrität über die Sensoroberfläche hinweg. Mithilfe des LTS kann die Ladungsteilung zwischen den Streifen gemessen, Design-Parameter verifiziert, und die Laserpunktgröße in-situ bestimmt werden. Das Testsystem ist dafür ausgelegt, durch fokussiertes Infrarot-Laserlicht (Strahlfokussdurchmesser = 12 μm , Wellenlänge = 1060 nm) ein Sensorsignal zu generieren und dies in einem automatisierten Verfahren an mehreren tausend

Positionen auf der Sensoroberfläche zu messen. Die Dauer (10 ns) und Leistung (5 mW) der Laserimpulse sind so gewählt, dass durch die Absorption des Laserlichts in den 300 µm dicken Silizium-Sensoren etwa 24000 Elektronen erzeugt werden. Diese Anzahl entspricht der Ladungsmenge, die durch minimal-ionisierende Teilchen (MIP) in diesen Sensoren erzeugt wird. Mithilfe des Testsystems wurden Charakterisierungsverfahren entwickelt, um die Ladungsteilung zwischen den Streifen zu bestimmen und die Uniformität der Sensorsignale über die gesamte aktive Detektorfläche zu messen. Mit dem Laser-Setup wurde die nicht reparierbare Basiseinheit der Siliziumtracker untersucht. Dies ist von großer Bedeutung, da hiermit die Kontrolle über das Signal-zu-Untergrund-Verhältnis, die Kalibrierung des Laserstrahls und die Möglichkeit zur Untersuchung der Regionen zwischen den Streifen sichergestellt werden können. Automatisierte Scanverfahren wurden mit dem EPICS-Sequencer entwickelt. Ein sehr nutzerfreundliches Operator Interface steht für die Analyse zur Verfügung.

Für gepulste Infrarotlaser konnte bereits gezeigt werden, dass sie ein sehr nützliches Werkzeug für die Untersuchung von Eigenschaften zusammengesetzter Detektormodule sind, zur Bestimmung ihrer operativen Kapazitäten und für die Verifizierung der Design-Parameter. Die Abbildung 2 zeigt ein Blockdiagramm verschiedener Charakterisierungen und Qualitätskontrolltests (QS), die unterteilt werden in (a) QS-Bonding, (b) QS-Sensor, und (c) QS-Streifen.

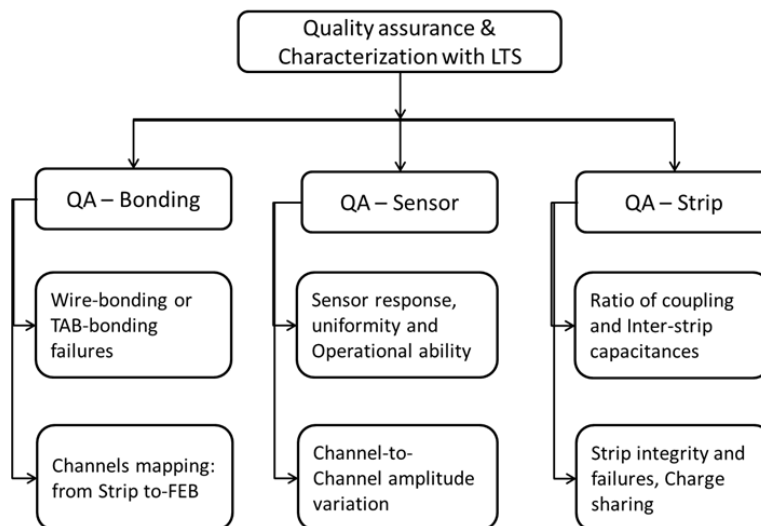


Abbildung 2: Schematische Darstellung verschiedener Charakterisierungen und Qualitätskontrolltests, die mit dem Lasertestsystem (LTS) beim STS durchgeführt werden können.

- **QS – Bonding:** Das LTS ist in der Lage, das Bonding der Detektormodule zu prüfen. Der LTS erlaubt die Überprüfung der Zuordnung der Detektorstreifen zu den Kanälen

der Front-End-Boards, und die Untersuchung der Amplitude und der Verstärkungsänderung von Kanal zu Kanal.

- **QS – Sensor:** Der LTS erlaubt die Messung der Signalamplitude zur Untersuchung der operativen Funktionalität der Sensoren bzw. der Detektormodule. Die Laserinjektion von Ladungen macht es möglich, die Ladungsteilung zwischen den Streifen in Abhängigkeit von verschiedenen Vorspannungen zu bestimmen, und die Uniformität der Signalamplitude über die gesamte Sensorfläche zu untersuchen.
- **QS – Streifen :** Auf der Ebene der Streifen erlaubt das LTS die Identifizierung von “toten” Streifen (Kanälen) und die Untersuchung der Streifenintegrität. Mithilfe des LTS kann die kapazitive Ladungsverteilung zwischen den Streifen als Funktion der Vorspannung und der Position gemessen werden. Nur mithilfe des LTS ist es möglich, verschiedene Design-Parameter wie zum Beispiel die Breite des Implants und das Verhältnis der Kopplungskapazität zur Kapazität zwischen den Streifen zu messen. Der zugehörige Laserscan machte es möglich, die die Integrität der Streifen sowie Design-Parameter zu untersuchen.

Ein wesentliches Ergebnis der laser-basierten Ladungsinjektion und Sensorcharakterisierung ist, dass die Lasertests nicht-invasiv sind und lokale wie generelle Untersuchungen erlaubt. Außerdem ist es möglich, strahlungsähnliche Szenarios zu simulieren und Informationen über viele Eigenschaften des Detektormoduls in nur einem Experiment zu erhalten.

Da alle Parameter auf einem einzelnen Laserscan basieren, sollten sich Qualitätskontrolltests mehrerer Detektormodule leicht an einem Tag durchführen lassen. Das Lasertestsystem ist ausreichend, um alle Charakteristiken und Funktionstests durchzuführen. Damit kann es künftig für Qualitätskontrollen und Charakterisierungen von Detektormodulen in der Vorserien- und Serienproduktionsphase genutzt werden.

Der erfolgreiche Betrieb der Detektorprototypen konnte in Protonenstrahlexperimenten gezeigt werden. CBM05-Sensoren können nachgewiesenermaßen Strahlungsdosen von $1 \times 10^{14} \text{ n}_{\text{eq}}/\text{cm}^2$ widerstehen. Eine vorläufige Analyse der Strahlzeitdaten wird gezeigt. Die Ladungsteilung in den Detektormodulen mit einem Protonenstrahl bestätigte die Lasermessungen im Labor. Dies zeigt, dass die Messungen im Labor mit dem Laser verlässlich und reproduzierbar sind.

Das im Rahmen dieser Arbeit entwickelte Testsystem ist einfach und kostengünstig zu betreiben, nicht-invasiv (oder mit minimaler Beschädigung des Test-Equipments) und kompatibel mit den bestehenden Teststrukturen. Üblicherweise werden Charakterisierungen von Silizium-Mikrostreifensensoren oder Detektormodulen mithilfe

von entweder passiven elektrischen Tests, mithilfe von radioaktiven Quelle, oder mit Teilchenstrahlen an Beschleunigern durchgeführt. Es ist jedoch zu beachten, dass die Herstellungsmethoden der Siliziumsensoren immer komplexer werden und die Dichte der Strukturen auf den Sensoren zunimmt. Daher ist der Ansatz mit nicht-invasiven, foto-intrusiven Messtechniken wegweisend, weil er signifikant weniger Schäden erzeugt. Laserinduzierte Ladungserzeugung und Messmethoden haben erst die Charakterisierung komplexer und großer Detektormodule möglich gemacht. Es konnte ebenso gezeigt werden, dass sich mit dem LTS zuverlässig Schlüsselparameter von Siliziumsensoren verifizieren und untersuchen lassen, was mit anderen Methoden nicht möglich.

Die Ergebnisse der Lasertests zur Ladungsteilung im Bereich zwischen den Sensorstreifen wurden durch Messungen mit Protonenstrahlen an COSY/FZ Jülich überprüft. In der vorliegenden Arbeit wurden Techniken zur Charakterisierung von Sensoren und Detektormodulen entwickelt und ausgearbeitet. Diese Techniken und Verfahren zur Qualitätssicherung der Komponenten kommen während der Vorserien- und Serienfertigung der STS- Detektormodule zur Anwendung.

Pradeep Ghosh

Curriculum Vitae

In den Bornwiesen 1a, Darmstadt 64291
Hessen, Germany

+49 176 3070 6994

+49 6159 71 3257

+49 6159 71 3916

✉ Pradeep.Ghosh@fair-center.eu

LinkedIn: <https://de.linkedin.com/in/deuprady>



Education

2012

Doctoral Studies, PhD, Goethe University, Frankfurt am Main, Germany.

Participant of HGS-HIRe, H-QM. Participated several international conferences, lecture weeks and soft-skill courses.

2008

2011

M.Tech Nuclear Science and Technology, University of Delhi, Delhi, India.

University of Delhi scholarship for Masters specialization in Nuclear Reactor Physics and Engineering from Université de Paris Sud-XI and INSTN, CEA-Saclay in France.

2005

2008

B.Sc. (Honors) in Physics, Banaras Hindu University, Varanasi, India.

Specialization in Physics, with Geology and Mathematics as subsidiary for 2 years.

2004

Senior School Certificate, CBSE Board, Bilaspur, India, 75%.

Passed with distinction. Highest marks in Physics. Major subjects: Physics, Mathematics and Chemistry

2002

High School Certificate, CBSE Board, Bilaspur, India, 81%.

Passed with distinction. Highest marks in Social Sciences.

PhD thesis

title *Characterization and quality assurance of silicon-micro-strip sensors with an infra-red pulsed laser for the CBM experiment*

supervisor Prof. Dr. Peter Senger (Goethe University Frankfurt / GSI Darmstadt)

description Development of test procedures for the systematic characterization and quality assurance of prototype silicon micro-strip sensors for the charged particles tracking in the CBM experiment. The project included defining required passive electrical test before assembling the detector modules, and development of non-invasive photo-intrusive test system using an infra-red laser for the characterization, and quality assurance of the prototype detector modules.

Master thesis

title *Application and development of pin-power reconstruction based on coupled (thermal and neutronic) code QUABOX/CUBBOX-ATHLET*

supervisor Dr. Kiril Velkov (GRS mbH, Garching b. München)

description Application and development of the pin-power reconstruction of hot channels in the reactor for the coupled thermal and neutronic code QUABOX/CUBBOX-ATHLET (commercial package in development). The project included identification of performance issues, development of the commercial package, performing benchmark test, and minimizing the error at the edges of the reactor core.

Achievements

- Elected Spokesperson for the Phd-Survey Group (2013-2014) of the Helmholtz-Juniors (Students organization representing 18 Helmholtz Institutes in Germany).
- Elected Student Representative (2013-2015) for the HGS-HIRe Participant Council.
- Represented Facility for Antiproton and Ion Research GmbH at the Germany-India Festival (Hafengeburtstag 2012) at Hamburg, Germany.
- HIC-for-FAIR scholarship (2012-2015) for doctoral studies.
- University of Delhi scholarship (2009-2010) for masters specialization in Nuclear Engineering at Paris, France.
- University of Delhi scholarship (2008-2011) for master studies.
- Rank holder and qualifier - All India Joint Admission Test for Masters Program (IIT-JAM) at Indian Institutes of Technology in 2008.
- Qualifier - District level, Science Olympiad 2003.

Languages

English	Fluent	<i>Schooling and education in English</i>
Hindi	Native	<i>Bilingual proficiency</i>
Bengali	Native	<i>Mother Tongue</i>
German	Basic Communication	<i>Level A2, practising daily, all work performed in English</i>
French	Elementary	<i>studied A1 level during masters program</i>

Interests

Travel	Train journeys, visiting new places, collecting miles from airlines
Sport	Basketball, Soccer, Cricket
Sketching	Pencil, Free hand
Volunteering	Public relations, Event management, Info-graphs
Extra	Blogging, Writing, Website development

Experience

2015 **Deputy Head, Council Issues, Facility for Antiproton and Ion Research in Europe GmbH, Darmstadt.**

Performing administrative work.

Main Duties:

- Keeping track with all Council Issues, Administrative and Financial Committees;
- Administer and assist International Delegations with proper information;
- Documentation and reporting from all Meetings;
- Facilitating proper communication with all shareholders and the Management;
- Organization and administrating all formal meetings.

2012
2015 **Researcher, Silicon Tracking Detectors, GSI Helmholtz Center for Heavy-Ion Research GmbH, Darmstadt, Germany.**

Performed Doctoral thesis project work.

Main Duties:

- Understanding and development of the prototype component for the Silicon Tracker;
- Performing electrical characterization of prototype sensors;
- Development of systematic characterization and quality assurance (QA) procedure for the prototype silicon sensors of the STS;
- Development of non-invasive, photo-intrusive characterization and QA system using a pulsed infra-red laser;
- Documentation and reporting of all development;
- Identifying and performing quality assurance tests on silicon detector modules using Laser Test System;

2010
2010 **Praktikant, Nuclear Reactor Safety Research, Gesellschaft für Anlagen -und Reaktorsicherheit mbH, Garching b. München, Germany.**

Performed Master thesis project work.

Main Duties:

- Understanding and development of the Coupled Code (QUABOX/CUBBOX-ATHLET) ;
- Implement new modules for the minimization of error at the edges of the reactor core;
- Documentation and reporting of all development;
- Implementation of new cross-section values and validating results;
- Performing benchmark test with the modules;

Vocational

2011
2011 **Intern, Silicon Wafer Design and Simulation, University of Delhi, Delhi, India.**
Did internship and training work in the field of simulation of thin silicon detector design and optimizing.

Main Duties:

- Learning SILVACO Package for Silicon Virtual Wafer Design;
- Design and optimize detector for high voltage operation;
- Design and optimize detector for smallest strip-to-pitch ratio and lowest number of guard rings.

2011
2011 **Intern, Neutron Physics at Fusion Reactor, Institute for Plasma Research, Gandhinagar - Gujarat, India.**

Did internship and training work in the field of neutron physics and reactor safety at Fusion reactors (TOKAMAK).

Main Duties:

- Learning neutron physics at fusion based reactors;
- Study the generation and evolution of the neutrons in the fusion reactors;
- Study the effects of neutron on the superconducting magnets at the TOKAMAK.

Skills

Specialization

Specialization Experimentation, Characterization, Analysis, Numerical methods, Quality Assurance, Neutron Physics, Engineering, Nuclear Physics, Detector Development, Silicon Technologies

Computing Mathematical Modeling, Matlab, SILVACO VWF, SYNOPSIS, Object-Oriented Programming, Root, MCNP, Simulation, Thermal hydraulic and Neutronic Codes

Office

Office MS-Office, OpenOffice, MS-Project, MS-Publisher, L^AT_EX

Presentation Documentation, Reporting, Presentation, Manual, Handbook

Instrumentation

Software LabVIEW, Origin, Prober-Bench, EPICS, Data Acquisition, Data Analysis, Sequencer, Control System Studio

Devices Device Communication, Motor control, Oscilloscope, Precision Ammeter and Voltmeter, LCR-meter, Manual Wire Bonding

Development

Languages C/C++, FORTRAN, PASCAL

Databases MS-Access, MySQL

Others

Internet PHP, HTML, CSS

Journal Publications

²⁰¹⁵ Ghosh, Pradeep. "Characterization of silicon micro-strip sensors with a pulsed infrared laser system for the CBM experiment at FAIR". In: *Journal of Instrumentation* 10.C03029.

²⁰¹⁴ Ghosh, Pradeep. "Systematic characterization and quality assurance of silicon micro-strip sensors for the Silicon Tracking System of the CBM experiment". en. In: *Journal of Instrumentation* 9.07, pp. C07001–C07001.

²⁰¹⁴ Ghosh, Pradeep. "Track measurement in the high multiplicity environment at the CBM Experiment". In: *Journal of Physics: Conference Series* 503.1, p. 012028.

²⁰¹³ Ghosh, Pradeep. "Quality Assurances for double-sided silicon microstrip sensors in the Silicon Tracking System of the CBM Experiment at FAIR". In: *Proceedings of Science* January 2013.

Thesis

2010

Ghosh, Pradeep. "Application and Development of Pin-power Reconstruction using Coupled code QUABOX/CUBBOX- ATHLET". Master - Nuclear Engineering. Orsay, France: University of Paris Sud-XI.

Conferences, Workshops and Courses

Conferences

2015

● **DPG Spring Meeting, German Physical Society**, Heidelberg, Germany.

2014

● **International Conference on Science and Technology for FAIR in Europe**, Worms, Germany.

2014

● **XXIV Quark Matter - International Conference on Ultra-relativistic Nucleus-Nucleus Collisions**, Darmstadt, Germany.

2014

● **DPG Spring Meeting, German Physical Society**, Frankfurt, Germany.

2013

● **DPG Spring Meeting, German Physical Society**, Dresden, Germany.

2013

● **51st International Winter Meeting on Nuclear Physics**, Bormio, Italy.

Workshops

2015

● **17th International Workshop on Radiation Imaging Detectors**, Hamburg, Germany.

2014

● **16th International Workshop on Radiation Imaging Detectors**, Trieste, Italy.

2012

● **2st Quality Assurance Workshop for prototype components of the CBM-STs**, Tuebingen, Germany.

2013

● **15th International Workshop on Radiation Imaging Detectors**, Paris, France.

2012

● **1st Quality Assurance Workshop for prototype components of the CBM-STs**, Tuebingen, Germany.

Lecture Week

2014

● **3rd Joint Helmholtz-Rosatom lecture Week**, Crete, Greece.

2012

● **2nd Joint Helmholtz-Rosatom lecture Week**, Bekasovo - Moscow, Russia.

Soft-skills Courses

2014

● **Leadership and Career Development**, Schloss Buchenau, Germany.

2013

● **Project and Time Management**, Kloster Höchst - Odenwald, Germany.

2012

● **Scientific Writing and Presentation in English**, Schloss Buchenau, Germany.

References

GSI Helmholtz Center for Heavy-Ion Research GmbH, Germany

Prof. Dr. Peter Senger

Head, CBM Research
Spokesperson, CBM Collaboration
GSI Helmholtz Center for Heavy-Ion
Research GmbH
Darmstadt, Germany
✉ P.Senger@gsi.de
☎ +49 6159 71 2652

University of Delhi, India

Prof. Dr. R.K.Shivpuri (Retd.)

Former Director
Center for Detector & Related Soft-
ware Technology
University of Delhi
Delhi, India
✉ shiv@fnal.gov

Gessellschaft für Anlagen -und Reaktorsicherheit mbH, Germany

Dr. Kiril Velkov

Head of Department
Core Behavior-Reactor Safety Research
Gessellschaft für Anlagen -und Reaktor-
sicherheit mbH
Garching b. München, Germany
✉ Kiril.Velkov@grs.de
☎ +49 221 20 68-0

